UNIVERSITÉ DE STRASBOURG

École Doctorale de Physique et Chimie-Physique

Institut de Physique et Chimie des Matériaux de Strasbourg

THÈSE présentée par :

Anna DEMCHENKO

Soutenue le **29 septembre 2015**

pour obtenir le grade de : **Docteur de l'Université de Strasbourg**

Discipline/ Spécialité : Physique / Sciences des Matériaux

Exploration des possibilités offertes en termes de multiferroïcité par le ferrite de gallium en couches minces

THÈSE dirigée par :

Mme VIART Nathalie	Professeur, Université de Strasbourg

RAPPORTEURS :

M. PRESMANES Lionel	Chargé de recherches CNRS, CIRIMAT, Toulouse
M. SORET Jean-Claude	Professeur, Université de Tours

EXAMINATEURS :

Mme POURROY Geneviève	Directeur de recherches CNRS, IPCMS, Strasbourg

ACKNOWLEDGMENTS

This work has been performed in Département de Chimie des Matériaux Inorganiques (DCMI), Institut de Physique et de Chimie de Strasbourg (IPCMS), France under supervision of Prof. Nathalie Viart, and co-supervision of Christophe Lefevre and Francois Roulland.

I would like to thank the committee members for their agreement to come to Strasbourg for the defense: Lionel Presmanes and Jean-Claude Soret and also for willingness to be rapporteurs of this work; Genevieve Pourroy for agreeing being part of the jury and for examining the scientific quality my PhD thesis.

I would also like to direct my great appreciation and thanks to my supervisor Prof. Nathalie Viart for the support she gave me through those years, knowledge and patience, for teaching me that mistakes is a part of a learning process.
To my co-supervisors Christophe Lefevre and Francois Roulland who were always there to break my mysteries in chemistry and of course for skills and for their invaluable help. Thank you for teaching me to look at the bright side of the life even when nothing is working.

Of course, I would like to thank all the members of DCMI department: it's director Pierre Rabu; Silviu Colis for keeping the spirit of competition in the preparation of the best TEM sample, to thank monsieur Cedric Leuvrey not only for endless MEB analysis but also for practicing my French speaking skills. Also, Sylvie Mainge for the assistance in paper-work and a top level of organization she did, thanks to her – all the administrative parts were not painful and significantly simplified my work. And of course many others, who gave me a friendly working atmosphere, for productive scientific discussions, coffee breaks in Aquarium where I could get to know the fabulous French culture.

I would like to express my gratitude to Gilles Versini, Sophie Barre and Jean-Pierre Vola who helped me to get into PLD depositions. Olivier Cregut for helping to fight with lenses and laser in the ablation room and making it work.

Also, I want to thank Cristian Meny for sharing knowledge in sputtering depositions. And, of course, sincerely thank Manuel Acosta for his patience, invaluable experience that he shared in sputtering deposition technique and his support in the experiments that we did, even though sometimes it was risky for the equipment itself.

I would especially like to thank Corinne Ulhaq-Bouillet for showing the beauty of reciprocal space by TEM, for enormous amount of ages spent at the microscope, for teaching me how to be patient non-stop for hours by polishing samples for microscopy.

Furthermore, I would like to thank Salia Cherifi and Romain Jarrier for a complete dedication in the electrical characterizations of incessant leakage currents in our material.

In the frame of GALIMEO project (ANR funding), it was possible to get in touch with outstanding theoretical researchers as Marjana Ležaić and Konstantin Rushchanskii from Peter Grünberg Institute, Jülich and Daniel Stoeffler from IPCMS, Strasbourg. Thanks to you the meetings dedicated to theoretical calculations were not a nightmare but fruitful discussions, giving hope for a bright polarized future. Also, part of this project was

collaboration with Brice Gautier and David Albertini (INL, Lyon), thanks to them we were able get into the art of AFM measurements.

Great thanks are to Nathalie Boudet and Vincent Foure-Vicolin (CRG BM02 ESRF, Grenoble), who helped us in REXS measurements and for great support that was given during the experiment.
I also want to thank Ekaterina Chikoidze and Yves Dumont (GEMaC, Versailles), our collaboration brought the studies to a successful achievement in the tuning the conductivity type.

In addition, great remerciements are to Morgan Trassin, who started the investigations of GFO in our group, especially for sharing priceless Platinum and making electrodes for us. And Alex Thomasson, whose cheerful spirit and strong patience when I was asking him same 1 million time ‘’Hey Alex, can I ask you a question?’’ were always amazing to me. Although I heard he made some money on bets with his officemate Zoo if I was using this question every time I entered theirs office...but let’s keep it quiet.

The greatest thanks are to all of my friends. I can’t express how grateful I am for the support, help, inspiration, critics and laugh that you gave me. First of all, Olcya and Mykola, my mentors for a long-long time. You are always my juries in case I need a judgment, you know that. Dr.Borysenko and his family for the great support through all those years. Frau Anna Kostina and Maxym Ryndya, Kate, Nina, Marek – thank you for always listening my nagging when something wasn’t working . My perfect office mates, Assil and Guido, you are my dream-team. Very special thanks to all guys whom I met here and got to know them in Strasbourg: Yulia, Ksenia, Myshka, Frank, little Hugo, Natasha, Ihor, Stas, Ivan, Zoo, Dominique, Mathias and many more I just can’t mention all here. Thanks to you I will have great memories to store. Being friends and the greatest examples of perfection and dedication to work, I want to thank Artem, Sasha and Sergii, who has been even more than that. And of course, Pierre, one of the dearest ones, for supporting me in just doing it.

And last but not least, I want to thank my family for supporting me no matter what.

Thank you.

Résumé

Les matériaux multiferroïques offrent d'impressionnantes possibilités en termes de dispositifs pour l'électronique de spin, avec notamment des applications pour le stockage de l'information. Les principales applications attendues sont les suivantes : le stockage multi-états, à densité accrue, lorsqu'aimantation et polarisation sont découplées,[1,2] les mémoires magnétoélectriques (ME-RAMs), à faible consommation d'énergie, lorsqu'il existe un couplage entre les propriétés magnétiques et électriques (effet magnétoélectrique)

permettant un contrôle électrique des propriétés magnétiques. De telles mémoires ont les avantages combinés des mémoires ferroélectriques (le faible besoin en énergie pour l'écriture dans les Fe-RAMs) et des mémoires magnétiques (l'absence de phénomène de fatigue des mémoires M-RAMs).[3,4] Il existe cependant peu de matériaux multiferroïques et/ou magnétoélectriques. Parmi ces matériaux, $BiFeO_3$ est le plus étudié en raison de ses propriétés magnétoélectriques (ME) à température ambiante.[3,5] Cependant, ce matériau étant antiferromagnétique, il ne possède pas d'aimantation nette résultante. Il est donc nécessaire de le coupler à une couche ferromagnétique qui doit être ajoutée dans le dispositif, ce qui en complexifie la production.

Le sujet de la présente thèse concerne un matériau extrêmement prometteur, le ferrite de gallium $Ga_{2-x}Fe_xO_3$ (GFO), décrit dans la littérature comme étant magnétoélectrique à température ambiante en massif et possédant une aimantation non nulle à température ambiante pour $x \geq 1.3$.[6,7] Ce matériau cristallise dans le groupe d'espace orthorhombique $Pc2_1n$ et sa structure n'a aucun lien avec les structures pérovskites observées pour la plupart des matériaux multiferroïques

connus. Il a été démontré précédemment au sein de notre groupe[8,9] qu'il est possible de déposer des couches minces de GFO orientées (0*k*0) sur des substrats non conducteurs YSZ(001) ou sur des électrodes conductrices de Pt(111) par ablation laser pulsée (PLD).

La température de Néel des couches minces obtenues augmente de manière similaire à celle des matériaux massifs avec leur teneur en Fe et dépasse la température ambiante pour x = 1.3. Lors d'un précédent travail de thèse effectué au laboratoire, les courants de fuite élevés observés dans les couches minces de GFO ont pu être considérablement réduits en dopant les couches par du Mg^{2+}.[10] Nous avions supposé que les courants de fuite étaient dus à la présence de Fe^{2+} dans les couches et à une conduction par saut entre Fe^{2+} et Fe^{3+} en sites octaédriques, la présence d'ions Fe^{2+} étant elle-même due à une sous-stœchiométrie en oxygène des dépôts. Le dopage des couches par du Mg^{2+} permettrait alors une substitution de Fe^{2+} par Mg^{2+} et empêcherait ainsi la conduction par saut. Ce mécanisme était une simple conjecture et demandait à être prouvé. La réduction des courants de fuite, même inexpliquée, avait permis de mesurer les propriétés ferroélectriques des couches minces. La polarisation mesurée s'était

cependant montrée faible vis-à-vis de la valeur attendue (P_s = 0.2 *vs.* 23 $\mu C/cm^2$)[11]. De plus, même si les résultats obtenus étaient extrêmement prometteurs, le dopage par un élément non magnétique tel que Mg^{2+} a conduit à une diminution des propriétés magnétiques du matériau.[11]

Les enjeux majeurs abordés dans ce travail de thèse sont l'optimisation de la réduction des courants de fuite et l'étude des mécanismes de conduction dans les films minces de GFO, d'une part, et la recherche de voies d'optimisation de la polarisation électrique de ces films, d'autre part, au travers de nouvelles voies de croissance. Les couches minces de GFO ont été principalement élaborées par ablation laser pulsée, selon un procédé optimisé lors de thèses précédentes.

Ce travail de thèse présente également l'optimisation de la croissance de couches minces de GFO par pulvérisation cathodique, voie encore jamais utilisée pour ce matériau, et qui a l'avantage de permettre l'application de champs électriques durant le dépôt. Une croissance sous champ électrique pourrait être un moyen d'influencer la polarisation des couches minces déposées.

Chapitre 1

Le premier chapitre de cette thèse est une présentation des matériaux magnétoélectriques et/ou multiferroïques et des applications extrêmement prometteuses que ces matériaux pourraient avoir en termes de nouveaux dispositifs électroniques. On y trouvera une description des propriétés de multiferroïcité et magnétoélectricité, ainsi qu'une liste de matériaux présentant ces propriétés.

Peu de matériaux sont éligibles pour des applications réelles, c'est-à-dire que peu de matériaux présentent leurs propriétés magnétoélectriques et/ou multiferroïques à température ambiante et ont une aimantation résultante non nulle. Parmi ces matériaux, on trouve un candidat prometteur : le ferrite de gallium $Ga_{2-x}Fe_xO_3$ (GFO), objet de cette thèse.

Chapitre 2

Le second chapitre rapporte un état de l'art concernant le ferrite de gallium GFO : les méthodes de synthèse, les propriétés structurales, magnétiques, électriques, et magnétoélectriques.

Le dopage de la maille de GFO par divers éléments sera également abordé, car c'est une voie intéressante pour moduler ses propriétés magnétiques et électriques. Deux précédentes thèses ont été effectuées au sein du laboratoire sur ce matériau et leurs résultats seront brièvement résumés ici car ils servent de base pour les travaux présentés dans cette thèse.

Chapitre 3

Dans le troisième chapitre on trouvera la description de l'ensemble des techniques expérimentales utilisées, tant pour la synthèse du matériau, sous forme massive ou de couches minces, que pour ses caractérisations structurale, magnétique et électrique.

Chapitre 4

Le chapitre quatre présente une étude du dopage de couches minces de GFO par du nickel. L'objectif poursuivi est la compréhension des mécanismes de conduction au sein des couches minces de GFO afin d'en avoir un meilleur contrôle.

Les phénomènes de conduction sont les principaux freins à l'utilisation des matériaux multiferroïques en couches minces. Des dépôts de couches minces de GFO dopé au Ni (GFO :Ni) ont été effectués sur trois substrats différents : Pt(111)//YSZ(111), YSZ(100) et STO:Nb(111). Les couches minces de GFO:Ni ont une orientation préférentielle (0*k*0) similaire à celle des dépôts non dopés et présentent 3 (dépôts sur Pt(111)//YSZ(111) et STO:Nb(111)) ou 6 (dépôts sur YSZ(001)) variants dans le plan, en accord avec les relations d'épitaxie possibles entre la phase orthorhombique de GFO et les divers substrats utilisés. Les dépôts sur électrode conductrice de Pt présentent en quantité importante une phase parasite de type spinelle et nous n'avons par conséquent pas poursuivi leur étude.

Nous avons par contre pu obtenir des dépôts de GFO:Ni ne montrant en diffraction des rayons X que la phase orthorhombique de GFO jusqu'à des taux de dopages de 5% sur YSZ(100) et STO:Nb(111). La réelle insertion de l'ion nickel au sein de la structure cristallographique de GFO a été démontrée par diffraction résonnante des rayons X.

Les paramètres de maille des couches minces de GFO non dopé sont différents de ceux du matériau massif, mais ne sont pas dûs à d'éventuelles contraintes imposées par le substrat. L'insertion de Ni dans la structure de GFO modifie ces paramètres de maille, et pour un taux de 2% de Ni on observe une forte similitude entre les paramètres des couches minces dopées et ceux du matériau massif non dopé.

Quel que soit le taux de dopage en Ni, on observe en microscopie électronique en transmission des indices de la présence d'une phase cristallographiquement proche d'une phase spinelle. Cela n'a rien d'étonnant si l'on considère la proximité entre la structure de GFO (isomorphe à ε-Fe_2O_3) et la structure spinelle (isomorphe à γ-Fe_2O_3).

Les deux structures ne diffèrent que dans l'ordre de l'empilement des couches d'oxygène : ABAC pour ε-Fe_2O_3 et ABCABC pour γ-Fe_2O_3. Des fautes d'empilement dans la phase GFO peuvent aisément conduire à des contrastes proches de la phase spinelle en microscopie électronique en transmission. Issu de simples fautes d'empilement ou d'une réelle phase spinelle, ce contraste se trouve en divers endroits de

la couche selon la nature du substrat utilisé. Alors qu'il se trouve sous forme d'une couche continue à l'interface entre le substrat et la couche de GFO pour des dépôts sur STO:Nb (111), on le trouve disséminé dans toute la couche de GFO, localisé aux joints de grains entre variants pour des dépôts sur YSZ(001).

Les propriétés magnétiques des couches minces de GFO:Ni se sont montrées similaires à celles des couches non dopées : le plan de la couche est plan de facile aimantation, alors que la normale à la couche est un axe de difficile aimantation.

L'insertion de Ni dans la maille de GFO conduit à une augmentation de la température de Néel pour de faibles dopages puis à une re-diminution pour de forts dopages. Là encore, le dopage de 2% est un dopage charnière, puisque c'est pour ce dopage que la température de Néel est maximale. On explique cela par le fait que c'est pour ce dopage que les paramètres de maille des couches minces de GFO sont les plus proches de ceux du matériau massif. Les recouvrements orbitalaires, et donc le couplage de super-échange, dont découle la température d'ordre du matériau, sont donc probablement

optimum pour cette concentration en Ni. Des champs d'échange sont observés, en particulier pour les couches déposées sur STO:Nb(111). Ils peuvent trouver leur explication dans un couplage magnétique entre la phase de GFO et la phase de type spinelle. Dans le cas des dépôts sur STO:Nb(111), cette phase de type spinelle est une longue bande bien localisée, et dont l'interface avec la couche de GFO est elle aussi bien localisée. Cela renforce les possibilités de couplage d'échange entre les phases. Ceci n'est pas le cas pour les dépôts sur YSZ(001), où l'échange entre les deux phases, localisé aux joints de grains des variants, peut avoir lieu dans diverses configurations, selon diverses directions.

Les substrats STO:Nb(111) se sont avérés trop mauvais conducteurs pour permettre des caractérisations électriques en mode transverse, mais trop bon conducteurs pour des études en mode plan. Les propriétés électriques des couches ont donc été étudiées majoritairement en mode plan sur les dépôts effectués sur YSZ(001). Le caractère semi-conducteur des couches a été démontré pour tous les dopages. Le dopage par les ions Ni conduit à une augmentation de la résistivité pour des dopages jusqu'à 2%, valeur au-delà de laquelle la

résistivité des couches diminue à nouveau. La nature des porteurs a également pu être déterminée. Si ce sont des électrons pour les couches non dopées et les faibles dopages, à partir de 2% de dopage en Ni ce sont des trous. Les caractérisations électriques sont donc en parfait accord avec un modèle de conduction par saut. Les couches non dopées présenteraient des lacunes en oxygène, qui seraient à l'origine de la réduction de Fe^{3+} en Fe^{2+}. Le dopage par des ions Ni^{2+} permettrait de ne pas former d'ions Fe^{2+} et réduirait ainsi la conduction par saut entre Fe^{3+} et Fe^{2+} en site octaédrique. Un ajout trop important de Ni^{2+} introduit des trous qui ne sont plus compensés par la sous-stœchiométrie en oxygène et la couche devient conductrice de type p.

Cette possibilité de moduler à volonté le type de conduction dans un oxyde transparent semi-conducteur magnétique par dopage par un dopant unique est un résultat majeur de ce travail de thèse.

Chapitre 5

Le chapitre cinq présente un travail d'optimisation de l'élaboration de couches minces de GFO par pulvérisation cathodique, voie encore jamais utilisée pour la fabrication de couches minces de ce matériau. Outre le fait que cette technique est la technique de choix pour les applications industrielles, le fait qu'elle permette l'application d'un champ électrique lors des dépôts constitue un nouveau levier potentiel pour le contrôle des propriétés du matériau. Nous avons montré qu'il était possible d'obtenir par pulvérisation cathodique des couches minces de qualité cristalline et de propriétés magnétiques comparables à celles des couches minces obtenues par ablation laser.

La structure cristallographique des couches est cependant moins stable que celle des couches obtenues par ablation laser car la préparation des échantillons de microscopie électronique en transmission par bombardement ionique suffit à transformer la phase orthorhombique du GFO en phase spinelle sur de très larges domaines.

L'application d'un potentiel positif au porte substrat durant le dépôt conduit à une réduction de la qualité cristalline des dépôts. Il est cependant encore possible d'obtenir des dépôts de qualité cristalline convenable pour des potentiels appliqués inférieurs à +25 V. Ce travail constitue une première étape vers une ouverture en termes de contrôle de synthèse.

Conclusion

Ce travail de thèse a permis une compréhension approfondie des mécanismes mis en jeu dans les phénomènes de conduction dans les couches minces de GFO déposées par ablation laser. Nous avons démontré que l'insertion d'un cation bivalent tel que Ni^{2+} permet non seulement de réduire considérablement les courants de fuite, mais également de contrôler la nature du type de conduction n ou p des

couches semi-conductrices de GFO. Ces couches s'avèrent également ferrimagnétiques, avec une aimantation d'environ 100 emu/cm^3 à température ambiante. On perçoit ainsi une utilisation possible des couches minces de GFO comme semi-conducteur magnétique dopé n ou p, dans des dispositifs électroniques de type transistor.

Par ailleurs, une preuve de faisabilité a été donnée pour le dépôt de GFO par pulvérisation cathodique sous champ électrique. Nous espérons ainsi ouvrir la voie à une orientation de la polarisation des couches minces pendant le dépôt, voire à des déformations accrues de maille. Des mesures par diffraction des rayons X résonnante permettront de vérifier l'orientation des mailles (axe *b* dans la direction de croissance ou dans la direction opposée). Des caractérisations ferroélectriques et magnétoélectriques permettront alors de conclure sur l'apport de cette technique de dépôt dans la synthèse de films minces de GFO. Il n'a, malgré les importants efforts de nos collaborateurs, malheureusement pas été possible de mesurer d'hystérèse ferroélectrique sur les échantillons produits dans ce travail de thèse. Nous pensons que la problématique des électrodes de contact peut être à l'origine de cela. Il faut envisager un travail approfondi dans lequel

des électrodes de diverses natures, dont le dépôt est suivi ou non d'un recuit, seront testées.

References :

[1] Scott, J. F., Nature Mater. 6 (2007) 256.

[2] Gajek, M., Bibes, M., Fusil, S., Bouzehouane, K., Fontcuberta, J., Barthelemy, A. E., and Fert, A., Nature Materials 6 (2007) 296.

[3] Bibes, M., and Barthelemy, A., Nature Materials 7 (2008) 425.

[4] Chu, Y. H., Martin, L. W., Holcomb, M. B., Gajek, M., Han, S. J., He, Q., Balke, N., Yang, C. H., Lee, D., Hu, W., Zhan, Q., Yang, P. L., Fraile-Rodriguez, A., Scholl, A., Wang, S. X., and Ramesh, R., Nature Materials 7 (2008) 478.

[5] Catalan, G., and Scott, J. F., Adv. Mater. 21 (2009) 2463.

[6] Remeika, J. P., Journal of Applied Physics 31 (1960) 263S.

[7] Arima, T., Higashiyama, D., Kaneko, Y., He, J. P., Goto, T., Miyasaka, S., Kimura, T., Oikawa, K., Kamiyama, T., Kumai, R., and Tokura, Y., Physical Review B 70 (2004) 064426.

[8] Thomasson, A., Université de Strasbourg, 2013.

[9] Trassin, M., Université de Strasbourg, 2009.

[10] Lefevre, C., Shin, R. H., Lee, J. H., Oh, S. H., Roulland, F., Thomasson, A., Autissier, E., Meny, C., Jo, W., and Viart, N., Appl. Phys. Lett. 100 (2012) 262904.

[11] Thomasson, A., Cherifi, S., Lefevre, C., Roulland, F., Gautier, B., Albertini, D., Meny, C., and Viart, N., J. Appl. Phys. 113 (2013) 214101.

Production scientifique liée à ce travail de thèse

Publications

"Incorporation of cobalt ions into magnetoelectric gallium ferrite epitaxial films: tuning of conductivity and magnetization", S. H. Oh, R. H. Shin, C. Lefèvre, A. Thomasson, F. Roulland, Y. Shin, D.-H. Kim, J.-Y. Kim, A. Demchenko, C. Leuvrey, C. Mény, W. Jo, N. Viart, *RSC Advances* 5 (2015) 34265

"Room temperature magnetic oxide with a tunable conductivity type: Ni doped $Ga_{2-x}Fe_xO_3$ compounds", A. Demchenko, Y. Chang, E.

Chikoidze, B. Berini, C. Lefèvre, F. Roulland, C. Ulhaq, C. Leuvrey, G. Versini, S. Barre, Y. Dumont, N. Viart

Manuscrit en préparation

Resonant X-Ray Diffraction Study of the Cationic Distribution: An Example with Epitaxial Thin Films of the $Ga_{2-x}Fe_xO_3$ Magnetoelectric Compound

C. Lefevre, A. Thomasson, F. Roulland, A. Demchenko, C. Leuvrey, G. Versini, S. Barre, Y. Joly, Y. Wakabayashi, V. Favre-Nicolin, N. Boudet and N. Viart

Manuscrit en préparation

Conférences

Communications orales

"Influence of Ni-doping on the structural and magnetic of thin films of the multiferroic $Ga_{2-x}Fe_xO_3$ compound"

A. Demchenko, C. Lefèvre, F. Roulland, C. Ulhaq-Bouillet, G. Versini, S. Barre, A. Derory, C. Leuvrey, N. Viart

E-MRS Spring Meeting 2015, Lille, France, 11-15 May 2015

"Cationic Distribution in $Ga_{2-x}Fe_xO_3$ thin films through Resonant X-ray Scattering"

C. Lefèvre, A. Demchenko, F. Roulland, V. Favre-Nicolin, N. Viart

E-MRS Spring Meeting 2015, Lille, France, 11-15 May 2015

"Improving magnetoelectricity in $Ga_{2-x}Fe_xO_3$ thin films through doping"

A. Demchenko , C. Lefèvre, F. Roulland, C. Ulhaq, S. Cherifi, G. Versini, S. Barre, C. Leuvrey, N. Viart

Matériaux 2014, 2 Montpellier, France, 4-28 November 2014

"Proving the ferroelectricity of Pulsed Laser Deposition grown thin films of $GaFeO_3$"

S. Martin, D. Albertini, P. Hamoumou, N. Baboux, A. Demchemko, N. Viart and B. Gautier

Joint IEEE International Symposium on Applications of Ferroelectric (ISAF), International Symposium on Integrated Functionalities (ISIF), and Piezoresponse Force Microscopy Workshop (PFM) (ISAF-ISIF-PFM 2015), Singapore, 24-27 May 2015

Communications par affiches

"Structural transformations in the orthorhombic $Ga_{2-x}Fe_xO_3$ system"

A. Demchenko, A. Thomasson, O. Marconot, C. Ulhaq, C. Lefèvre, F. Roulland, C. Mény, G. Versini, S. Barre, N. Viart

CNRS-EWHA Winter School 2014, Strasbourg, France, 27-31 January 2014

"Structural study of thin films of the magnetoelectric $Ga_{2-x}Fe_xO_3$ produced by sputtering"

A. Demchenko, A. Thomasson, O. Marconot, C. Ulhaq-Bouillet, C. Lefèvre, F. Roulland, C. Mény, N. Viart

Functional oxides for Integration in micro- and nano-electronics, Autrans, France, 7-10 April 2014

"Structural transformations in the orthorhombic $Ga_{2-x}Fe_xO_3$ system"

A. Demchenko, A. Thomasson, O. Marconot, C. Ulhaq, C. Lefèvre, F. Roulland, C. Mény, G. Versini, S. Barre, N. Viart

International School of Oxide Electronics, Summer School, Cargese, France, 2-14 September 2013

Summary

General introduction

The field of multiferroics and magnetoelectrics is full of promises in terms of applications with new outstanding devices. The existence of uncoupled magnetic and electric orders allow high density four states memories. The coupling between magnetic and electric orders pave the way for a new type of memory- the Magnetoelectric Random Access Memories (ME-RAMs). These memories in which the magnetization is controlled by the application of an electric field present both the advantages of ferroelectric memories (Ferroelectric-RAMs), such as low energy consumption for writing, and those magnetic memories (Magnetic-RAMs) such as lack of fatigue phenomena. However, very few materials exhibit these properties at room temperature, a key element for technological applications; one of the very rare candidates for integration in such recording devices is the bismuth ferrite $BiFeO_3$. This multiferroic compound has the ordering temperatures well above room temperature, but its magnetic order is antiferromagnetic type. Its use in devices therefore requires the coupling with an additional layer having a non-zero net magnetization which complicates the elaboration process. The $Ga_{2-x}Fe_xO_3$ compounds (GFO) are an interesting alternative. These compounds crystallize in an orthorhombic structure, different from the perovskite structure usually adopted by multiferroic materials. GFO is pyroelectric, ferrimagnetic, and has one of the highest magnetoelectric (ME) couplings observed for a single-phased material. It's the first material observed to simultaneously present a strong ME coupling and a non zero magnetization. It's Curie temperature is above room temperature (370 K) for x=1.4. It has a significant optical magnetoelectric effect also allowing its application in the field of optoelectronics. In addition, its applicational potential is coupled with photocatalytic properties recently used to produce hydrogen gas by decomposition of H_2O under the action of visible light.

Previously, the elaboration process of GFO in bulk and thin films was successfully optimized in the group. High quality (0*k*0) oriented GFO thin films were deposited by pulsed laser deposition (PLD) on Pt(111) and YSZ(100) substrates.

However, important leakage currents make the characterization of the electrical properties of undoped GFO films impossible. In a previous work the leakage currents were importantly reduced through the introduction of Mg^{2+} in the GFO thin films. The mechanism of conduction in the GFO films was however still not understood and the introduction of Mg^{2+} into the GFO lattice led to a decrease of the ordering temperature and saturation magnetization.

Thus, in this work we will study the conduction mechanisms in GFO thin films doping with a magnetic bivalent ion. The Ni^{2+} ions were selected because of their likeness with Fe^{3+} ions. Both are 3d elements with similar ionic radii, Ni^{2+} ions own a spin moment of 2μB, while Fe^{2+} and Fe^{3+} have spin moments of 4 and 5μB, respectively.

A second issue addressed in this manuscript is the optimization of the elaboration of GFO thin films by sputtering. Sputtering allows the application of an electric field during deposition. This could therefore open possibilities to orient the GFO cells during the deposition and possibly to enhance its polarization.

In this manuscript, the **Chapter 1** describes the different types of magnetoelectric and/or multiferroic materials and the types of devices to which they open the way if they had their properties at room temperature.

Chapter 2 is an introduction to the $Ga_{2-x}Fe_xO_3$ compound. We will describe its structural, magnetic, electric and magnetoelectric properties in bulk and thin films.

Chapter 3 provides an overview of the synthesis and analysis techniques used in this thesis. The descriptions will show the reader the reasons that made us to use them, and the specific conditions under which measurements were made.

The study of Ni doped GFO thin films on different substrates will be presented in **Chaper 4**. Structural, magnetic and electrical investigations will present the properties that insertion of Ni brings into GFO structure.

The **Chapter 5** is dedicated to the optimization of deposition of GFO by sputtering on different substrates. We will show the possible metastability of the deposited thin films. The effect of the application of an electric field during the deposition will be studied.

Finally, a general conclusion will be presented summarizing the significant results of this work, and a list of prospects on the remaining future studies to further optimize knowledge of the material.

CHAPTER 1

Multiferroic and magnetoelectric materials

1. Introduction

Materials showing simultaneously more than one type of order are extremely promising in terms of applications and allow the conception of new devices, When these orders interact through a coupling some further possibilities are perceived.

There are three types of orders known as: ferromagnetism, ferroelectricity and ferroelasticity. The two main orders which will be of interest for me in this thesis are the magnetic and electric ones. I will first present those two kinds of orders and then introduce notion of multiferroism and magnetoelectricity. Will follow the concepts of application made possible by such multifunctional materials.

I will end this chapter giving a listof the very few material which may be considered for these applications.

2. Magnetic properties of materials

2.1.Absence of order

2.1.1 Diamagnetism

Diamagnetism characterizes materials that do not contain magnetic ions. The magnetization of such materials is induced by the external magnetic field is opposite this field and has a low amplitude.

2.1.2 Paramagnetism

In paramagnetic materials, magnetism originates from the magnetic moments of atoms within the material. These moments do not interact with each other and are moving freely. This results in a zero average macroscopic magnetization. The application of a magnetic field modifies the average orientation and the resultant macroscopic magnetization is parallel to the field. This magnetization decreases as the temperature increases due to the thermal agitation which tends to confuse the magnetic moments. It becomes zero if the magnetic field is removed.

2.2 Existence of an order

2.2.1 Ferromagnetism

A ferromagnetic compound is a material that undergoes a transition from a high temperature phase without macroscopic magnetic moment to a low temperature phase characterized by the appearance of spontaneous magnetization even in the absence of an applied magnetic field [1]. The macroscopic magnetization follows the collective coupling of the spins. The moments of all randomly aligned spins in the paramagnetic phase (Figure 1-1) orient themselves in the same direction at low temperature.

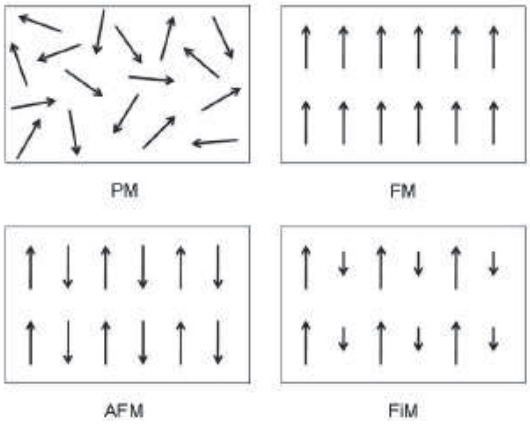

Figure 1-1. Different classes of magnetic orders PM - Paramagnetism, FM - ferromagnetism, AFM - Antiferromagnetism and FiM - ferrimagnetism

As the temperature decreases, the magnetic moments are oriented more easily under the effect of an external field due to positive exchange interactions. The magnetization is then maximum at zero temperature. The magnetic susceptibility increases quickly up to a certain temperature, called the Curie temperature T_C. Above T_C, the spontaneous magnetization is zero, and ferromagnetic material becomes paramagnetic. For temperatures above the magnetic transition temperature $T > T_C$, the susceptibility therefore follows the Curie-Weiss law:

$$(1)\quad \chi_m = \frac{C}{T-\theta}$$

The alignment and reorientation of ferromagnetic domains (in zero field oriented in different directions) under application of a magnetic field H leads to a hysteresis of the magnetization M and variation curves of the magnetic flux B. The wide range of applications

of ferromagnetic materials is due to their hysteretic characteristic. For example, the magnetic "hard" materials (with wide hysteresis cycle) having two equilibrium states of magnetization, are used for magnetic data storage. In contrast, materials with a hysteresis cycle permitting the rapid exchange of magnetization states (soft magnetic materials) are used for transformer cores.

2.2.2 Antiferromagnetism

In antiferromagnetic materials, below a transition temperature called the Neel temperature, there appear two sublattices. The magnetic moments are oriented in the simplest case, antiparallel due to exchange of negative interactions of one sublattice to another, and in parallel in a same sublattice. The resulting magnetization of the two sublattices has the same amplitude and oppose.

Unlike ferromagnetic interactions, antiferromagnetic interactions can lead to several ground states. One of the phenomena for which antiferomagnetism is of high interest is the geometrical frustration, which is the system's inability to find a single state of minimum energy. There are several classes of antiferromagnets, depending upon the arrangement of the antiparallel coupled sublattices. One of the possibilities is schematized in Figure1-2. Above the Neel temperature, the behavior is paramagnetic.

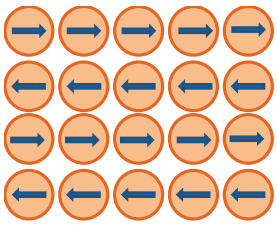

Figure 1-2. Scheme of one of the possible arrangements of the magnetic moments in an antiferromagnetic material.

2.2.3 Ferrimagnetism

A ferrimagnetic material is an antiferromagnetic material for which the resulting magnetization of the two sublattices is non zero (Figure 1-3). Spontaneous magnetization can then appear in this type of material.

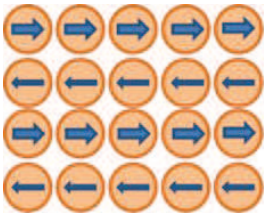

Figure 1-3. Scheme of one of the possible arrangements of the magnetic moments in a ferrimagnetic material.

2.2.4 Mechanisms

The long-range magnetic order appears at low temperature due to the magnetic coupling between the atoms spin carriers of the crystallographic unit cell. There are several exchange mechanisms: direct exchange, double exchange and super-exchange. The interaction between the magnetic moments S_i and S_j is expressed using the Heisenberg model:

$$(2)\quad H = -\sum_{ij} J_{ij} S_i S_j$$

J_{ij} represents the exchange constant. In the case of ferromagnetic interactions this parameter is positive, and it takes negative values for the antiferromagnetic interactions.
For transition metal oxides M_xO_y, the magnetic order is usually created via a super-exchange mechanism (called Kramers-Anderson). The interaction between two adjacent metal ions is carried out via a non-magnetic anion, such as O^{2-} ions in the case of the oxides (or S^{2-} in sulfides, Br^- in bromides, Cl^- in chlorides or F- in fluorides) because the distance between the 3d orbitals of the magnetic ions does not allow direct overlapping.

The so-called double exchange [2] interaction (Figure 1-4) occurs in the case of oxides when the transition ion has two valence states (as in the case of Mn^{3+} and Mn^{4+} in $La_{1-x}Sr_xMnO_3$ or Fe^{2+} and Fe^{3+} in Fe_3O_4). A ferromagnetic type of interaction between these ions may intervene through hybridization with the orbitals of oxygen. Mobility of the extra

electron that has the less oxidized form relative to the other valence represents an energy gain for a stabilization of the state. The exchange is possible in the configuration where the majority spins of the M1 and M2 cations of different valences in the same direction. The ferromagnetic state is then stabilized.

Figure 1-4. Scheme of the interaction of double exchange resulting in a ferromagnetic coupling, the transfer of the minority spin is possible only in the configuration where the majority spins are parallel.

3. Electric properties of materials

3.1 Absence of order

When at zero electric field, no polarization is present, the material is called paraelectric. In this type of material, it is possible to generate a polarization, that is to say to accumulate charges at interfaces, by applying an external electric field.

3.2 Existence of an order

Figure 1-5 represents the hierarchy of electrical properties depending on the symmetry group. The existence of polarization necessitates non centrosymmetry of the crystallographic space group.

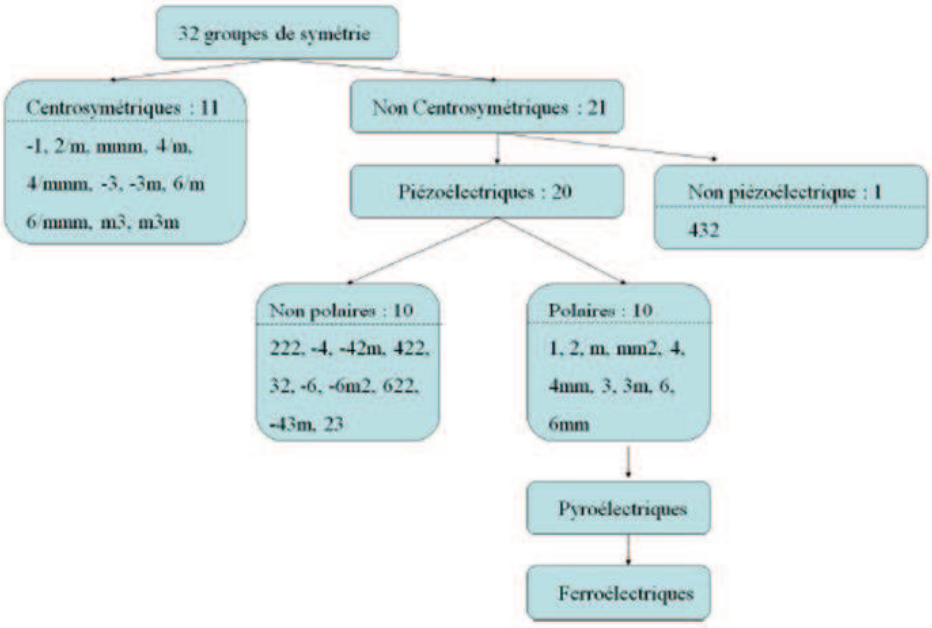

Figure 1-5. Hierarchy of the space groups for the electric properties.

Of the 21 non-centrosymmetric symmetry groups, 20 allow piezoelectricity. Piezoelectric materials may deform upon the application of an electric field and present a polarization, but will lose it when the electric field is set back to zero. Among the 20 group allowing piezoelectricity, 10 of them are polar and allow pyroelectricity. Pyroelectric materials are polar materials that exhibit spontaneous polarization which varies with the temperature. When these pyroelectric materials have a polarization whose direction can be reversed by applying an external electric field, they are called ferroelectric materials. It is then possible to observe ferroelectric hysteresis loops with remanent polarization P_r, saturation polarization P_s and coercive field E_c. Among the ferroelectric materials, one can define two classes of materials: the proper ferroelectrics in which the polarization is induced by structural instability and the improper ferroelectrics, where ferroelectricity arises due to complex lattice distortions or by other types of ordering such as charge ordering and magnetic ordering.

3.3 Ferroelectricity and polarization

Ferroelectricity is a phenomenon which was discovered by Valasek in 1921 [3]. Rochelle salt ($NaKC_4H_4O_6 \cdot {}_4H_2O$) was the first material found to show ferroelectric properties, such as a re-orientable spontaneous polarization (Ps), on cooling below a transition temperature (T_C).

Most of the ferroelectric characteristics are similar to those of ferromagnetic materials: there is a Curie temperature above which the spontaneous polarization is canceled and the ground state of paraelectric deviation (random distribution of electric dipoles) is found. A ferroelectric phase transition is often associated with the existence of anomalies in the dielectric properties at the transition temperature (study by dielectric constant measurements or polarization). Under application of an external electric field E, there is also the appearance of a hysteresis loop of electrical polarization P (M) and the electric flux density D (B). The hysteresis properties of the ferroelectric materials are the source of their applications: capacitors (high dielectric permeability due to the concentration of the electric flux density), electromechanical transducers, actuators (the change of the electrical bias is often accompanied by a change the shape of the ferroelectric material) and ferroelectric RAMs.

The most important class of ferroelectric oxide materials are perovskite ABO_3. Some examples are $PbMg_{1/3}Nb_{2/3}O_3$ (PMN)[4], $PbSc_{1/2}Ta_{1/2}O_3$ (PST) [5] and $Bi_{1/2}Na_{1/2}TiO_3$ [6]. These are also technologically important and can form end members to solid solutions in their own right, $PbMg_{1/3}Nb_{2/3}O_3$–$PbTiO_3$ (PMN-PT)[7], for example. Many of the complex ferroelectrics (PMN-PT is a classic example) exhibit ferroelectric relaxor behaviour. In these materials, the Curie point is no longer a sharp transition but is actually observed over a very wide range of temperatures.

Many ferroelectrics are low temperature modifications of a high temperature, higher symmetry structure (prototype) which has no spontaneous polarization. This prototypic structure is also called paraelectric. In the ferroelectric phase, modifications to cation and anion positions occur to give relative displacements of ions inside the unit cell, resulting in reversible spontaneous dipole moments.

Polarization reversal (switching) is a characteristic of ferroelectricity which can be observed by measuring the hysteretic polarization versus electric field (P-E) relationship below T_C.

4. Multiferroism

Materials, which combine two or more ferroic properties in the same phase, are known as multiferroics [8] (Figure 1-6).

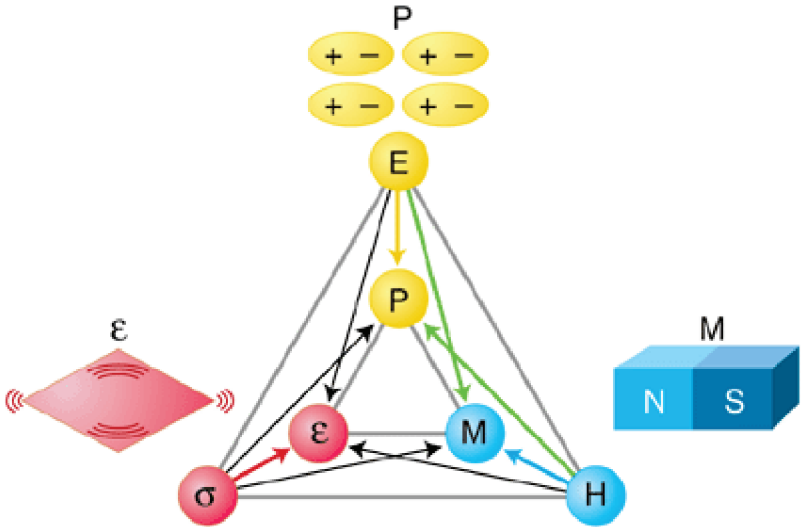

Figure 1-6. Phase control in ferroics and multiferroics [8].

The electric field *E*, magnetic field *H*, and stress σ control the electric polarization *P*, magnetization *M*, and strain ϵ, respectively. In a ferroic material, *P*,*M*, or ϵ are spontaneously formed to create ferromagnetism, ferroelectricity, or ferroelasticity, respectively. The coexistence of at least two ferroic forms of ordering may lead to additional interactions. As an example, in a magnetoelectric multiferroic, a magnetic field can control *P* or an electric field can control *M*.

Multiferroicity does not imply that there is a magnetoelectric effect, and contrarywise magnetoelectric effects can occur in the much wider class of materials than those that are simultaneously magnetically and electrically polarizable.

The lack of single-phased multiferroic materials can be explained by the limited number of symmetry groups that allow the coexistence of these orders and the fact that the origin of the electrical properties is often contradictory with the appearance of a magnetic order.

5. Magnetoelectricity

The magnetoelectric effect is defined as the coupling between the magnetic and electric properties (the ability to induce a magnetization by an electric field and *vice versa*, an electric polarization by a magnetic field) within the same material.

There are two mechanisms that cause the linear magnetoelectric effect. First, we may consider that the magnetic ions contribute in the electrical order: this will generate transitions temperatures, and in this case we have a direct coupling. The electric field is deforming the electron cloud of the magnetic ions by modifying the spin-orbit coupling and may cause an induced magnetization [9].

Second, two magnetic and electric subnetworks may also be coupled by magnetostriction or electrostriction.

When the electric and magnetic properties have different origins, the transition temperatures may be far away from each other and the coupling is usually weak.

Among the 122 magnetic Shubnikov groups 58 groups allow the existence of the linear magnetoelectric coupling. Figure 1-7 includes the general form of the magnetic magnetoelectric linear tensor for these groups when the linear magnetoelectric effect is allowed. Among these 58 groups, 13 allow the existence of magnetization and a spontaneous polarization (m'm'2, 3m ', 4m'm' 6m'm ', 1, 2, 3, 4, 6, m, 2 ', m', mm'2 '): these are multiferroic materials FM / FE type. If one considers groups where ferrimagnetic and antiferromagnetic orders as well are allowed (31 groups), then the linear magnetoelectric coupling is allowed for 13 of them. For each group the second-order magnetoelectric coupling is allowed.

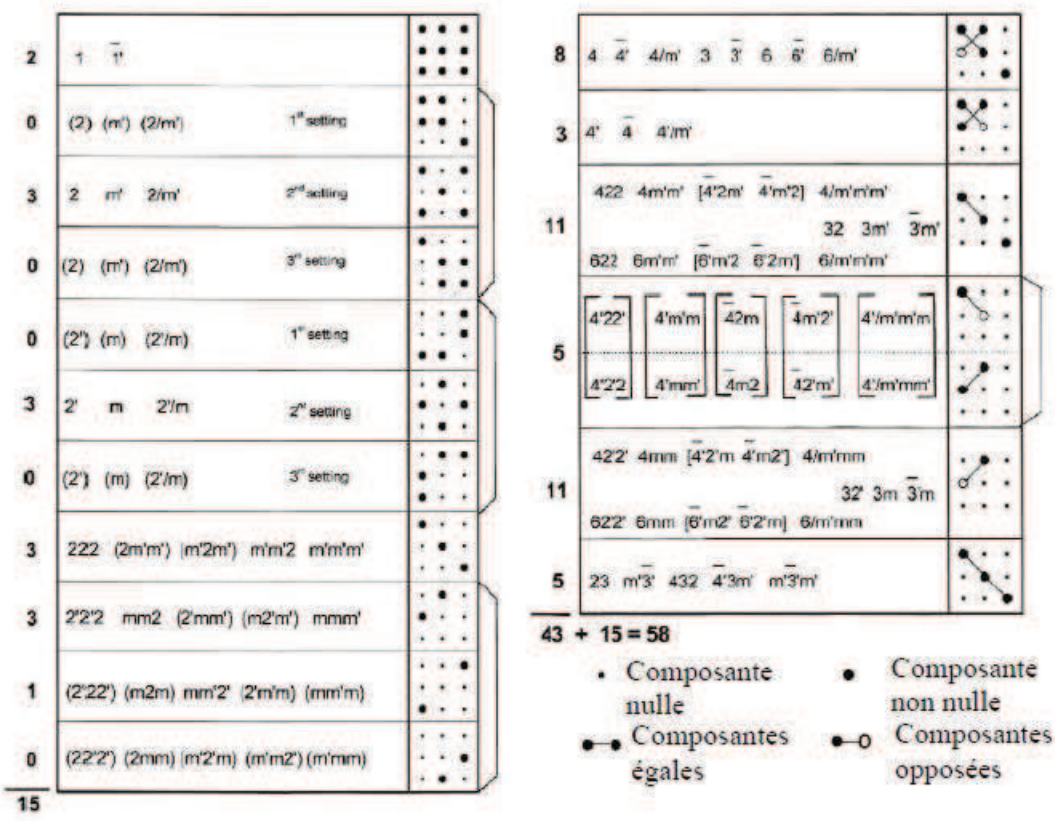

Figure 1-7. Expression of the linear magnetoelectric tensor for the 58 groups in which the magnetoelectric effect is allowed. [10]

6. Applications

6.1 Magnetic memories: M-RAM

The M-RAMs [11] (Magnetic Random Access Memories) are based on the tunnel [12] magnetoresistance effect. A tunnel junction (Figure 1-8) consists of a stack of two ferromagnetic layers (one "hard", the other "soft") separated by a thin insulating layer that permits the way for a tunnel current. The resistance of the stack depends on the relative orientation of the magnetization of the magnetic layers, the two states of parallel and antiparallel magnetization states correspond to "0" and "1". The reading process is non-destructive, as shown in Figure 1-8, the current go through the "word line" through the stack and is detected by the "bit line". A low current indicates the anti-parallel state in contrast to a

strong current that is indicative of a parallel state. The main disadvantage of these devices is the high energy required for writing, as this step requires the creation of a magnetic field to control the direction of magnetization of the "soft" ferromagnetic layer.

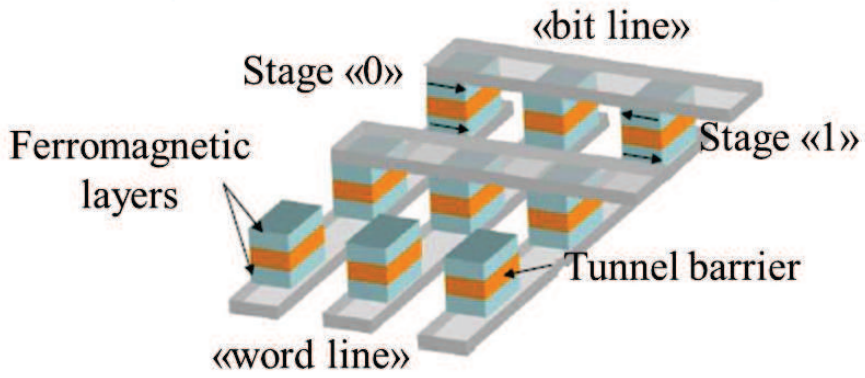

Figure 1-8. Schematic representation of the components of M-RAM magnetic memories.

6.2 Ferroelectric memories: Fe-RAM

The memory unit in the Fe-RAM[11] systems (Ferroelectric Random Access Memories) consists of a ferroelectric capacitance confined between two conductive electrodes. The application of a voltage allows control of the bias (positive or negative) and hence the state "0" or "1" of the capacitance. A transistor allows electrical isolation of each memory element and therefore a selective addressing of the electrical pulses. The voltage is applied to the ferroelectric capacitance *via* the "drive line", the transistor is controlled by the "word line" and the state of the cell is detected by the "bit line". The main disadvantage of this type of device resides in the fact that the read process is destructive. In addition, the fatigue phenomenon linked to the ferroelectric material is a limit to the number of cycles achievable.

6.3 Magnetoelectric memories ME-RAM

The insertion of magnetoelectric materials in which it is possible to control the direction of the magnetization by an electric field allows considering a new type of memory: magnetoelectric memory (ME-RAM). The ME-RAMs described by M. Bibes *et.al.* [13] (Figure 1-9) combine the advantages of Fe-RAMs and MRAMs, that is to say the reduction in energy costs for writing, non-destructive nature of read and absence of fatigue phenomena. Important research is currently underway in order to realize such devices recently and control of magnetization by an electric field was produced at room temperature [14].

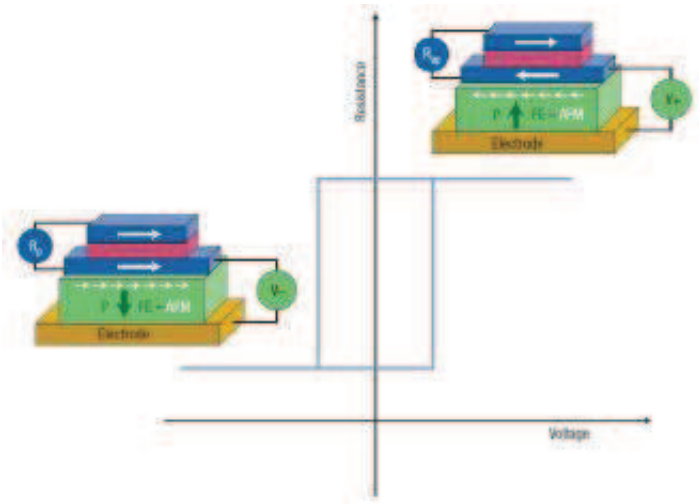

Figure 1-9. A scheme of a magnetoelectric memory element, a sudden change in resistance is obtained by changing the voltage across the device [13].

7. Materials of interest

The materials eligible for multiferroism should have peculiar symmetries and therefore crystallize in certain type of space group [15]. This reduces a lot the list of candidates.

The most studied ones are presented in *Table 1-1*.

Table 1-1. The most studied materials for multiferroicity

Compound	Magnetic order	T_C/T_N (K)	Electric order	T_C (K)
$BiMnO_3$ [16]	FM	105	FE	750
$BiFeO_3$ [17]	**AFM**	**640**	**FE**	**1100**
$YMnO_3$[18]	AFM	77	FE	910
$HoMnO_3$[19]	AFM	77	FE	870
$TbMnO_3$ [20]	AFM	41	FE	28
RMn_2O_5 [21]	AFM	< 30	FE	< 30
$Ni_3B_7O_{13}I$[22]	FM	64	FE	64
PFT-PZT [23]	AFM	133-180	FE	250
PFN-PZT [23]	AFM	600	FE	585
$Sr_3Co_2Fe_{24}O_{41}$ [24]	FM	670	FE	710
β-$NaFeO_2$ [25]	To explore	450	FE	To explore

The only single phased room temperature magnetoelectric material available for this concept for the moment is $BiFeO_3$, and it has an antiferromagnetic character. This requires its coupling with an additional ferromagnetic electrode, usually CoFe.

Recent studies present new materials such as $PbFe_{0,5}Ta_{0,5}O_3 - PbZr_{0,53}Ti_{0,47}O_3$ (PFT-PZT), $PbFe_{0,5}Nb_{0,5}O_3 - PbZr_{0,53}Ti_{0,47}O_3$ (PFN-PZT), $Sr_3Co_2Fe_{24}O_{41}$, β-$NaFeO_2$ showing room temperature multiferroicity with non-zero magnetization. However the synthesis of complex $Sr_3Co_2Fe_{24}O_{41}$ in thin films has never been performed and certainly is a major challenge. The magnetization of all these compounds is also rather low and not really suitable for application. Finally, it is to be noted that the structure of β-$NaFeO_2$ shows high level of instability.

8. Extrinsic multiferroism

There is a possibility to create devices that will use the coupling between a ferroelectric material and a magnetic material through piezoelectricity and piezomagnetism. Indeed, it is possible to apply an electric field to the first and to put it to a deformation, then forward it to the second material which will undergo a magnetization change or the anisotropy piezomagnetism. A lot of research has been conducted for this purpose [26], [27]. However, the presence of the substrate can partly prevent deformation of the ferroelectric, leading to lower magnetoelectric coefficients.

Zheng *et al.* [28] demonstrated the possibility of producing nanostructured columnar materials. Selecting immiscible material (such as a perovskite phase and a spinel phase, for example), it is possible to create a structure composed of pillars embedded in a matrix. In the first experimental example, columns of $CoFe_2O_4$ had been incorporated into a matrix of $BaTiO_3$. All showed a high magnetoelectric coupling. In this type of compound, the action of the relevant constraint is generally higher because the substrate contribution is almost non-existent. New structures using other materials were developed later [29; 30], in particular pulsed laser ablation, which proved to be the technique of choice for the realization of such structures [31; 32].

While there may be disagreement lattice mismatch between two phases, it may in some cases prove that the interface is coherent, *i.e.* it is impossible to detect the presence of dislocations that usually occur at the interfaces. In other words, the transformation is called isostructural, *i.e.* the crystalline symmetry is preserved. In these materials a very interesting electromechanical response was observed [33] and this undeniable hysteretic behavior, for phase transitions like martensitic transition. In particular, it was observed that the high electromechanical response could be observed according to many "paths", including some where the reversal of the polar state of the material was not necessary.

However, in this thesis we will focuse on single phased multiferroic and/or magnetoelectric materials.

In this class of materials, an interesting candidate which has realistically usable properties is the gallium ferrite $Ga_{2-x}Fe_xO_3$. It is said to be polar, has shown a ferrimagnetic behavior at room temperature for $x>1.3$ with a magnetization of 100 emu/cm^3. This material will be the subject of investigation of this work.

Bibliography

[1] Hill, N. A., Journal of Physical Chemistry B 104 (2000) 6694.
[2] De Gennes, P.-G., Physical Review 118 (1960) 141.
[3] Valasek, J., Physical Review 17 (1921) 475.
[4] De Mathan, N., Husson, E., Calvarn, G., Gavarri, J., Hewat, A. and Morell, A., Journal of Physics: Condensed Matter 3 (1991) 8159.
[5] Mihailova, B., Bismayer, U., Güttler, B., Gospodinov, M. and Konstantinov, L., Journal of Physics: Condensed Matter 14 (2002) 1091.
[6] Zhou, C. and Liu, X., Journal of Materials Science 43 (2008) 1016.
[7] Bouquin, O., Lejeune, M. and Boilot, J. P., Journal of the American Ceramic Society 74 (1991) 1152.
[8] Spaldin, N. A. and Fiebig, M., Science 309 (2005) 391.
[9] Smolenskii, G. A. and Chupis, I. E., Uspekhi Fizicheskikh Nauk 137 (1982) 415.
[10] Schmid, H., Journal Of Physics-Condensed Matter 20 (2008) 434201.
[11] Rabe, K. M., Nature 449 (2007) 674.
[12] Moodera, J. S., Kinder, L. R., Wong, T. M. and Meservey, R., Physical Review Letters 74 (1995) 3273.
[13] Bibes, M. and Barthelemy, A., Nature Materials 7 (2008) 425.
[14] Chu, Y. H., Martin, L. W., Holcomb, M. B., Gajek, M., Han, S. J., He, Q., Balke, N., Yang, C. H., Lee, D., Hu, W., Zhan, Q., Yang, P. L., Fraile-Rodriguez, A., Scholl, A., Wang, S. X. and Ramesh, R., Nature Materials 7 (2008) 478.
[15] Schmid, H., Journal of Physics-Condensed Matter 20 (2008) 434201.
[16] Kimura, T., Kawamoto, S., Yamada, I., Azuma, M., Takano, M. and Tokura, Y., Physical Review B 67 (2003) 180401.
[17] Bibes, M. and Barthélémy, A., Nat. Mater 7 (2008) 425.
[18] Van Aken, B. B., Palstra, T. T., Filippetti, A. and Spaldin, N. A., Nature Materials 3 (2004) 164.
[19] Rout, P., Pradhan, S., Das, S. and Roul, B., Physica B: Condensed Matter 407 (2012) 2072.
[20] Kimura, T., Goto, T., Shintani, H., Ishizaka, K., Arima, T. and Tokura, Y., Nature 426 (2003) 55.
[21] Noda, Y., Kimura, H., Fukunaga, M., Kobayashi, S., Kagomiya, I. and Kohn, K., Journal of Physics: Condensed Matter 20 (2008) 434206.
[22] Ascher, E., Rieder, H., Schmid, H. and Stössel, H., Journal of Applied Physics 37 (1966) 1404.
[23] Sanchez, D. A., Kumar, A., Ortega, N., Martinez, R. and Katiyar, R. S., Integrated Ferroelectrics 124 (2011) 61.
[24] Kitagawa, Y., Hiraoka, Y., Honda, T., Ishikura, T., Nakamura, H. and Kimura, T., Nature Materials 9 (2010) 797.
[25] Viret, M., Rubi, D., Colson, D., Lebeugle, D., Forget, A., Bonville, P., Dhalenne, G., Saint-Martin, R., André, G. and Ott, F., Materials Research Bulletin 47 (2012) 2294.
[26] Ryu, J., Carazo, A. V., Uchino, K. and Kim, H.-E., Japanese Journal of Applied Physics 40 (2001) 4948.
[27] Ryu, S., Park, J. H. and Jang, H. M., Applied Physics Letters 91 (2007) 142910.
[28] Zheng, H., Wang, J., Lofland, S. E., Ma, Z., Mohaddes-Ardabili, L., Zhao, T., Salamanca-Riba, L., Shinde, S. R., Ogale, S. B., Bai, F., Viehland, D., Jia, Y., Schlom, D. G., Wuttig, M., Roytburd, A. and Ramesh, R., Science 303 (2004) 661.
[29] Murakami, M., Fujino, S., Lim, S. H., Long, C. J., Salamanca-Riba, L. G., Wuttig, M., Takeuchi, I., Nagarajan, V. and Varatharajan, A., Applied Physics Letters 88, (2006) 112505.

[30] Zheng, H., Zhan, Q., Zavaliche, F., Sherburne, M., Straub, F., Cruz, M. P., Chen, L. Q., Dahmen, U. and Ramesh, R., Nano Letters 6 (2006) 1401.
[31] Ryu, H., Murugavel, P., Lee, J. H., Chae, S. C., Noh, T. W., Oh, Y. S., Kim, H. J., Kim, K. H., Jang, J. H., Kim, M., Bae, C. and Park, J. G., Applied Physics Letters 89 , (2006) 102907.
[32] Wan, J. G., Weng, Y. Y., Wu, Y. J., Li, Z. Y., Liu, J. M. M. and Wang, G. H., Nanotechnology 18, (2007) 465708.
[33] Zeches, R. J., Rossell, M. D., Zhang, J. X., Hatt, A. J., He, Q., Yang, C. H., Kumar, A., Wang, C. H., Melville, A., Adamo, C., Sheng, G., Chu, Y. H., Ihlefeld, J. F., Erni, R., Ederer, C., Gopalan, V., Chen, L. Q., Schlom, D. G., Spaldin, N. A., Martin, L. W. and Ramesh, R., Science 326 (2009) 977.

Introduction to $Ga_{2-x}Fe_xO_3$

1. Crystallographic structure
2. Synthesis in bulk and thin films
3. Magnetic properties
4. Electric properties
5. Magnetoelectric properties
6. Tuning the GFO properties by doping
7. Conclusion

Bibliography

1. Crystallographic structure

The $GaFeO_3$ compound was discovered by Remeika in 1960.[1] It is then described as a compound of orthorhombic symmetry of equimolar composition of gallium and iron. In 1965, Abrahams *et al*. [2], analyzing single crystals of $GaFeO_3$, established that the compound adopts an orthorhombic structure and crystallizes in the non-centrosymmetric space group $Pc2_1n$ with lattice parameters a_{GFO} = 8.7512 ± 0,0008Å, b_{GFO} = 9.3993 ± 0,0003Å and c_{GFO} = 5,0806 ± 0.0002Å. In this space group, there is only a general position of multiplicity 4. O^{2-} anions are spread across six different sites rated O1-O6 (see *Table 2-1*). They are arranged according to a double hexagonal close packed stocking ABAC along the *b* axis. The Fe^{3+} and Ga^{3+} cations are located in three non-equivalent octahedral sites named Fe1, Fe2, Ga2 and a tetrahedral site named Ga1. The Ga1 tetrahedra are described as oriented along the direction of the *b* axis, regular with metal-oxygen distances of 1,846 ± 0,005Å. The Ga2 octahedra are irregular with average metal-oxygen distances of 2,026 ± 0.004 Å. Octahedral Fe1 and Fe2 sites are even more distorted with average distances of 2.036 ± 0.004 Å and 2.049 ± 0.004 Å.

Table 2-1 Positions of atoms in $GaFeO_3$ in the space group $Pc2_1n$ [2].

Site	x	y	z
Ga1	0,1519 ± 0,0002	0	0,1773 ± 0,0003
Ga2	0,1602 ± 0,0002	0,3084 ± 0,0002	0,8102 ± 0,0003
Fe1	0,1529 ± 0,0003	0,5838 ± 0,0002	0,1911 ± 0,0004
Fe2	0,0340 ± 0,0002	0,7956 ± 0,0003	0,6776 ± 0,0004
O1	0,3242 ± 0,0009	0,4290 ± 0,0008	0,9748 ± 0,0020
O2	0,4879 ± 0,0010	0,4350 ± 0,0008	0,5187 ± 0,0019
O3	0,9958 ± 0,0009	0,2000 ± 0,0010	0,6569 ± 0,0020
O4	0,1564 ± 0,0010	0,1966 ± 0,0009	0,1534 ± 0,0018
O5	0,1696 ± 0,0010	0,6724 ± 0,0011	0,8487 ± 0,0021
O6	0,1684 ± 0,0012	0,9390 ± 0,0011	0,5146 ± 0,0023

The structure of $GaFeO_3$ and positions of the atoms are shown on Figure 2-1.

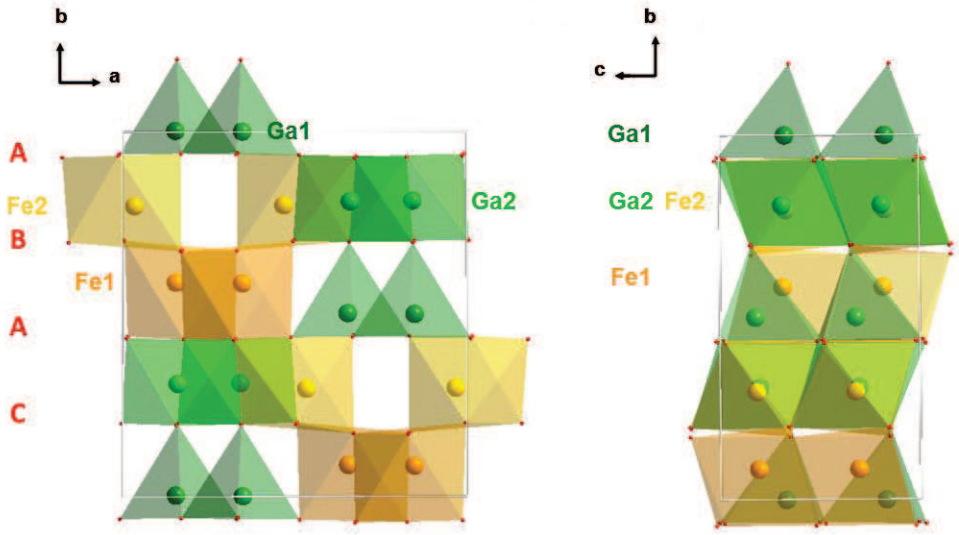

Figure 2-1. The *P*c2$_1$n $Ga_{2-x}Fe_xO_3$ structure.

GFO presents an important cationic disorder which has important consequences. One would expect the Fe1 and Fe2 sites to be filled only with iron, and the Ga1 and Ga2 sites only filled with gallium. However, in [3] Mössbauer spectroscopy shows that there are Fe^{3+} cations in 3 different octahedral sites. It is clear that the type and conditions of synthesis (temperature annealing, tempering) have a major influence on these occupations.

The results found in the literature are summarized in *Table 2-2*.

Table 2-2. Site occupations depending on the type of synthesis.

Type	Stochiometry	Method	T_N(K)	Fe/Ga in Ga1	Fe/Ga in Ga2	Fe/Ga in Fe1	Fe/Ga in Fe2
Monocrystal [4]	$Fe_{1,11}Ga_{0.89}O_3$	Flux	290	14/86	32/68	83/17	89/11
Monocrystal [5]	$Fe_{1,0}Ga_{1,0}O_3$	FZ	<230	10/90	24/76	84/16	83/17
Monocrystal [6]	$Fe_{1,0}Ga_{1,0}O_3$	Flux	260	0/100	35/65	83/17	83/17
Monocrystal [7]	$Fe_{1,0}Ga_{1,0}O_3$	FZ	205	0/100	54/46	75/25	73/27
Powders [8]	$Fe_{1,0}Ga_{1,0}O_3$	SR	190	20/80	55/45	70/30	55/45
Powders [8]	$Fe_{1,0}Ga_{1,0}O_3$	SG	>300	4/96	75/25	51/49	72/28
Powders [9]	$Fe_{1,0}Ga_{1,0}O_3$	SR	-	9/91	83/17	42/58	66/34
Powders [9]	$Fe_{1,0}Ga_{1,0}O_3$	SG	-	8/92	96/4	45/55	52/48
Powders [10]	$Fe_{1,0}Ga_{1,0}O_3$	SR	210	12/88	68/32	62/38	58/42

where FZ – floating zone, SR- solid state reaction, SG – sol gel.

It is estimated[11] that the thermal energy and the defects of the structure are the only sources of cationic disorder in GFO. Energetically, the disordered state is not the most stable, but the interchange is very likely between Fe2 site and Ga2 sites. Band structure calculations show that the exchange iron/gallium between Fe2 and Ga2 sites only modifies the system energy by 1 meV. First principle calculations have shown that in the case of an excess of Ga (x = 0.5) the gallium surplus will be located in the Fe2 sites, while for higher values of Fe (x=1.5) one observed the migration of iron in to Ga2 [12].

The Ga1 tetrahedral site is mostly occupied by gallium. This trend had already been reported by Remeika [13] , and can even be found when trying to force the gallium to leave this site, *e.g.* when it competes with smaller cation, for example Al^{3+}. A study [14] presents a total absence of iron in the tetrahedral site. Another study, also carried on single crystals, corroborates the absence of iron in the tetrahedral site, and states that there is no preference for the Ga between Fe1 and Fe2 sites in the case of a gallium surplus [7].

The space group into which GFO crystalizes, number 33, has different settings. The one chosen historically by Remeika[1] and Rado[15] in their first publications on GFO is $Pc2_1n$, with c<a<b. However, numerous crystallographic softwares, including Carine, which we use for the reciprocal space simulations, use $Pna2_1$ as the main setting, with a<b<c. We will therefore use the $Pna2_1$ setting when working on the reciprocal lattice of GFO, both for X-ray diffraction and transmission electronic microscopy. Use of the $Pna2_1$ setting will be indicated as subscript of the crystallographic directions or planes. The relationships between the two settings rely on a circular permutation of the cell parameters and are described in Figure 2-2.

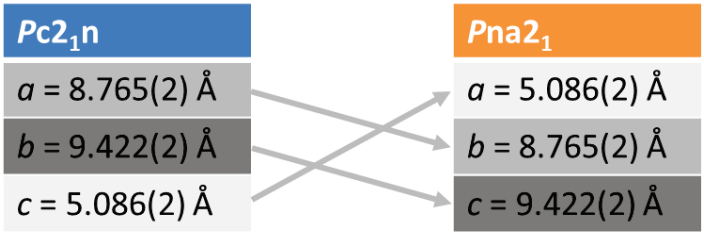

Figure 2-2. Relationships between the two mainly used settings for space group 33, with the cell parameters of GFO1.4[16].

Arima *et al.*[5] determine the evolution of the lattice parameter of $Ga_{2-x}Fe_xO_3$ compound with the increase of iron in the structure in single crystals for 0.8 <x <1.2, by neutron diffraction. This study highlights an isotropic lattice parameters increase with the value of x due primarily to the difference in ionic radii between Fe^{3+} and Ga^{3+}, 65 and 62 pm,

respectively. Later, Lefevre *et al.* [16] did studies on $Ga_{0.6}Fe_{1.4}O_3$ and determined the cell parameters of the x=1.4 compound. The variation of the cell parameters with the composition are summarized in *Table 2-3*.

Table 2-3. Lattice parameters of $Ga_{2-x}Fe_xO_3$ compounds with ($0.8 \leq x \leq 1.4$) determined by synchrotron diffraction on single crystals for $0.8 \leq x \leq 1.2$ and polycrystalline samples for x=1.4[16] at room temperature.

Composition,x	0,8	1,0	1,2	1,4
a (Å)	8,7358(13)	8,7442(10)	8,7515(15)	8,765(2)
b (Å)	9,3771(14)	9,3927(11)	9,4012(16)	9,422(2)
c (Å)	5,0767(7)	5,0823(5)	5,0865(9)	5,086(2)

The orthorhombic structure adopted by GFO is isomorphous to that of ε-Fe_2O_3[17]. One should note the similarities between this structure and two other structures which are more stable in the case of iron oxides, α-Fe_2O_3 and γ-Fe_2O_3. α-Fe_2O_3, of rhombohedral corundum structure *R*-3c, is the most common form for iron oxide (Figure 2-3(a)). The structure is made of hexagonal close packed ABAB oxygens stacking, and has four octahedral sites per cell, of which 2/3 are occupied by Fe^{3+}. This phase naturally in mineral form (hematite), has an antiferromagnetic behavior under 260 K (Morin transition temperature), and is a weak ferromagnet above this temperature until its Curie temperature of 950 K. The low symmetry of the cationic sites allows a spin-orbit coupling which causes canting moments when they are in the plane perpendicular to the c axis. At the Morin temperature, a change of anisotropy causes the alignment of the moments along the *c*-axis.

γ-Fe_2O_3 has a cubic structure (Figure 2-3(b)). It consists of a face centered cubic close packed ABCABC oxygen stacking, with two octahedral (1/6 of which are left vacant) and a tetrahedral sites. The phase is actually metastable and transforms into hematite at high temperatures. This structure is the one adopted by the Fe_3O_4 oxide mineral found in natural form (magnetite). This compound is ferromagnetic.

ε-Fe_2O_3. (Figure 2-3(c)) to which GFO is isostructural, is not the most stable for pure iron oxide. It has however recently been obtained in thin films [18] and has also shown some interesting properties in the field of multiferroism. Relying on a double hexagonal compact ABAC oxygen packing and having 3 octahedral sites and one tetrahedral one, this phase is intermediate between the γ and α phases.

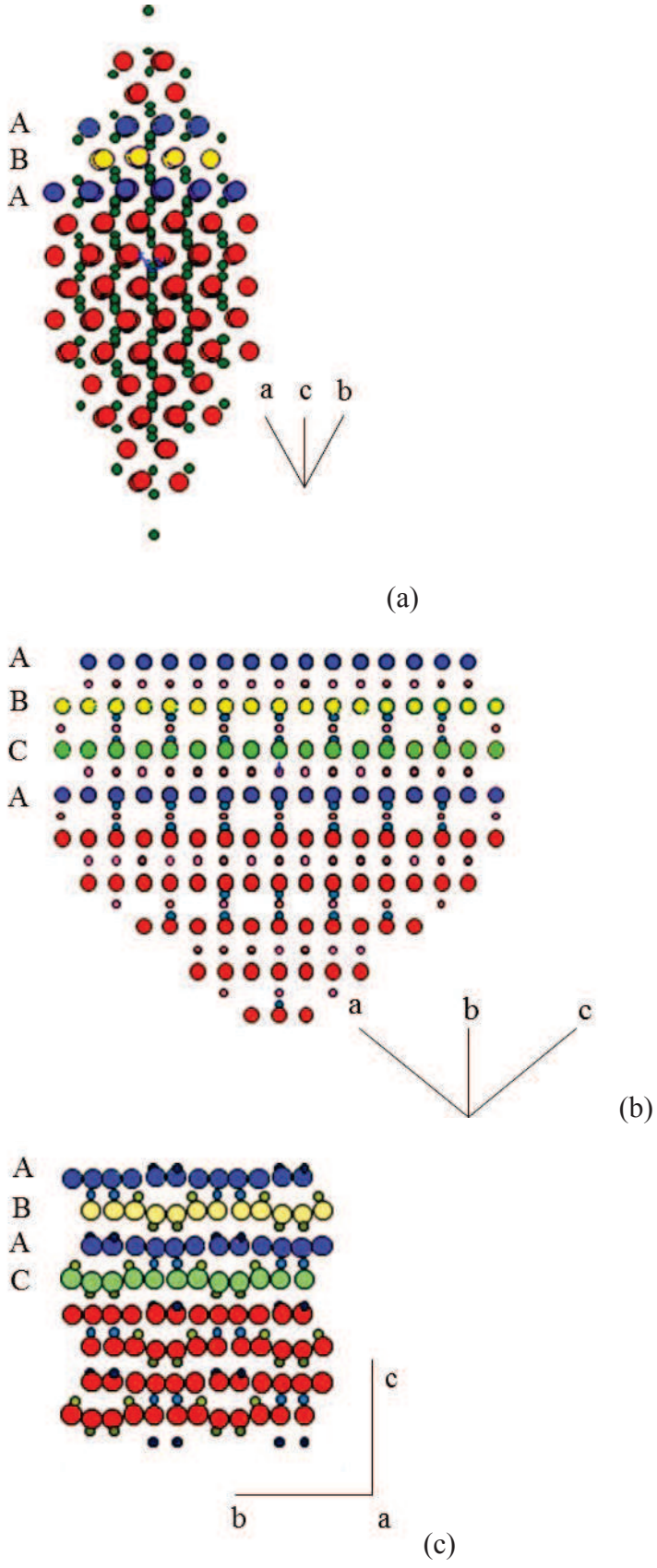

Figure 2-3. Projections of a) α-Fe_2O_3 b) γ-Fe_2O_3 c) ε–Fe_2O_3 structures showing the 3 different oxygen stackings in each case.

2. Synthesis in bulk and thin films

Depending on the desired sample, several synthetic methods have been used for the synthesis of $Ga_{2-x}Fe_xO_3$. In the case of single crystals, two techniques were mainly used: flux growth [6; 19] and growth through floating zone (FZ) method [5; 7]. The first consists in dissolving the elements we want to use in a solvent. The solution is then placed in a crucible itself sealed in a quartz bulb. The crucible is heated, and then upon cooling there is precipitation of species taking place. The advantage of the technique is that it yields faceted crystals, which do not require polishing. The disadvantage is the relatively small size of the crystals obtained. In the second technique, known as the melt zone, a seed oriented in a preferential direction is fixed on a support. Using a mobile heating system, a solid / liquid interface is created, resulting in both growth of the crystal according to the selected crystallographic direction and purification of the material at the same time.

For the formation of polycrystalline powders, two major techniques have been reported in the literature. First is the ceramic process, where the chemical reaction takes place in solid phase. The powders of the compounds are mixed, crushed and then heated to high temperature to obtain the formation of the desired phase. The second possible technique is the sol-gel method. This soft chemistry method in the case of $GaFeO_3$ consists in mixing precursors of iron and gallium as chlorides or nitrides in the presence of citric acid and ethylene glycol. The gels obtained are heated to 400°C and the powders are filtered and annealed at different temperatures.

The variety of production techniques entails certain flexibility allowing accessibility to various compositions. The material properties critically depend on the used method, and the synthesis conditions. The method of synthesis of powders has, for example an influence on the size of the formed particles. While 75 nm grains can be obtained by sol-gel, 200 nm ones are obtained by the ceramic method[20]. As shown in a sol-gel based method[21] increasing the annealing temperature from 800 to 1400°C leads to a better crystallinity, and lower cell parameters[20]. Finally, the magnetic properties are highly dependent on experimental procedures, in particular the magnetic transition temperature. For a given composition in iron and gallium, the ordering temperature may vary with the method of preparation used by several tens of degrees.

The first $GaFeO_3$ thin films were made in 2005 by Kundaliya *et al.*[22]. The layers were deposited on yttria stabilized zirconia (YSZ) substrates oriented (100) or on YSZ buffered Si substrate (001) by laser ablation from a sintered target of $GaFeO_3$. Obtaining satisfying quality layers with an orientation (0*k*0) opened the way to the magnetic characterizations but also to the optical characterization of GFO thin films. In addition, these studies demonstrated the compatibility of $GaFeO_3$ with silicon technology. On these substrates, the layers have easy magnetization direction in the film plane. The polarization direction *b* is perpendicular to the surface, the easy magnetization along *c*, if one considers the (0*k*0) growth. No information is given about a possible anisotropy in the plane of the layers, and magnetic measurements in the plane are carried along an arbitrary axis indexed *c* $GaFeO_3$.

Studies on GFO material made of thin layers remained in the past five years quite rare. GFO films deposited directly on YSZ (100) were studied by ellipsometry [11]. Parallel research was done by [23] where the band gap was estimated as 2.28 eV. Although refinements have been made on a single oscillator, making the results questionable, the results are substantially the same as those obtained by Kalashnikova [24], *i.e.* the optical transitions into play involve 2p oxygen and 3d Fe(III) levels. In addition, a better balance between the measurements and refinements made is observed when the cationic disorder is introduced (mostly between Fe2 and Ga2) and a stress due to the epitaxy.

Other possible substrates for GFO deposition were studies in [25], using MgO(001) and Al_2O_3 (0001) substrates. Observing relatively large lattice mismatch parameters of 4.8% and 6.3% for MgO and Al_2O_3, respectively, it was difficult to obtain good quality of GFO layers. The nature of the substrate seemed to influence the value of the optical gap of GFO, which were found to be 2.92 and 3 eV for depositions on MgO and Al_2O_3, respectively.

The first direct measurements of electric polarization as a function of the electric field applied to (0*k*0) oriented $GaFeO_3$ films are made possible by the use of $SrTiO_3$ substrates made conductive by doping with Nb [25]. The layers, however, have poor crystal quality, probably due to the large lattice mismatch (8.2%). The authors conclude on the ferroelectricity of the thin layers but the ferroelectric hysteresis cycles obtained (Figure 2-4) are not saturated. The appearance of these cycles (rounded shape and absence of saturation) recalls the observations made by Scott [26] in its warning article. Moreover, these polarization measurements require, unlike magnetic measurements, the use of electric contacts. In this case, it may form double-diode circuits that will have a ferroelectric behavior. Even acquiring a polarization *versus* electric field saturated hysteresis curve with an inflection point is not a sufficient condition to conclude that the material shows ferroelectricity [27], and the majority

of publications have at least one capacitance *versus* voltage curve with 2 peaks, characteristic of a reversal of the polarization.

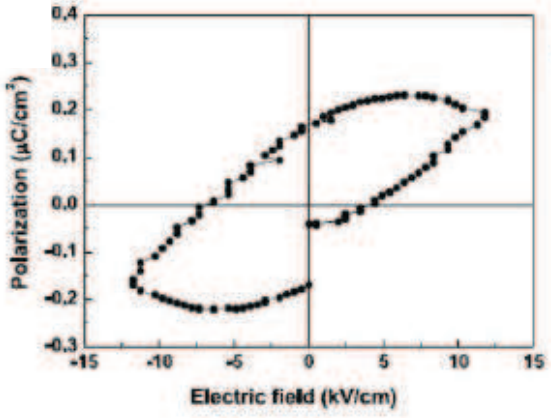

Figure 2-4. Electrical characterization of thin layers of $GaFeO_3$ hysteresis loops of polarization versus electric field applied [25].

The pulsed laser deposition of GFO thin films of high crystalline quality was optimized in previous works carried out in our research team [28], [29], [30]. The films are perfectly (0*k*0) oriented for all compositions. The lattice parameters of the GFO thin films are consistent with those observed for bulk material and no secondary phase was observed. The $Ga_{2-x}Fe_xO_3$ thin films are ferrimagnetic at room temperature when x> 1.2. The saturation magnetization is of the same order of magnitude as that observed for the bulk material. The Neel temperatures of the films are similar to those of the bulk for all compositions ($0.8 \leq x \leq 1.4$) (Figure 2-5).

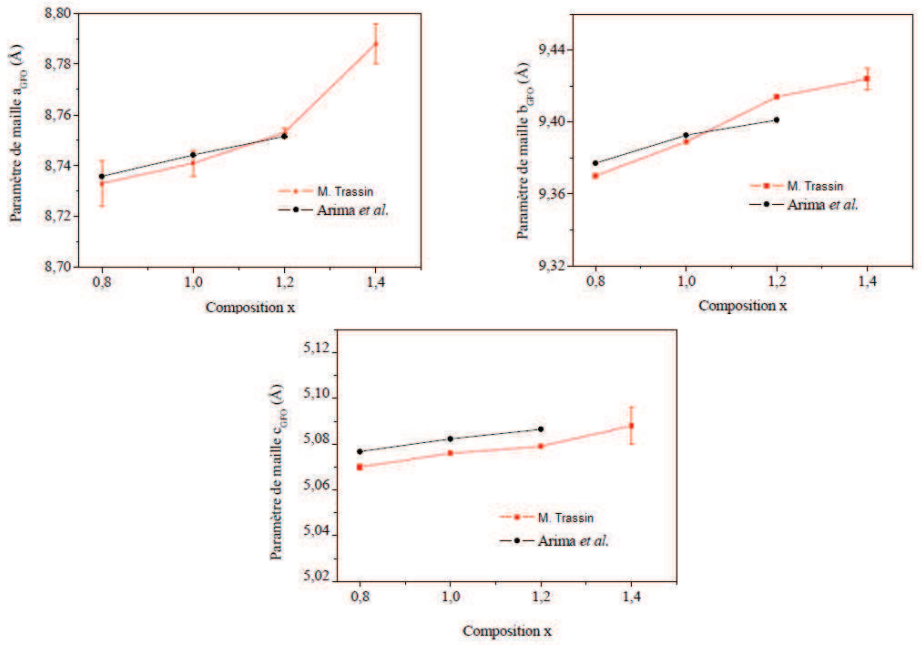

a)

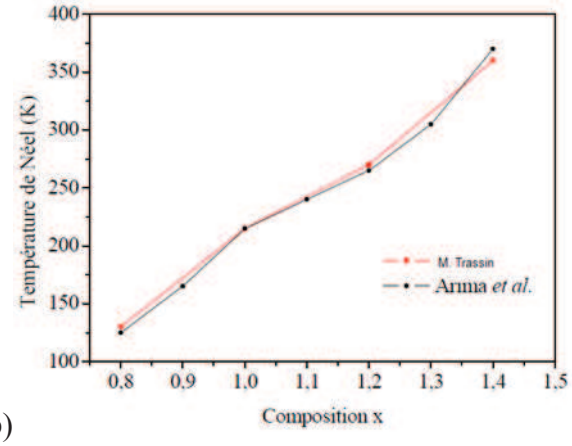

b)

Figure 2-5. Variation in (a) the lattice parameters and b) the Neel temperature with the composition x in $Ga_{2-x}Fe_xO_3$ [29].

The values of leakage currents, however, were too high to allow meaningful electrical characterizations, neither macroscopic nor microscopic. Numerous studies were performed on doping the material with various elements in order to decrease those leakage currents. A work previously done in our research team [31] showed that introducing 2% of Mg^{2+} into GFO structure in thin films prevents a hopping mechanism between Fe^{3+} to Fe^{2+} that has an effect

on the electrical resistivity of GFO thin films. Ferroelectric hysteresis loops could then be measured (Figure 2-6).

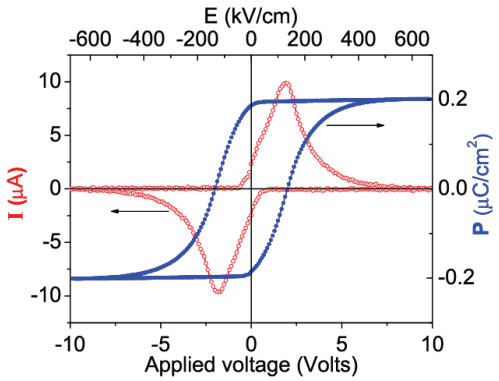

Figure 2-6. Ferroelectric hysteresis loop P(E) and switching current I(V) of the 2% Mg-doped $Ga_{0.6}Fe_{1.4}O_3$ [31].

3. Magnetic properties

The observation of a non-zero magnetization for the newly discovered GFO pushed Remeika to define it as a ferromagnet with an observed Curie temperature of 260 K [13]. He also showed that the magnetic ordering transition could take place at temperatures above room temperature when the Fe / Ga ratio increases. Bertaut *et al.*[32], studying the magnetic structure of GFO single crystals by neutron diffraction, showed in 1966 a strong antiferromagnetic coupling between the Fe1 and Fe2 sites, on the one hand, and the Fe1 sites and Ga2 other hand, with super exchange interactions characterized by angles of 180 °. In 1968, Levine *et al.* [33] describe the evolution of the magnetic properties of the $Ga_{2-x}Fe_xO_3$ compound in terms of x and determine a Néel temperature of about 240 K and a magnetization of 0.789 μB per iron atom at 4.2 K [33] for the compound $GaFeO_3$. The ordering temperature is higher than room temperature for x> 1.2 (Figure 2-7). These results were confirmed by [34]. Lefevre *et.al* [35] indicate that the magnetic properties of $Ga_{2-x}Fe_xO_3$ can be strongly enhanced through increasing x, without deteriorating the electric polarization within the structure. Moreover, magnetic structure and displacements of Fe1 and Fe2 from the center of their octahedron along the b axis suggest that a magnetoelectric coupling still occurs with the increasing iron content.

Arima *et al*. [5] confirmed in 2004 the results published by Bertaut *et al.*[32], that the magnetic moment carried by the Fe^{3+} cations in the Ga2 site is aligned parallel with that

carried by the cations located in the Fe2 sites oriented antiparallel to that worn by the cations in the Fe1 site.

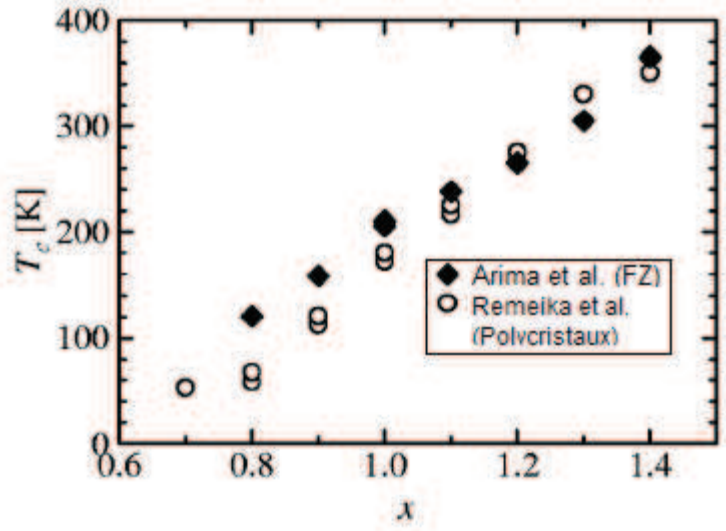

Figure 2-7. The evolution of Néel temperature of the $Ga_{2-x}Fe_xO_3$ compound according to x [5].

The measured values of the moments of Fe in the Fe1 sites, Fe2 and Ga2 sites are -3.9, 4.5, and 4.7 μB per atom of Fe, respectively. The population of Fe^3 + cations being greater on the Fe2 and Ga2 sites than in the Fe1 and Ga1 sites, the antiferomagnetism isn't compensated and an overall ferrimagnetic behavior is observed even for x=1. For the composition x = 1, the saturation magnetization value obtained at 5 K is between 0.78 μB / Fe [33] and 0.87 μB / Fe [6] and depends on the technique used for the synthesis of single crystals. The *ab initio* calculations in [12; 36] describe the magnetic structure of GFO as uncompensated antiferromagnet, which is due to two-thirds of oxygens are non-zero magnetic moment demonstrated hybridization of orbitals between iron and oxygen. One group [37] contradicts the fact that alignment is purely antiferromagnetic along *c* and reports the existence of a moment canted of 25 ° along the axis with respect to the *c* axis.

Whatever the method of synthesis is, a "pinch" [21; 38] is observed in hysteresis cycles, indicating the presence of non-coupled magnetic layers of different hardness. This has initially been identified in ε-Fe_2O_3 [18], where the possibility of a secondary phase at the origin of this behavior was discarded by multiple analyzes. For GFO, there doesn't seem to be a relationship between the existence of that pinch on MH curves and the composition. All hysteresis curves published to date do not have this singularity and its origin is debatable. Moreover, a potential spin glass behavior was observed in [39]. Such frustrations could also explain the presence of pinching in the hysteresis cycles. Another study offers as an

explanation that the four sites anisotropy values are very different [40]. The presence of four separate subnetworks corresponding to the four cationic sites is detected by Mössbauer spectroscopy: the tetrahedral site turns out to be milder than the other three sites. The authors of this publication show that the pinch in the magnetic areas is not present for samples prepared at higher temperatures, where the level of iron in the tetrahedral site is low [10] . However, it remains difficult to consider that the sites can be correlated in a magnetic structure governed by super-exchange interactions. The magnetic structure of GFO is probably more complicated than it seems anyhow since some studies show the persistence of ferrimagnetic short-range spin correlations above the ordering temperature [41].

4. Electric properties

Electrical measurements on GFO have established a semiconductor behavior [42], with a resistivity of between 3 and 60 MΩ.m for temperatures between 360 K and 260 K. The thermally activated transport mechanism obeys an Arrhenius law, with an activation energy value of Ea = 0.675 eV, well below the value of the gap estimated at 2.7 eV [24] or 2.28 eV [43]. Although belonging to the $Pc2_1n$ space group, allowing ferroelectricity, there is no ferroelectric behavior observed on single crystals. This compound was defined as pyroelectric-that is having an electric polarization, non reversible. The origin of the polarization is still discussed and two assumptions are made. Abrahams *et al*. [2] explain the possible polarization by a displacement of Ga^{3+} cations in the tetrahedral site Ga1. One of the Ga1-O bonds of the tetrahedron Ga1 is almost parallel to the *b* axis. A pressure along this direction may cause a compression of this bond, thus inducing a dipole and therefore explain piezoelectricity observed by Remeika *et al.*

Abrahams *et al.* [2] observed that with increase of x, the occupation of the Ga2 sites by Fe^{3+} cations increases. The presence of iron in these sites can lead to a significant distortion of the octahedral Ga2 site. The position of the common oxygen atom between the octahedral Ga2 and tetrahedral Ga1 sites is changed. This results in a deflection of the Ga1-O bond with respect to the polar axis *b*. Pressure along this polar axis tends to rotate the Ga1-O bond more than to compress it. The bias is due to the displacement of Ga^{3+} in the tetrahedron, and explains why increased x results in a reduction in the polarization and the Curie temperature. According to Arima *et al.* [5] the occurrence of electric polarization is due to displacement of the Fe^{3+} ions in the octahedral Fe1 and Fe2 sites distorted. The movement along the *b* axis of the Fe^{3+} ions with respect to the center of the octahedra is measured by

neutron diffraction. This displacement is 0.26 and -0.11 Å for ions present in the Fe1 and Fe2 sites, respectively.

Spontaneous polarization values of GFO have been recently been evaluated by calculations based on the atomic positions determined by *ab initio* calculations. These calculations involve a path going through an intermediate centrosymmetric structure and give a much better estimate of the polarization. The value published by Roy *et al.* in [43] is falsely estimated as 59 μC /cm^{2}due to an error in the calculations and a correct value of 25 μC /cm^2 is given by Stoeffler [12]. In the case of GFO, the energy cost to move from the *P*c2$_1$n to the centrosymmetric structure is important,of about 0.5 eV, and it is difficult to consider a reversal of the experimental polarization along this path. Lefevre *et al.* in [16] think that there will be no decrease in the polarization for increase of x, when considering the position of the cations measured by neutron diffraction.

Experimental observation of a polarization in $GaFeO_3$ has been demonstrated for temperatures below 100 K by measuring a pyrocurrent on sintered pellets of GFO 1.0 [40]. According to these authors, the polarization would consist of two components: an irreversible one along z, and a second in the xy plane, of the order of 0.25 μC/cm². These results are subject to debate, as the measurement have been performed on polycrystalline samples. Another study performed in our research team [44] demonstrated for composition x=1.1 a polar state with an ordering temperature of about 580 K and a polarization of 33 μC /cm^2. For x=1.3 and 1.4 an electric relaxor behaviour was observed at room temperature. In thin films, a,much lower polarization value has been measured on 2% Mg-doped $Ga_{0.6}Fe_{1.4}O_3$ but it was shown reversible and presented fully saturated polarization loop [31].

The situation regarding the polarization of GFO and its eventuality is far from established. Nevertheless, it is important to remember that GFO belongs to a space group that would allow ferroelectricity and studies already showed hints of ferroelectric behavior.

5. The magnetoelectric properties

The magnetic group of $GaFeO_3$ authorizes the spontaneous presence of magnetization and spontaneous polarization [45]. Two components of the tensor of the linear magnetoelectric effect and α_{bc} α_{cb} are found to be nonzero. Rado [15] experimentally highlights the magnetoelectric coupling present in $GaFeO_3$ in 1964. He measured a polarization along the b axis (P // b) induced by a magnetic field along the c-axis (H // c) and a magnetization along the c axis (Dm //c) induced by an electric field along the b axis (E // b) as well as and the evolution of these quantities with temperature (Figure 2-8). This method allows qualitatively approaching the magnetoelectric coupling term α by measuring both linear effects, by applying either a magnetic H or electric E field. The coupling coefficient α was determined quantitatively in 2004 by Arima *et al.*. Its value of 2.10^{-11} s/m is one order of magnitude greater than that measured for the reference magnetoelectric compound Cr_2O_3 (α_{zz} for $Cr_2O_3 = 4{,}13.10^{-12}$s/m) [15; 46].

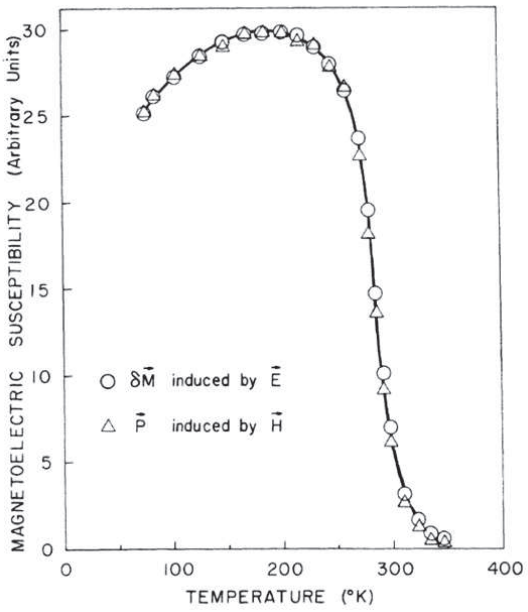

Figure 2-8. Temperature dependence of the magneto-electric susceptibility [15].

The magneto-electric effect is greatly reduced when the temperature is higher than the magnetic ordering temperature of the crystal, which is about 250 K for $GaFeO_3$. However it is not zero at room temperature.

Arima *et al.* [5] explain the contrast between the two α_{bc} α_{cb} coefficients as follows: in the H parallel to the *c* axis, case where the magnetic field is parallel to the Fe spin moments, the Fe2 moment increases while the Fe1 moment decreases (the moment stands for that in both spin and orbital sectors). If the displacement along the *b* axis of Fe2 is enlarged by the modulation of the magnetic moment, that of Fe1 is reduced, conversely. Since the displacements of Fe1 and Fe2 are opposite in direction with each other, the magnetic-field-induced modulation of the displacement obligingly affects the bulk polarization P_b as a result. In the case when magnetic moment is applied along the *b*-axis, the Fe1 and Fe2 moments are in two opposite directions (+b and –b), any direction of the moment is promoted by the field (Figure 2-9).

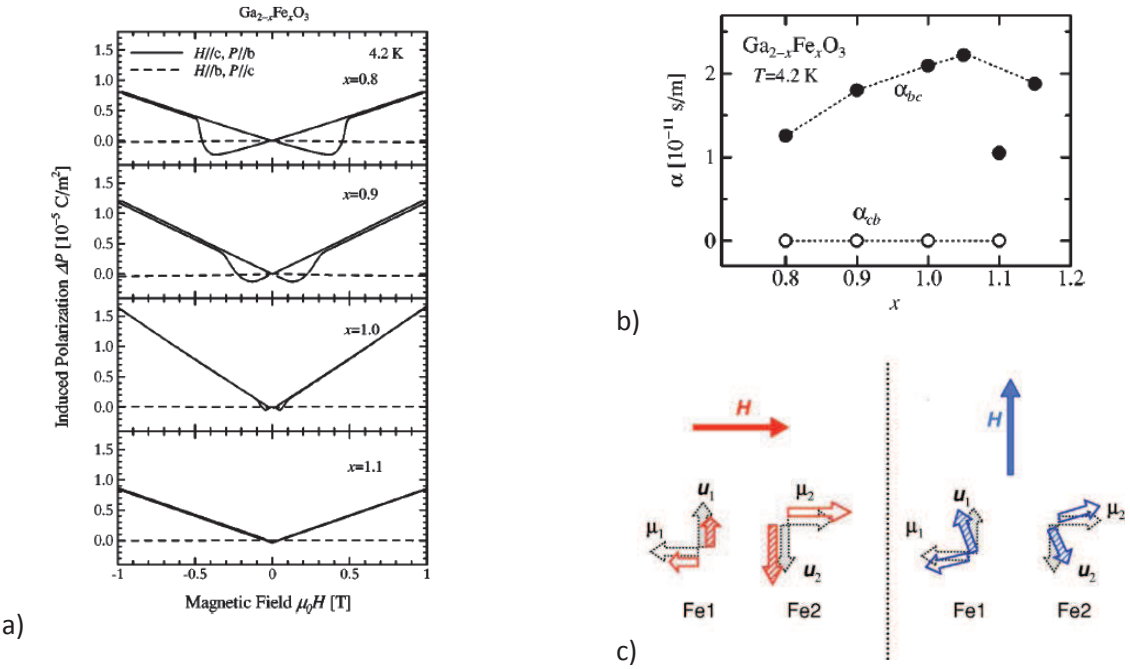

Figure 2-9. a) Measurement of magnetoelectric effect in crystals of $Ga_{2-x}Fe_xO_3$, b) changes in coupling coefficients with x, c) qualitative explanation of the differences between α_{bc} and α_{cb} [5].

The result of displacements with the same amplitudes, are opposed, which explains the absence of macroscopic polarization along the c-axis. A possible origin of the magnetoelectric coupling in $GaFeO_3$ is given by Rado [15] as the combination of the effects of piezoelectricity and magnetostriction.

Even though there had been many assumptions made, the cause of the coupling between the orders in GFO is still unknown.

6. Tuning the GFO properties by doping

The modification of the GFO properties has been considered through doping. Most studies focused on the problem of leakage currents and GFO (bulk and thin films) doping is performed with a wide range of elements *(Table 2-4)*.

Table 2-4. Various dopings performed on the gallium ferrite compound

Doping element	**Results**	**Ref.**
Al^{3+}	Increased magnetocapacitance Conservation of magnetism	[47]
In^{3+}	Decrease in T_N Forming another structure following a high doping rate	[48]
Mg^{2+}	Consequent reduction in leakage current in thin layer Low decrease in T_N	[49; 31]
Cr^{3+}	Decrease of the dielectric constant and the magnetization	[50]
Co^{3+}	Increase the T_N and the saturation magnetization	[51]
Mn^{3+}	Decrease in magnetization and T_N Occurrence of a structural defect and the dielectric constant at 250 K	[52; 53]
Ti^{4+}	Increasing the dielectric constant Decrease the saturation magnetization	[54]
Zn^{2+}	Increase of the magnetization by the passage of a ferrimagnetic behavior to a spin-decanted magnetism Increased polarization	[55]
Sc^{3+}	Decreased T_N Small decrease leakage currents Forming another structure following a high doping rate	[56]

In the case of the manganese doping for example [52; 53] a weakening of the magnetic properties has been noticed. This is probably due to the fact that the superexchange interactions Fe - O - Mn are lower than those of Fe - O -Fe. In the case of doping with magnesium (thin films) [49] a strong decrease of the leakage currents has been noticed. Asumption was made that the origin of the leakage currents is a sub-stoichiometry in oxygen in the cell being created during the deposition. This lack of oxygen anions leads to a partial reduction of Fe^{3+} to Fe^{2+} in order to respect the electroneutrality in the structure. The presence of the couple Fe^{3+}/Fe^{2+} reduces the electrical resistivity in the material *via* a hoping mechanism of an octahedral site by electrons one to another, generating a current which hinders the measurement of the ferroelectric effect. This mechanism was however only a conjecture and still remains to be proved. Doping GFO by voluminous Sc^{3+} ions [56] showed a slight decrease of the leakage currents. These ions distort anisotropically the cell and should induce an electric polarization through important cell distortion and cationic displacement. However, no polarization loop could be measured.

7. Conclusion

In this chapter was briefly described the $Ga_{2-x}Fe_xO_3$ compound since its discovery. The main properties of the material have been widely investigated, mostly in the form of bulk materials. Some zones of shadow still remain in this material and the control and tuning of the electric and magnetic properties of GFO should be looked for *via* :

- investigations of new GFO dopings. The conduction mechanisms in GFO thin films is still not fully understood. A way to decrease the leakage currents without decreasing the magnetic properties of the materials is still to be looked for. exploration of new ways of GFO syntheses. In particular, it would be interesting to investigate depositions of GFO by sputtering, since this method has never been mentionned before in the literature. The advantage of this technique is that it gives a possibility to apply an electric field during the deposition which might distort the cell and enhance the polarization.

Bibliography

[1] Remeika, J. P., Journal of Applied Physics 31 (1960) 263S.
[2] Abrahams, S. C., Reddy, J. M. and Bernstein, J. L., Journal of Chemical Physics 42 (1965) 3957.
[3] Krehula, S., Ristic, M., Kubuki, S., Iida, Y., Perovic, M., Fabian, M. and Music, S., Journal Of Alloys And Compounds 634 (2015) 130.
[4] Mukherjee, S., Garg, A. and Gupta, R., Journal of Physics-Condensed Matter 23 (2011) 445403.
[5] Arima, T., Higashiyama, D., Kaneko, Y., He, J. P., Goto, T., Miyasaka, S., Kimura, T., Oikawa, K., Kamiyama, T., Kumai, R. and Tokura, Y., Physical Review B 70 (2004) 064426.
[6] Kim, J. Y., Koo, T. Y. and Park, J. H., Physical Review Letters 96 (2006)
[7] Hatnean, M., Robert, J., Diaz, M. T. F., Ressouche, E., Cousson, A., Pinsard-Gaudart, L. and Petit, S., European Physical Journal-Special Topics 213 (2012) 69.
[8] Recko, K., Szymanski, K., Dobrzynski, L. and Waliszewski, J., Acta Physica Polonica A 122 (2012) 396.
[9] Szymanski, K., Dobrzynski, L., Bakr, M., Satula, D., Olszewski, W., Parzych, G. and Fuess, H., Phase Transitions 83 (2010) 824.
[10] Sharma, K., Reddy, V. R., Gupta, A., Kaushik, S. D. and Siruguri, V., Journal of Physics-Condensed Matter 24 (2012)
[11] Thomasson, A., Ibrahim, F., Lefevre, C., Autissier, E., Roulland, F., Meny, C., Leuvrey, C., Choi, S., Jo, W., Cregut, O., Versini, G., Barre, S., Alouani, M. and Viart, N., RSC Advances 3 (2013) 3124.
[12] Stoeffler, D., Journal of Physics-Condensed Matter 24 (2012) 185502.
[13] Remeika, J. and Marezio, M., Applied Physics Letters 8 (1966) 87.
[14] Ryding, S. H. M., Azough, F., Freer, R., Cernik, R. J., Tang, C. C. and Thompson, S. P., Journal of Applied Crystallography 45 (2012) 174.
[15] Rado, G. T., Physical Review Letters 13 (1964) 335.
[16] Lefevre, C., Roulland, F., Thomasson, A., Meny, C., Porcher, F., Andre, G. and Viart, N., Journal of Physical Chemistry C 117 (2013) 14832.
[17] Tronc, E., Chaneac, C. and Jolivet, J. P., Journal Of Solid State Chemistry 139 (1998) 93.
[18] Gich, M., Frontera, C., Roig, A., Molins, E., Fontcuberta, J., Bellido, N., Simon, C. and Fleta, C., arXiv preprint cond-mat/0509104 (2005)
[19] Mukherjee, S., Garg, A. and Gupta, R., Journal of Physics: Condensed Matter 23 (2011) 445403.
[20] Mohamed, M. B., Senyshyn, A., Ehrenberg, H. and Fuess, H., Journal Of Alloys And Compounds 492 (2010) L20.
[21] Sharma, K., Raghavendra Reddy, V., Kothari, D., Gupta, A., Banerjee, A. and Sathe, V. G., Journal of physics. Condensed matter : an Institute of Physics journal 22 (2010) 146005.
[22] Kundaliya, D. C., Ogale, S. B., Dhar, S., McDonald, K. F., Knoesel, E., Osedach, T., Lofland, S. E., Shinde, S. R. and Venkatesan, T., Journal of Magnetism and Magnetic Materials 299 (2006) 307.
[23] Roy, A., Prasad, R., Auluck, S. and Garg, A., Journal Of Applied Physics 111 (2012) 043915.
[24] Kalashnikova, A. M., Pisarev, R. V., Bezmaternykh, L. N., Temerov, V. L., Kirilyuk, A. and Rasing, T., Jetp Letters 81 (2005) 452.
[25] Sun, Z. H., Dai, S., Zhou, Y. L., Cao, L. Z. and Chen, Z. H., Thin Solid Films 516 (2008) 7433.

[26] Scott, J. F., Journal of Physics-Condensed Matter 20 (2008) 021001.
[27] Pintilie, L. and Alexe, M., Journal of Applied Physics 98 (2005) 124103.
[28] Trassin, M. (2009). Couches minces de $Ga_{2-x}Fe_xO_3$ par ablation laser pulsée : vers un matériau magnétoélectrique à température ambiante. Strasbourg, Université de Strasbourg.
[29] Trassin, M., Viart, N., Versini, G., Barre, S., Pourroy, G., Lee, J., Jo, W., Dumesnil, K., Dufour, C. and Robert, S., Journal of Materials Chemistry 19 (2009) 8876.
[30] Trassin, M., Viart, N., Versini, G., Loison, J. L., Vola, J. P., Schmerber, G., Cregut, O., Barre, S., Pourroy, G., Lee, J. H., Jo, W. and Meny, C., Applied Physics Letters 91 (2007) 2504.
[31] Thomasson, A., Cherifi, S., Lefevre, C., Roulland, F., Gautier, B., Albertini, D., Meny, C. and Viart, N., Journal of Applied Physics 113 (2013) 214101.
[32] Bertaut, E. F., Bassi, G., Buisson, G., Chappert, J., Delapalme, A., Pauthenet, R., Rebouillet, H. P. and Aleonard, R., Journal de Physique 27 (1966) 433.
[33] Levine, B. F., Nowlin, C. H. and Jones, R. V., Physical Review 174 (1968) 571.
[34] Srimathy, B., Bhaumik, I., Ganesamoorthy, S., Bhatt, R., Karnal, A. K. and Kumar, J., Journal Of Alloys And Compounds 590 (2014) 459.
[35] Lefèvre, C., Roulland, F., Thomasson, A., Mény, C., Porcher, F., André, G. and Viart, N., The Journal of Physical Chemistry C 117 (2013) 14832.
[36] Stoeffler, D., Thin Solid Films 533 (2013) 93.
[37] Nakamura, S., Morimoto, S., Saito, T. and Tsunoda, Y. (2009). Mössbauer Study on the Polar Ferrimagnet GaFeO(3). International Conference On Magnetism (Icm 2009). 200**:** 012140.
[38] Sharma, K., Reddy, V. R., Gupta, A., Banerjee, A. and Awasthi, A. M., Journal of Physics-Condensed Matter 25 (2013)
[39] Singh, V., Mukherjee, S., Mitra, C., Garg, A. and Gupta, R., Journal of Magnetism and Magnetic Materials 375 (2015) 49.
[40] Mukherjee, S., Garg, A. and Gupta, R., Applied Physics Letters 100 (2012) 112904.
[41] Gruener, G., Vitucci, F., Calvani, P. and Soret, J.-C., Physical Review B 84 (2011) 224427.
[42] Naik, V. and Mahendiran, R., Journal of Applied Physics 106 (2009) 3910.
[43] Roy, A., Prasad, R., Auluck, S. and Garg, A., Journal of Applied Physics 111 (2012) 043915
[44] Kundys, B., Roulland, F., Lefevre, C., Meny, C., Thomasson, A. and Viart, N., Journal of the European Ceramic Society 35 (2015) 2277.
[45] Kimura, T., Kawamoto, S., Yamada, I., Azuma, M., Takano, M. and Tokura, Y., Physical Review B 67 (2003) 180401.
[46] Brown, W. F., Hornreich, R. M. and Shtrikman, S., Physical Review 168 (1968) 574.
[47] Shireen, A., Saha, R., Mandal, P., Sundaresan, A. and Rao, C. N. R., Journal Of Materials Chemistry 21 (2011) 57.
[48] Hatnean, M. C., Pinsard-Gaudart, L., Fernández-Díaz, M. T., Petit, S., Dixit, A., Lawes, G. and Suryanarayanan, R., Journal of Solid State Chemistry 200 (2013) 110.
[49] Lefevre, C., Shin, R. H., Lee, J. H., Oh, S. H., Roulland, F., Thomasson, A., Autissier, E., Meny, C., Jo, W. and Viart, N., Applied Physics Letters 100 (2012) 262904.
[50] Mohamed, M. B., Wang, H. and Fuess, H., Journal Of Physics D-Applied Physics 43 (2010) 455409.
[51] Han, T., Lee, Y. and Chu, Y., Applied Physics Letters 105 (2014) 212407.
[52] Mohamed, M. B. and Fuess, H., Journal of Magnetism and Magnetic Materials 323 (2011) 2090.
[53] Mohamed, M. B., Hinterstein, M. and Fuess, H., Materials Letters 85 (2012) 102.

[54] Chakraborty, N. (2012). synthesis and characterization of pure and doped gallium ferrite, Jadavpur University Kolkata-700032 India.
[55] Mukhopadhyay, K., Mahapatra, A. S. and Chakrabarti, P. M., Physica B-Condensed Matter 448 (2014) 214.
[56] Thomasson, A. (2013). Ordres électriques et magnétiques dans le composé magnétoélectrique $GaFeO_3$: optimisation par dopage, Université de Strasbourg.

CHAPTER 3

Experimental

1. Elaboration of $Ga_{2-x}Fe_xO_3$ powders
2. Pulsed Laser Deposition
3. Sputtering
4. X-Ray Diffraction
   4.1 θ-2θ measurement
   4.2 Rocking-Curve (RC) measurement
   4.3 Reciprocal space mapping (rsm)
   4.3 φ-scan
5. Atomic Force Microscopy
6. Scanning Electron Microscopy
7. Transmission electron microscopy
8. SQUID magnetometry
9. Electric measurements
   9.1 Parallel
   9.2 Perpendicular
10. Determination of the samples composition
    10.1 Energy Dispersive X-Ray Spectroscopy
    10.2 ICP-AES Analysis
11. Resonant Elastic X-ray Scattering

    Bibliography

1. Elaboration of $Ga_{2-x}Fe_xO_3$ powders

$Ga_{2-x}Fe_xO_3$ (GFO) powders with x= 1.4 were prepared by ceramic solid state route using commercial powders of α-Fe_2O_3 (Prolabo> 99%) and β-Ga_2O_3 (Alfa Aesar 99.9%) and dopant if necessary. This kind of elaboration requires several distinct stages (Figure 3-1): mixing / milling, sample shaping and finally the heating step to obtain the desired phase.

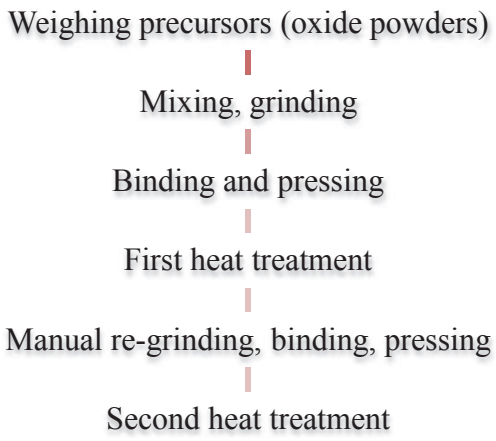

Figure 3-1. Scheme of the ceramic state route.

Mixing / grinding is performed by attrition Teflon jar using Zirconia balls (ZrO_2) of 1 mm diameter (Netzsch SAZ 1 / 1.2). Unlike a planetary mill, which acts by shocks and crushing of the powder particles, attrition operates by shearing of grains, which makes it possible to ultimately obtain lower particle size and improved monodispersity. These two properties will authorize a better reactivity during the calcination cycle and thus to facilitate obtaining a pure phase. Parameters such as the milling time and the dispersing medium were optimized by a study in particle size (Malvern Mastersizer 2000) coupled to observations by scanning electron microscopy and by zeta potential measurements (Malvern Zetasizer). The zeta potential (in mV) represents the electrical potential of each powder particle measured on the diffuse layer. These measurements require to work in dilute medium, and it is possible to approximate these results with actual mixing conditions [1]. It is recognized that the zeta potential should be the highest possible and the same sign for all components of the mixture, to minimize particle agglomeration during mixing / milling. The preparation of the pellets is done as described in [2]. The precursor powders are previously weighed in stoichiometric proportions and ground according to the conditions determined. The milling step is

systematically carried out in a solution with pH=9, for 60 minutes. After that the solution is put to the oven until the powders are dry. An organic binder (Rhodoviol, *i.e.* polyvinylic alcohol) is incorporated. Cylindrical pellets of 15 mm diameter and 2.5 mm thick were then pressed uniaxially at 1.5 T/cm^3 using a hydraulic press in case of the targets that are prepared for pulsed laser deposition. When the targets are prepared for sputtering, the pellets are pressed using 80 mm die. After well pressed pellets are obtained, they are put to the oven and heated up to 1450°C in air for 48 h and then cooled down to room temperature.

2. Pulsed Laser Deposition

Since 1987 when Dijkkamp *et al.* [3] published their ground breaking paper on $YBa_2Cu_3O_{7-x}$ (YBCO) prepared by pulsed laser deposition (PLD), there has been enormous interest and growth in the use of this unique physical vapour deposition (PVD) process for elaboration of all kinds of complex compounds such as oxides, nitrides, etc... In PLD a target holder and a substrate holder are housed in a vacuum chamber. A high-power laser is used as an external energy source to vaporize materials from the target and grow thin films onto the substrate. A set of optical components is used to focus and raster the laser beam over the target. So as to facilitate the homogeneous evaporation of the target, this latter is scanned by the laser throughout a defined area. The substrate is mounted on a heating device and located in the way of the target at a fixed distance of 4 to 6 cm. This technique makes possible the stoichiometric transfer of the material and allows depositions in an oxidizing atmosphere (Figure 3-2).

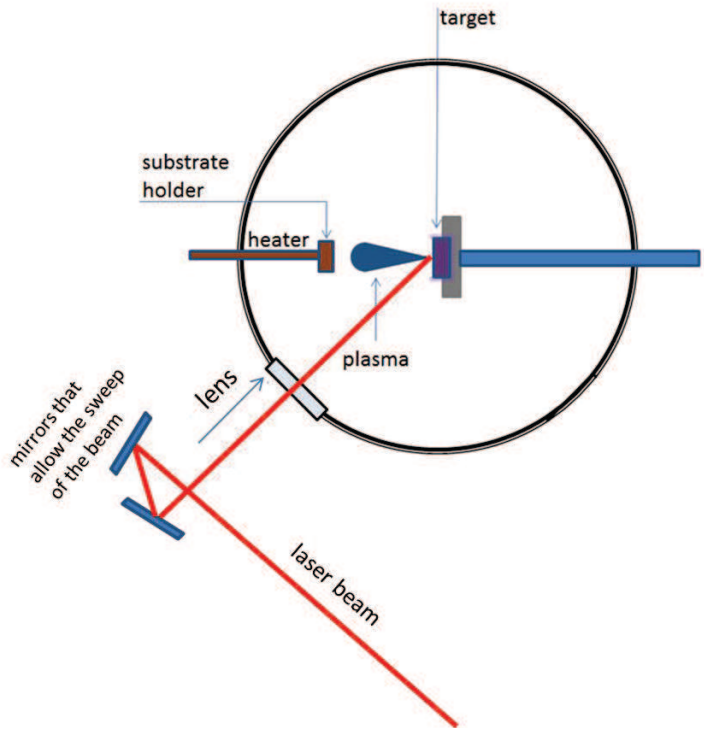

(a)

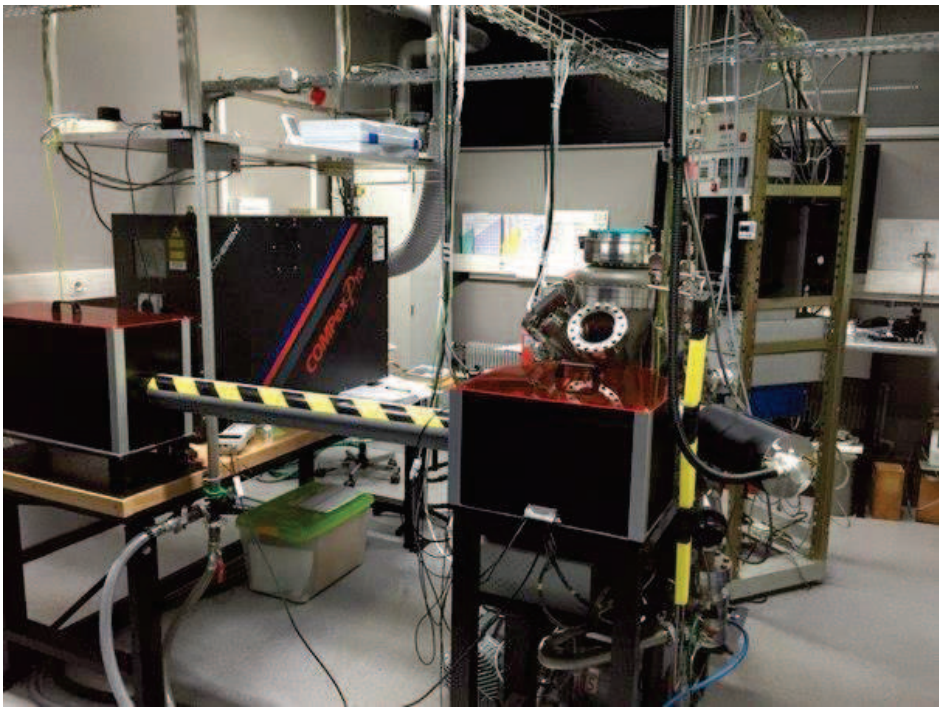

(b)

Figure 3-2. A Pulsed Laser deposition set up: (a) scheme, (b) real image of the IPCMS set-up.

Pulsed laser deposition for thin film growth has several advantages:

-Large pressure range to deposit materials: from $<10^{-7}$ mbar (high vacuum without additional background gas) up to 1 mbar.

-The laser is not part of the vacuum system. Therefore a considerable degree of freedom in the ablation geometry is possible.

-The congruent transfer of the composition can be achieved for many ablated material or materials combinations.

-Moderation of the kinetic energy of evaporated species to control the growth properties and growth modes of a film. In addition, a background gas can provide an appropriate reactive atmosphere using *e.g.* oxygen to create oxidized species in the plasma, when growing oxide films.

The drawback of the PLD technique is that the large kinetic energy of some plume species causes re-sputtering and likewise defects in the substrate surface and growing film. Due to the high laser energies involved, macroscopic and microscopic particles can be ejected from the target which can be detrimental to the desired properties of films and multilayers. When the time required to transfer laser energy into heat is shorter than needed to evaporate a surface layer with a thickness on the order of depth, the subsurface layer is superheated before the surface itself has reached the vapor phase- this can cause so-called 'splashing' phenomenon.

The deposition mechanism is strongly dependent on the energy of the laser used and the area of the illuminated target. The fluence of the laser beam corresponds to the laser energy per unit area. The evaporated particles interact with the laser beam, which induces the isothermal expansion of the plasma which then contains all the elements of the target in ionic, atomic, or molecular form . The size of the plasma plume depends on several parameters, such as the laser energy (LE), the target to substrate distance (TSD), the focalization (F) and the repetition rate (RR). On Figure 3-3 the comparison of the plasma plume is pictured when changing energy with fixed TSD (45mm), RR (10Hz) and F (2 mm^2).

90 mJ	50 mJ	25 mJ

Figure 3-3. Plume with different laser energies with fixed TSD (45mm), F(2mm^2) and RR(10Hz).

Deposition Conditions of GFO thin films

The deposition of the samples was done in O_2:N_2 gas (20%: 80%). A flowmeter with an accuracy ranging to 30 sccm was used to control the pressure of the reactive gas in the chamber for any type of gas down to $1x10^{-6}$ mbar. GFO films depositions was optimized in a previous work [4] and requires to work under 1 mbar O_2:N_2. This high deposition pressure reduces the deposition rate. In this deposition pressure, 150 000 laser pulses allows obtaining a 100 nm thick layer.

The substrate is placed on a holder of stainless steel, itself fixed on a heating substrate holder to achieve a maximum temperature of 820 °C. The temperature strongly affects the crystallization of the films. High temperature brings enough energy to move the atoms on the substrate and thus optimize the quality of crystallization. The rise in temperature is done according to a ramp of 10 °C / min, it is the same for descent in temperature. To meet the needs of this work, when Pt electrode as a bottom was required, some depositions were done partially under a temperature gradient of 600 °C to 820 °C [5]. The presence of a carousel rotating target holder gives a possibility for placing up to 6 targets.

3. Sputtering

Sputtering is based on the theory that particle to particle collisions will involve an elastic transfer of momentum, which can be utilized to deposit a thin film onto the substrate. In this technique, ions are accelerated toward a target by utilizing electric fields. These ions are usually derived from either an ion gun or from exciting a neutral gas into ion plasma. As the ions are accelerated and bombard the target surface, they dislodge target atoms and other ions. The ejected atoms attach themselves to the substrate, and a thin film of the target material is produced (Figure 3-4)

(a)

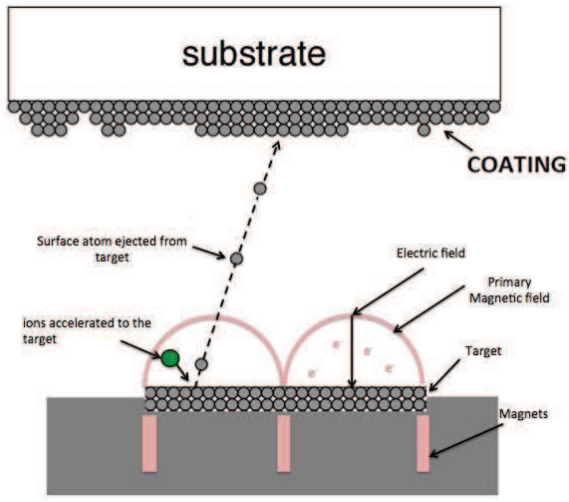

(b)

(c)

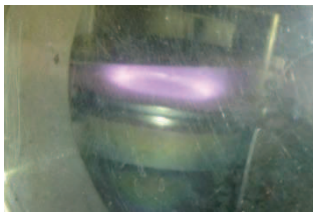

Figure 3-4. The sputtering equipment: (a) scheme of deposition; (b) a real image of set up in IPCMS; (c) the plasma during the deposition.

GFO thin films were obtained by radio frequency (RF) sputtering technique from a GFO target 75 mm diameter. The target to substrate distance was about 25cm. The temperature of substrates was maintained at 700 °C during the deposition. The base pressure was of 1.6×10^{-8} mbar, but for for the preparation of the thin films, various mixtures of ($Ar+O_2$) gases were. We always used the same RF power conditions (40W). In these conditions, the deposition rate was 0.06 Å/s. Some depositions were performed in an electric field, with an additional positive voltage applied to the substrate holder.

4. X-Ray diffraction

The X-ray diffraction gives a possibility to study the crystallographic structure of the sample.

4.1 *θ-2θ* measurement

The most common configuration is the *θ-2θ* measurement, also called symmetric mode (Figure 3-5). 2*θ* is the angle between the incident and diffracted beams. It relates to the interplanar distance of crystal planes. In the θ-2θ configuration, the angle between the sample surface and the incident beam is equal to the angle between the diffracted beam and the sample surface. The obtained diffractogram provides information on planes parallel to the surface, the diffraction vector being perpendicular to the sample surface. The measurement therefore provides information on the growth direction and the out of plane lattice parameter.

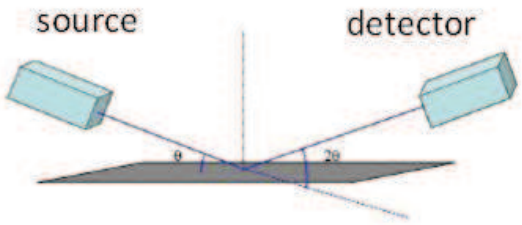

Figure3-5. Scheme of *θ-2θ* configuration.

4.2 Rocking-Curve (RC) measurement

Rocking curves (RC), also known as *ω* scans, (Figure 3-6) allow evaluating the orientation of the crystalline phase in a thin film. *ω* is the angle between the incident beam and the surface of the sample.The incident and diffracted angles are decoupled. A chosen *2θ* angle is kept fixed while scanning a range of *ω* angles. The width of the peak obtained gives information on the disorientation degree of the planes.

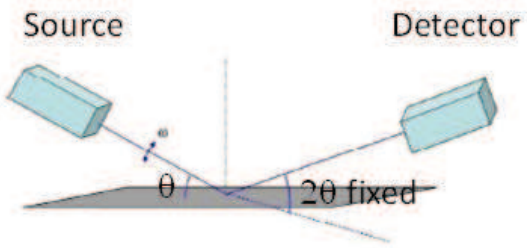

Figure 3-6. Scheme of the rocking curve configuration.

4.3 Reciprocal space mapping (rsm)

The *θ-2θ* configuration gives us information about the out of plane lattice parameters. To obtain information on the plane parameter of the layer, it is necessary to scan the reciprocal space (Figure3-7) and reach reflections that contain information about the order in the plane.

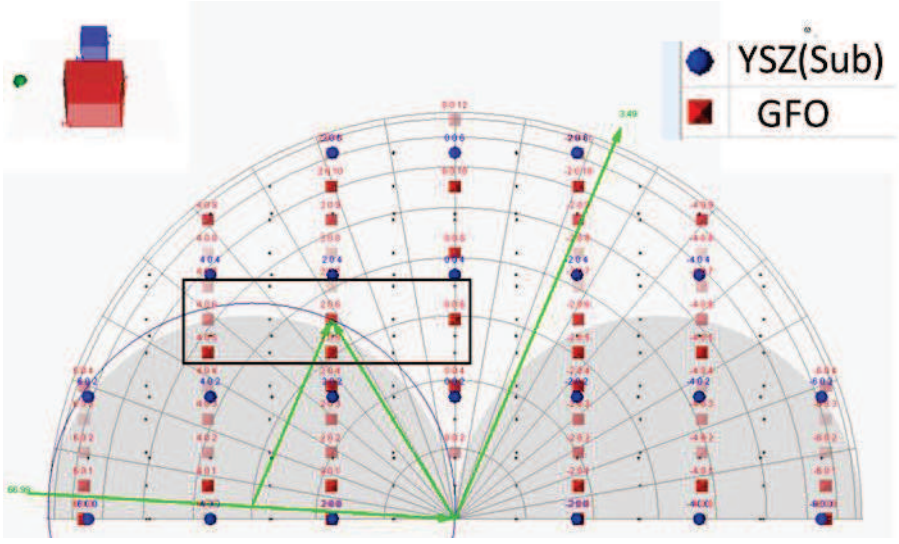

Figure 3-7. Reciprocal space for the stack GFO(0*k*0)/YSZ (100), as proposed by the SmartLab Guidance software (Rigaku).

Reciprocal space mapping consists in making a series of ω-2θ scans for different ψ angles in the vicinity of the theoretical position of the reflection. Achieving these maps provides access to components perpendicular to the plane of the diffraction $Q_{\perp}$ and in the plane of the diffraction $Q_{//}$ according to:

$$(1) \qquad Q^{//} = \frac{4\pi}{\lambda} \sin\theta \sin\psi \qquad\qquad Q^{\perp} = \frac{4\pi}{\lambda} \sin\theta \cos\psi$$

Each of these components and $Q_{\perp}$ and $Q_{//}$ is inversely proportional to the cell parameters in and out of plane, respectively.

All the measurements were performed using a Rigaku Smartlab diffractometer equipped with a rotating anode (45 kV, 200 mA) of copper radiation (Kα = 0.154056 nm).

4.3 φ-scan

A φ-scan, which consists in monitoring the intensity corresponding to a particular reflection for ω / 2θ couple with a rotation around the normal to the sample plane (Figure 3-8). This mode is used to look for specific nodes of the network.

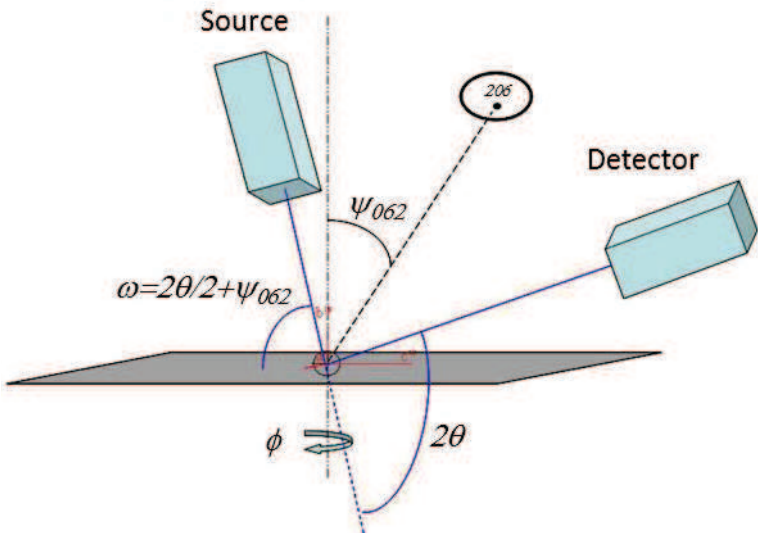

Figure 3-8. Scheme of the measurement of φ-scan in the case of reflection (062) of the GFO.

5. Atomic Force Microscopy (AFM)

The study by atomic force microscopy involves scanning the sample surface with a tip of small size, ideally consisting of a single atom at its apex and measuring the interaction between this tip and the surface. The tip is locat ed at one end of a cantilever. This tube allows lateral and vertical displacement of the cantilever, essential to the approach of the tip to the surface and to obtain a good spatial resolution of the measurements. When the tip approaches the surface, the interaction between the survey surface and the tip causes a change in the position of the cantilever. This change is detected as a move of the laser beam reflected on the cantilever, by photodiodes. There are two measurement modes. In the mode known as "contact", the tip is in contact with the surface, a feedback loop is used to measure and change the elevation of the point by the action of a piezotube to ensure permanent contact with the surface. This mode is reserved to the study of very flat surfaces, so not to risk damaging the tip. The second mode is called "tapping". The tip is not in direct contact, but just a few angstroms above the surface. The cantilever is vibrated at its natural resonant frequency and the interaction with the surface changes the frequency of this oscillation. A measurement comprises scanning areas of a few square microns in surface area in order to determine the roughness. The apparatus used is a microscope Nanoscope III Digital Instrument and the measurements were carried in tapping mode with silicon cantilevers of nanosensors at a resonance frequency of 300 kHz.

6. Scanning electron microscopy

An electron beam scans the sample surface. The interaction of the beam with the material gives rise to phenomena of diffusion, emission of secondary electrons, Auger electrons, backscattered electrons and X-rays. With the Secondary Electron Image imaging mode (SEM), the detector is sensitive to secondary electrons with low energy which originate from only a very small thickness (a few nanometers). This imaging mode is sensitive to the sample surface morphology and provides a good definition of the contours of the surface. The Lower Electron Image mode (LEI) detects the secondary backscattered electrons in proportion dependent on the acceleration voltage. At high voltage, the yield of secondary electrons is low, unlike that of the backscattered electrons. This imaging mode is also used to visualize the sample surface. Finally for the Composition Mode (COMPO), the detector is sensitive to

backscattered electrons only. A contrast is obtained according to the atomic number of the elements present. The light elements induce dark regions and heavy elements clearer areas. An acquisition coupled with LEI mode allows to discriminate the contrast due to the roughness from that due to possible variations of composition or the presence of impurities. A JEOL 6700F was used for the study of different morphology of thin films. The microscope is also equipped with an Energy Dispersive X-ray Spectroscopy detector, allowing the determination of the composition of the materials observed.

7. Transmission electron microscopy

Transmission electron microscopy can image the structural arrangement of compounds at the Angstrom scale. It may be used to determine the thickness of thin films (observation of cross views), crystal growth and the quality of the interfaces. The visualization in transmission requires a very small thickness of the sample (less than fifty nanometers). This technique therefore requires a critical thinning of the sample preparation step, describes in details further.

The samples were observed using the microscope JEOL 2100FCs. This microscope is equipped with the scan function Scanning Transmission Electron Microscopy (STEM), an Electron Energy Loss Spectroscopy detector (EELS) and an Energy Dispersive X-ray Spectroscopy detector (EDX). This microscope allowed us to determine local chemical profiles of the species.

The sample preparation was done in 2 ways:

-Manual polishing

The preparation is carried in transverse mode when it is desired to observe the stack in cross view or in plane mode when it is desired to obtain a plane view of the thin layer. For a plane view, the sample preparation (Figure 3-9), of dimension less than 3 mm², begins with successive mechanical polishing using disks (formed of a polymer matrix to which integrates SiC grains) of decreasing grain density in order to reduce the thickness of the substrate.

For a preparation in cross section, a 5 x 3mm² sample is cut in two portions. These portions are then glued face to face with an epoxy adhesive Gatan G1 (heat treatment 200 ° C for 2 hours to polymerize the glue). Glueing the surfaces *vis-à-vis* doubles the observable area but also protect this area during the mechanical polishing step. Polishing is done for both sides. Polishing is a critical step. The polished surfaces should contain as few defects as

possible to avoid cleavage during thinning. For all preparations, polishing was performed using the Allied Multiprep System device.

Once the mechanical polishing performed (thickness of about 20-30 microns), there are two options for the further thinning: ion milling, or finalization of the polishing manually. Regarding this point, it should be noted that very few studies are beginning to be published giving some hints of disparities between the two methods.

In the first case, the samples are bonded to a copper ring, which gives a possibility of fixing the sample. The samples are then thinned by the ion milling PIPS (Precision Ion Polishing System-Gatan). Two Ar+ ion guns bombard the substrate surface with an accelerating voltage of 4 kV. The rotation of the sample enables a homogeneous attack. A lower energy bombardment (1-2kV) is performed towards the end of the thinning, until a hole is done, to minimize the amorphization of the sample surface. The study area for the transmission electron microscopy is limited to the vicinity of the hole obtained by the bombardment. The angle of incidence of the guns is reduced to increase the size of observable regions (6 ° for the view plane and 8 ° for the cross view).

The evolution of polishing is monitored using an optical microscope. Upon the occurrence of interference fringes, significant of a very small thickness, it is considered that the sample is sufficiently thin to observation by transmission electron.

Figure 3-9 (a). Sample preparation for TEM observation in plane view. The last step is the ion milling.

Figure 3-9 (b). Preparation of a sample for TEM cross section observation , with the ion milling a the last step.

-Focused ion beam (FIB)

A FIB instrument operates much like a scanning electron microscope (SEM). Both instruments rely on a focused beam to create a specimen image; an ion beam for the FIB and an electron beam for the SEM. For both instruments, the intensity of the secondary electrons produced at each raster position of the beam is displayed to create an image of the sample. In the FIB, secondary ions may also be detected and used to construct an image of the sample. Images having magnifications up to 100 000 times are available using a FIB with a very good depth of field. The operation of a FIB begins with a liquid metal ion source (LMIS). A reservoir of gallium (Ga) is positioned in contact with a sharp Tungsten (W) needle. The Ga wets the needle and flows to the W tip. A high extraction field (108 V/cm) is used to pull the liquid Ga into a sharp cone whose radius may be 5–10 nm. Ions are emitted as a result of field ionization and post-ionization and then accelerated down the FIB column. The use of Ga is advantageous for two reasons: (i)Ga has a low melting point and, therefore, exists in the liquid state near room temperature, and (ii) Ga can be focused to a very fine probe size (10 nm in diameter). FIBs typically operate with an accelerating voltage between 5 and 50 keV. By controlling the strength of the electrostatic lenses and adjusting the effective aperture sizes, the probe current density (and therefore beam diameter) may be altered from tens of pA to several nA corresponding to a beam diameter of 5nm to 0.5mm). When a Ga ion is accelerated toward the target sample, it enters the sample and creates a cascade of events which results in the ejection of a sputtered particle (which may be an ion or a neutral atom). The primary ion penetration depth is 20 nm for 25 keV Ga. The FIB preparation of the samples was performed at the Service of Microscopy of the IEMN Institute in Lille, France.

8. SQUID magnetometry

The magnetic characterization of the thin films were conducted by a MPMS SQUID magnetometer VSM (Quantum Design). The SQUID detector (Superconducting Quantum Interference Device) consists of a superconducting ring segmented by one or two isolation regions of very small thickness constituting the Josephson junctions. The insertion of these insulating regions in a magnetic field results in the passage of a tunnel current of charge carriers predicted by Josephson. The amplitude of this current is function of the magnetic flux. Measuring the current through the junction can be traced back to the magnetic field flow.

This type of magnetic field detection is the most sensitive that exists with an accuracy of 10^{-8} emu. The VSM (Vibrating Sample Magnetometer) used, wherein the sample oscillates rapidly in the superconducting ring, allows a characterization of samples on a wide range of temperatures (1.8 K to 400 K) and for fields of up 7 T. This configuration allows an acquisition faster than conventional SQUID measurements. The axis of easy magnetization of $GaFeO_3$ compound is located along the crystallographic *c* axis. In the case of magnetic measurements of thin layers, the "parallel" measurements correspond to a magnetic field applied in the plane of the sample (containing the easy magnetization axis - the orientation of the sample in plane is irrelevant, because of the presence of the equivalents variants.), and the "perpendicular" measurements correspond to a magnetic field applied out of plane.

When measuring magnetization curves M = f (H), a diamagnetic contribution is noticed, originating from the straw in which the samples are placed, as well as from the substrate onto which the film is grown. Thus, it is necessary to withdraw this contribution in order to obtain the one which originates from the intrinsic material. The measurements performed on the various GFO thin films at 300 K showed saturation. It was thus easy to determine the diamagnetic contribution from these measurements. It was more difficult to say if the measurements performed at 5 K showed any saturation. Since the diamagnetic contribution is temperature independent, we corrected those measurements from diamagnetism by subtracting the slope attributed to diamagnetism on the 300 K measurements.

9. Electric measurements

9.1 Perpendicular:ferroelectric dynamic characterizations

Ferroelectric measurements were performed by Salia Cherifi and Romain Jarrier (IPCMS) using an analyzer TF 2000 (AixCCT) after depositing an upper electrode deposited by e-beam evaporation. These electrodes are of square shape, with dimensions of *ca.* 30 x 30 µm². The dynamic hysteresis measurements are acquired as follows: a delta voltage is applied to the sample at different frequencies (up to 3 kHz). A pre-polarization allows to fix the polarization in a given state (*e.g.* the negative residual polarization, denoted by 1). Then three bipolar excitation signals are applied, each separated by one second relaxation.

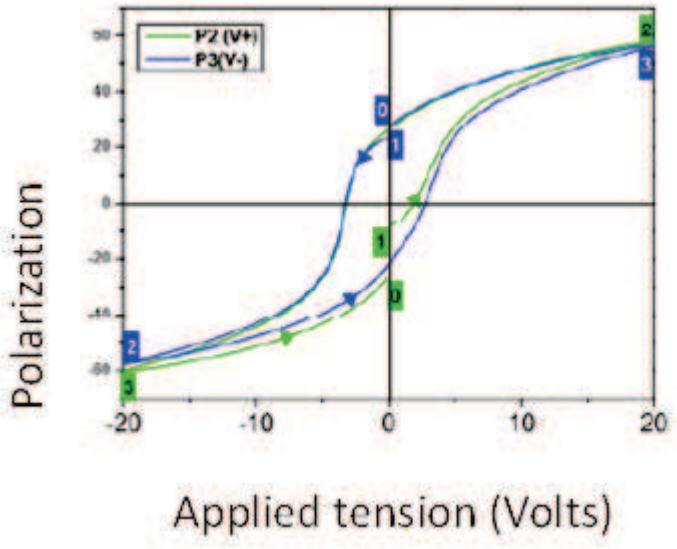

Figure 3-10. Ferroelectric dynamic measurements.

The first signal will establish a positive polarization in saturated state (2). The second will allow obtaining the negative saturation (3), and the third will bring the system into a state of negative residual polarization (0). Again this step is then carried out (blue curve), starting from the positive retention (1) to go into the negative saturation state (2), and a voltage is applied until the positive saturation (3) . Finally, it returns to the state of positive afterglow (0). The final hysteresis is then deduced from the second portion of the first excitation (between 2 and 3), and the second part of the second excitation (between 2 and 3).

9.2 Parallel electric measurements

These measurements were performed by Ekaterina Chikoidze, Yves Dumont and Yue Chang at the GEMaC-CNRS, Versailles. Resistivity and Hall effect measurements were performed on the films by Van der Pauw method on a home built set-up, operating in the temperature range 80 K – 880 K, using Ti/Au sputtered electrodes for ohmic contact. Seebeck effect measurements were carried out at 300 and 500 K, in order to confirm the nature of the carrier types.

10. Determination of the compositions

10.1 Energy-dispersive x-ray spectroscopy

Both the scanning and transmission electron microscopes that we used are equipped with an EDX elemental analysis system (Energy Dispersive X-ray Spectroscopy). This device provides access to the nature of the elements that are present and the composition of thin films. The EDX analysis is based on the interaction between the sample and the electron beam. The electrons located on the outermost layers of these then occupy lower energy levels. The transition from a high energy level to a lower energy level generates X-rays characteristic of the element, and allows evaluating its concentration in the observed sample. The analyzed volume depends upon the size of the electron beam. It is of about 1 μm^3 for analyses perfomed with the SEM. The survey depth is adjustable according to the energy of the incident beam.

10.2 ICP-AES Analysis

The composition of the films was analysed by Inductively Coupled Plasma Atomic Emission Spectroscopy, performed at the “Plateforme Analytique Inorganiques”, Strasbourg) after microwave assisted dissolution of approximately 3 x 3 mm^2 samples in HNO_3 for trace analysis (TraceSE-LECT®, Fluka). The AES method uses the fact that the atoms excited by ionization emit a photon whose energy is characteristic of the element when they return to the ground state . The plasma torch consists of three concentric quartz tubes around which is placed a RF coil. An argon gas is introduced into the chamber and ionized in a strong magnetic field. The total light emitted by the plasma is analyzed through a monochromator. Those issued by the desired elements are then detected and measured, and their intensities compared to those issued by the same element present in a known concentration of standard solution, analyzed under identical conditions. This method is precise but destructive, since the layers must be dissolved in an acidic solution prior to analysis.

11. Resonant Elastic X-ray Scattering

The actual insertion of Ni in the GFO cell was checked by X-ray resonant diffraction [6]. The intensity of three independent Bragg reflections of the GFO $P\mathrm{c}2_1\mathrm{n}$ structure were recorded as a function of the energy of the scattered photons crossing the atomic Ni K edge (8.33 keV). The X-ray resonant diffraction experiments were performed on the CRG-BM02 beamline, in collaboration with Vincent Favre-Nicolin and Nathalie Boudet, at the European Synchrotron Radiation Facilities (ESRF) in Grenoble using photon energies between 8.285 and 8.405 keV. The measured intensities were corrected from fluorescence.

Bibliography

[1] Hunter, R. J. (1981). Zeta potential in colloid science : principles and applications. London; New York, Academic Press.
[2] Roulland, F., Lefèvre, C., Thomasson, A. and Viart, N., Journal of the European Ceramic Society 33 (2013) 1029.
[3] Dijkkamp, D., Venkatesan, T., Wu, X. D., Shaheen, S. A., Jisrawi, N., Minlee, Y. H., McLean, W. L. and Croft, M., Applied Physics Letters 51 (1987) 619.
[4] Trassin, M. (2009). Couches minces de $Ga_{2-x}Fe_xO_3$ par ablation laser pulsée : vers un matériau magnétoélectrique à température ambiante. Strasbourg, Université de Strasbourg.
[5] Trassin, M., Viart, N., Ulhaq-Bouillet, C., Versini, G., Barre, S., Leuvrey, C. and Pourroy, G., Journal of Applied Physics 105 (2009) 6101.
[6] Hodeau, J.-L., Favre-Nicolin, V., Bos, S., Renevier, H., Lorenzo, E. and Berar, J.-F., Chemical Reviews 101 (2001) 1843.

CHAPTER 4

Ni doped $Ga_{2-x}Fe_xO_3$ thin films

1. Motivation of doping GFO with Nickel
2. Ni doped GFO in the bulk form
   - 2.1 Elaboration
   - 2.2 Structural analysis
   - 2.3 Compositional analysis
3. Ni doped GFO thin films
   - 3.1 Ni doped GFO thin films on Pt buffered YSZ(111)
     - 3.1.1 Surface analysis
     - 3.1.2 Structural analysis
     - 3.1.3 Electric properties
   - 3.2 Ni doped GFO thin films deposited on STO:Nb(111)
     - 3.2.1 Structural analysis
     - 3.2.2 Magnetic properties
   - 3.3 Ni doped GFO thin films deposited on YSZ(100)
     - 3.3.1 Structural analysis
     - 3.3.2 Magnetic properties
     - 3.3.3 Electric properties
4. Conclusion

Bibliography

1. Motivation of doping GFO with Nickel

The high level of leakage currents commonly observed in thin films of oxides is usually attributed to the presence of oxygen vacancies. Such a lack of oxygen would lead for GFO to a partial reduction of Fe^{3+} into Fe^{2+}.

The presence of the couple $Fe^{2+}/Fe^{3+}$is decreasing the electrical resistivity of the layers due to a hopping mechanism of electrons from one cation to another. Such behaviors could be observed in other oxide systems like $BiFeO_3$, $YnMnO_3$, $Ni_3V_2O_8$ [1; 2]. This conduction mechanism plays a key role in the measurement of polarization when the electric field is applied to obtain P-E curves (measuring the change in polarization as a function of electric field).

The problem of leakage currents is usually solved in the literature through doping. Numerous studies have been performed on the investigation of GFO (bulk and thin films) doped with Mn [3; 4], Cr [5], Mg [6; 7], Al [8] and Sc [9].

Our team has previously studied the possibility to decrease the leakage currents in GFO doping with Mg. The optimal amount of substitution was found to be 2% [7]. The substitution showed no significant change in the GFO structure. Unfortunately, Mg substitution doesn't only allow the reduction of leakage currents. It also induces a slight decrease of the magnetic properties of the films.

This chapter will report on a study we performed on doping $Ga_{0.6}Fe_{1.4}O_3$ (GFO 1.4) with Ni. Ni is bivalent, as Mg, but has a magnetic moment and should therefore not negatively influence on the magnetic properties of the material. The aim of this study is to fully understand the mechanism responsible for conduction in GFO thin films and control it. The GFO1.4 composition was chosen for it has the best magnetic characteristics: highest Neel temperature and saturation magnetization.

2. Ni doped GFO in the bulk form

2.1 Elaboration

The elaboration of Ni doped GFO in a bulk form is necessary for elaboration of targets for PLD. The preparation process is described in Chapter 3, where the amount of Ni that must be added in the compound was calculated by:

$$(1)\quad \frac{0.6}{2}\,Ga_2O_3 + \frac{1.4-y}{2}\,Fe_2O_3 + y\,NiO \rightarrow Ga_{0.6}Fe_{1.4-y}Ni_yO_{3-y/2}$$

Six different targets of Ni doped GFO1.4 - $Ga_{0.6}Fe_{1.4-y}Ni_yO_{3-y/2}$ with different substitution percentages were prepared : 0.1%, 0.5%, 1%, 2%, 3% and 5%. These global percentages are calculated as y/(0.6+1.4-y+y).

2.2 Structural analysis

X-ray diffractograms obtained for calcinated targets are shown on Figure 4-1.

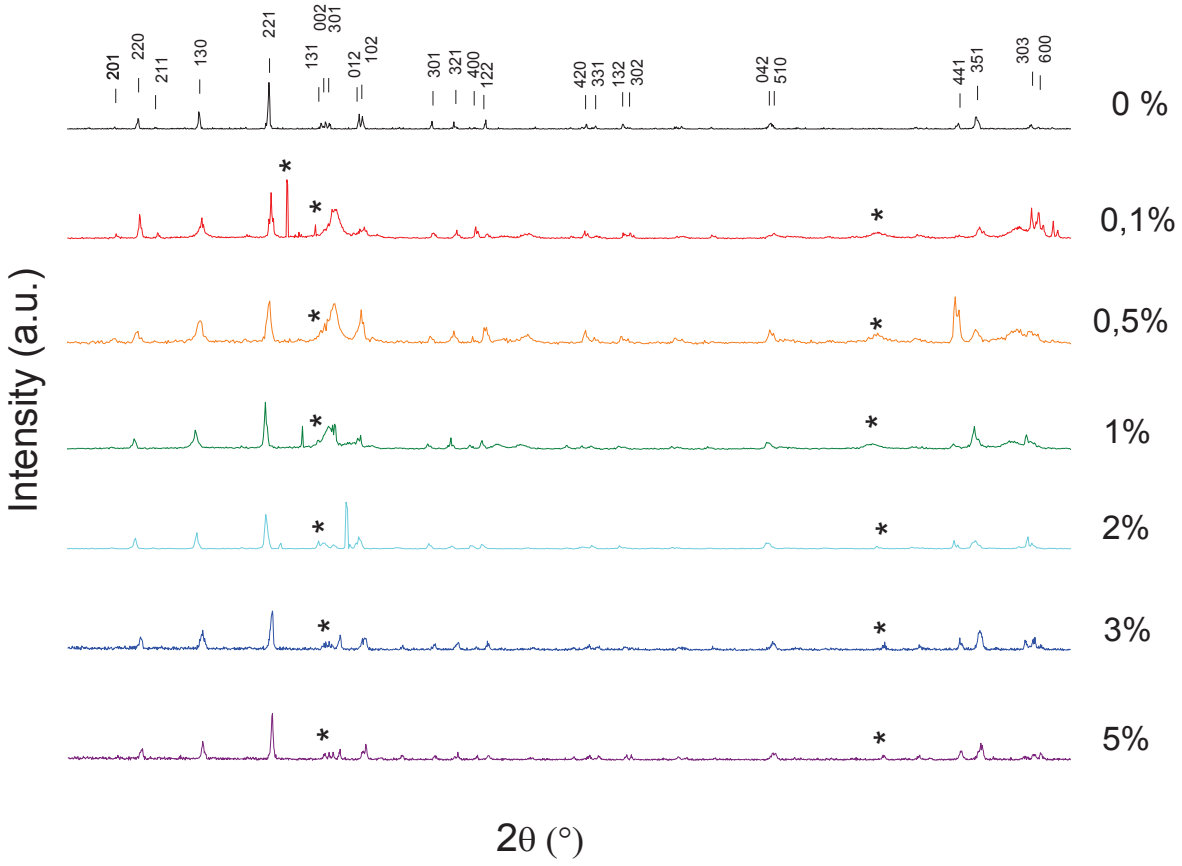

Figure 4-1. X-ray diffractograms of different GFO :Ni ceramics for 0.1%-5% concentrations. The star * indicates a position of the parasitic phase matching with ICDD No.01-072-9576

Intense and well defined peaks observed on the diffractograms of the powders show the presence of an orthorhombic phase of GFO matching ICDD 01-076-1005 file for all the studied compositions. Additional peaks were also observed indicating the presence of secondary phase. The extra peaks correspond to a spinel structure, which can be either $NiFe_2O_4$ (ICDD No.00-010-0325), $GaFe_2O_4$ (ICDD No. 01-072-9576), or any other spinel of intermediate composition. The expected change in the lattice parameters of the GFO phase influenced by Ni insertion could not be followed by structural refinements due to the presence of a parasitic phase.

2.3 Compositional analysis

The global composition of the powders was evaluated with scanning electron microscopy coupled with energy dispersive x-ray spectroscopy (SEM coupled with EDX) on zone of a few $100\mu m^3$ (*Table 4-1*).

Table 4-1 Compositions of GFO:Ni doped pellets.

	Expected composition	Experimental composition	Error
GFO non doped	$Ga_{0,6}Fe_{1,4}O_3$	$Ga_{0,52}Fe_{1,48}O_3$	±0,03
GFO 0.1% Ni	$Ga_{0,6}Fe_{1,39}Ni_{0,002}O_3$	$Ga_{0,58}Fe_{1,41}Ni_{0,001}O_3$	±0,02
GFO 0.5% Ni	$Ga_{0,6}Fe_{1,39}Ni_{0,01}O_3$	$Ga_{0,59}Fe_{1,39}Ni_{0,01}O_3$	±0,01
GFO 1% Ni	$Ga_{0,6}Fe_{1,38}Ni_{0,02}O_3$	$Ga_{0,57}Fe_{1,41}Ni_{0,01}O_3$	±0,02
GFO 2% Ni	$Ga_{0,6}Fe_{1,36}Ni_{0,04}O_3$	$Ga_{0,59}Fe_{1,39}Ni_{0,02}O_3$	±0,02
GFO 3% Ni	$Ga_{0,6}Fe_{1,34}Ni_{0,06}O_3$	$Ga_{0,59}Fe_{1,36}Ni_{0,05}O_3$	±0,02
GFO 5% Ni	$Ga_{0,6}Fe_{1,3}Ni_{0,1}O_3$	$Ga_{0,610}Fe_{1,33}Ni_{0,06}O_3$	±0,02

The global experimental compositions match with the expected ones when considering the error bar.

Images of the surface of the pellets were made by SEM. Figure 4-2 shows the surface of the pellet of GFO:Ni for 0.5% substitution, which is representative of the different observed ceramics.

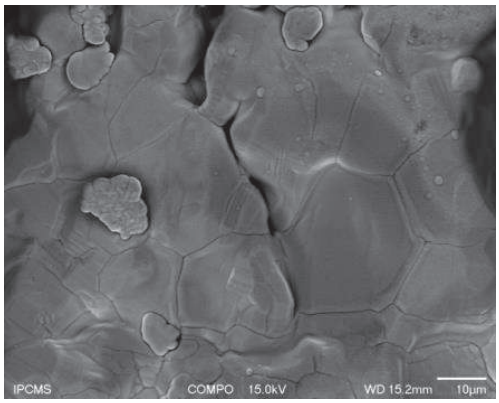

Figure 4-2. SEM image of the surface of the GFO:Ni 0.5% pellet.

The grain size, often elongated, is of the order of twenty micrometers and doesn't appear to change significantly as a function of doping level. The relatively long heat treatment at very high temperature may help to explain the large size of the ceramic grains. Point EDX analysis showed some places richer in Fe, which could be correlated with the presence of parasitic phases which are identified on XRD. Compositional inhomogeneity is at $100\mu m^3$.

The attempts to insert Ni into GFO do not allow obtaining pure GFO phase. Ni drives the structure towards a spinel-like phase. Since the EDX analyses showed rather small inhomogeneity of the composition, it was possible to use the Ni doped targets for PLD in order to do depositions of thin films.

3. Ni doped GFO thin films

3.1 Thin films of Ni doped GFO on Pt buffered YSZ(111)

3.1.1 Surface analysis

In order to be able to perform perpendicular electrical measurements, thin films of doped GFO:Ni were deposited on high quality conducting Pt buffered YSZ(111). The conditions of Pt deposition are described elsewhere [10].

The observations by SEM showed no significant decrease in surface quality with Ni insertion (Figure 4-3).

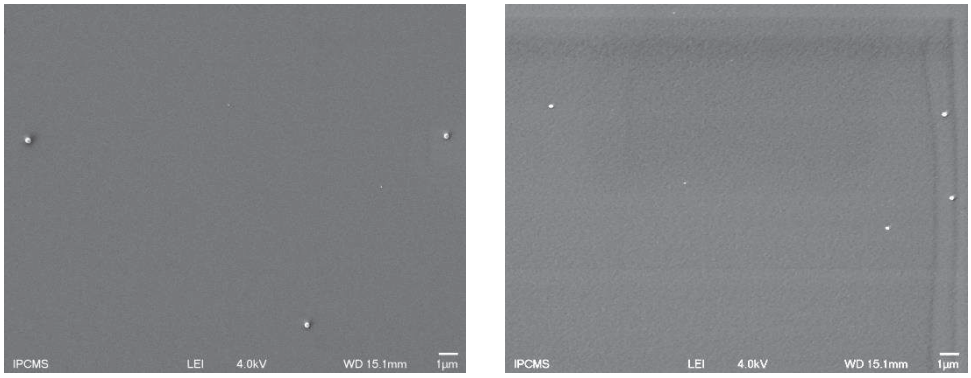

a) b)

Figure 4-3. SEM images of (a) the non-doped and (b) GFO:Ni 1% doped thin films, deposited on Pt//YSZ(111).

The surface analysis of the layers didn't show any major defects, except splashings, which are common in PLD. The size of the splashings is less than 100 nm which proves a good quality of the surface. The estimated roughness with reflectivity of undoped and doped layers was 0.6 nm and 1 nm, respectively.

3.1.2 Structural analysis

Figure 4-4 shows the diffractograms of GFO:Ni films for doping between 0 and 5%.

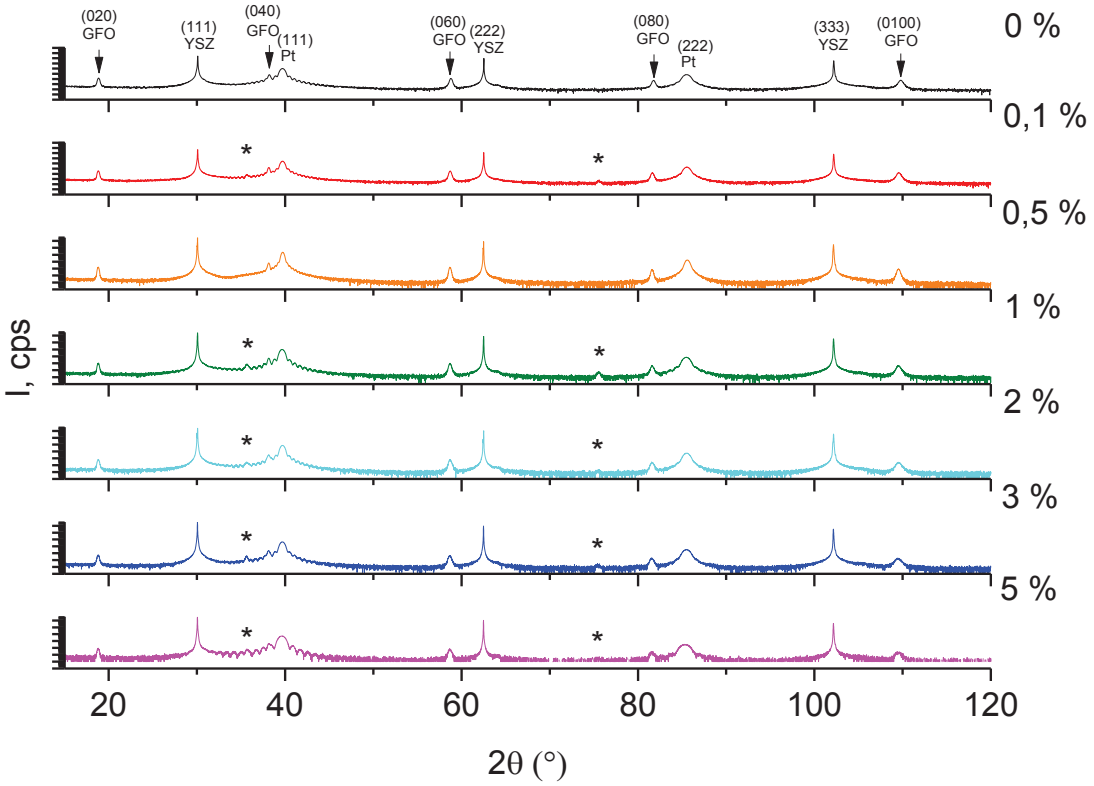

Figure 4-4. Diffractograms of GFO: Ni thin films deposited on Pt//YSZ(111). A parasitic phase, marked by *, corresponds to a possible spinel phase.

The Figure 4-4 shows the existence of an additional phase (marked as * on the diffractogram) of a spinel structure. The two peaks could correspond to the (311) and (622) reflections of ICDD No. 00-010-0325. The investigation of evolution of cell parameters wasn't performed due to existence of this parasitic phase.

The high resolution TEM images of the 3% Ni doped GFO in cross section is shown on Figure 4-5. As it is seen on the Figure 4-5(a), the parasitic phase is visible in a separate grain on high resolution image in a different in contrast. It is worth noticing that the grain appears not from the beginning of the growth, but only after 5 nm thick layer (Figure 4-5 b).

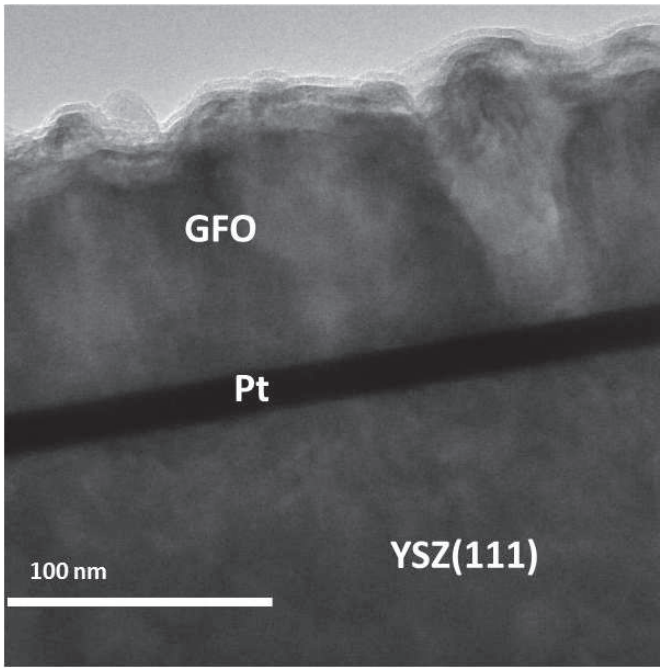

(a)

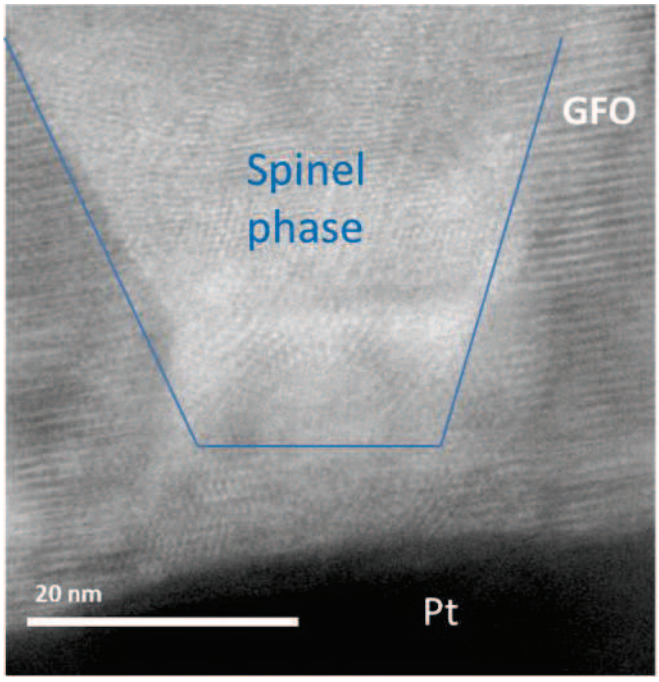

(b)

Figure 4-5. TEM high resolution image of 3% Ni doped layer deposited on Pt(111)//YSZ(111) in cross section : (a) a global view of the thin film, (b) zone showing the spinel phase origin.

3.1.3 Electrical properties

The measurements of leakage currents in the GFO-doped Ni thin films deposited on Pt(111)//YSZ(111) were carried out by S. Cherifi and R. Jarrier (IPCMS, Strasbourg).

Figure 4-6 shows the evolution of the leakage currents versus global Ni content in the structure of GFO. A significant reduction in leakage current is observed when the Ni level increases, reaching a minimum for the compound GFO: Ni 5%.

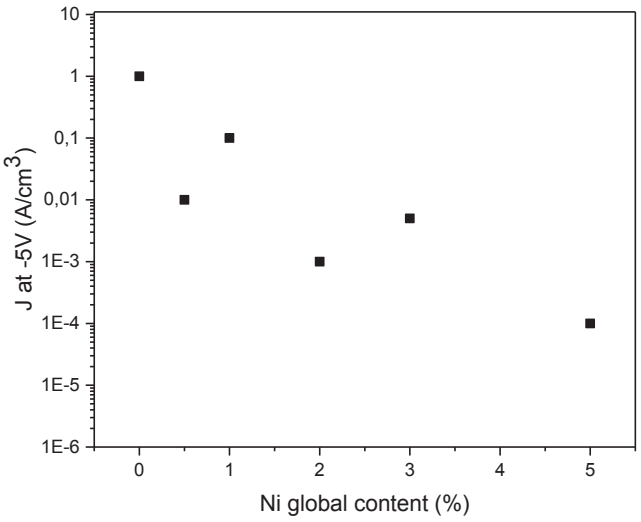

Figure 4-6. Evolution of leakage currents with the global Ni content in the GFO thin films deposited on Pt//YSZ(111).

Leakage currents decrease for increasing doping levels. The reduction in leakage currents can be attributed to the replacement of increasing larger contents of Fe^{2+} ions by Ni^{2+} ions, making difficult the hopping conduction between the different valences of iron.

Ferroelectric measurements were also performed at room temperature at different frequencies, but unfortunately it was not possible to observe any P(E) loop.

Conclusion

It was not possible to obtain Ni doped GFO thin films without parasitic phase on Pt(111)//YSZ(111). The electric characterizations showed that the Ni doping play a considerable role in the decrease of leakage currents, but no polarization loops could be observed. We decided to make some further depositions of Ni doped GFO onto other substrates. Among them, a conducting one STO:Nb(111) and a non-conducting one YSZ(100).

3.2 Thin films of Ni doped GFO deposited on STO:Nb(111)

3.2.1 Structural analysis

The same series of depositions were performed on conducting STO:Nb(111) substrates with the same doping content of Ni as was described in previous paragraph.

The various thin films doped with Ni were analyzed by X-ray diffraction (Figure 4-7). No parasitic phase was detected up to 5% of Ni content.

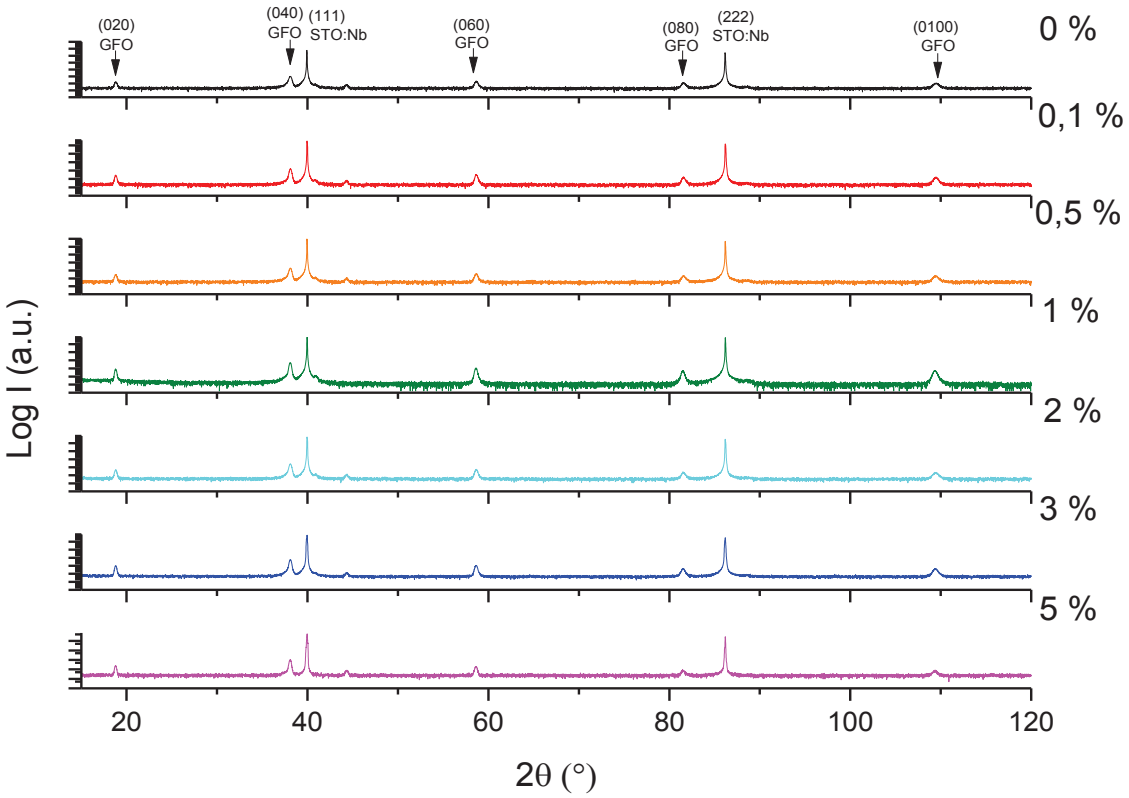

Figure 4-7. Diffractograms of GFO :Ni doped thin films deposited on STO:Nb(111) for concentrations 0.1%-5%

The films are all (0*k*0) oriented for all Ni compositions.

Some *Φ*-scans of the GFO:Ni layers were made on the nodes {570} and {062} of the GFO structure (in the space group $Pc2_1n$), and are presented on Figure 4-8. Six peaks are observed, which are characteristics of three equivalent variants in the plane of the layers.

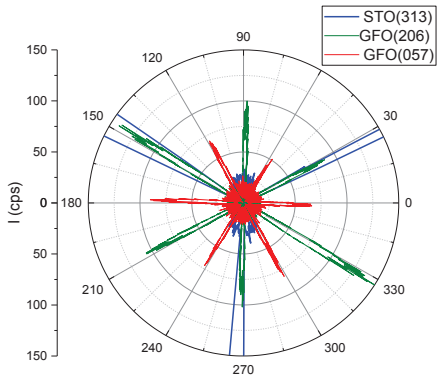

Figure 4-8. *Φ*-scans of the {057} and {206} nodes of undoped GFO deposited on STO:Nb(111) as representative for all films deposited on same substrate.

The orientations of the GFO variants is due to the different matching possibilities of GFO(0k0) onto STO:Nb(111). In order to understand the possible epitaxial relationships between $GFO(001)_{Pna2_1}$ onto STO (111), the reciprocal lattices must be observed in the $[001]_{Pna2_1}$ zone axis for GFO and in the [111] zone axis for STO (Figure 4-9). The possible matching distances are $d_{GFO(060)_{Pna2_1}}$ =1.465 Å and $d_{GFO(330)_{Pna2_1}}$=1.468 Å and $d_{STO(220)}$=1.380 Å. The mismatch is of *ca.* 6% in all cases. The stress is in compression.

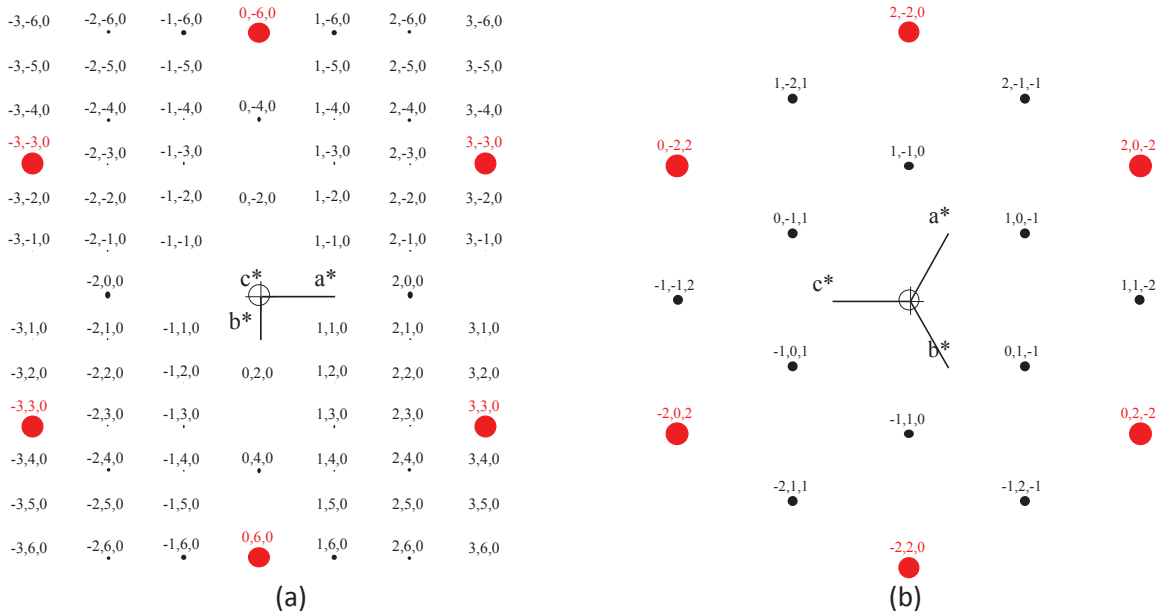

Figure 4-9. Reciprocal lattices of (a) GFO in the $[001]_{Pna2_1}$ zone axis and (b) STO in the [111] zone axis

There are 3 possibilities of matching (Figure 4-10), which may be described according to the following epitaxial relationships:

(a) GFO $(001)_{Pna2_1}$// STO (111), GFO $[060]_{Pna2_1}$// STO [-220],
(b) GFO $(001)_{Pna2_1}$// STO (111) , GFO $[060]_{Pna2_1}$// STO [-202],
(c) GFO $(001)_{Pna2_1}$// STO (111) , GFO $[060]_{Pna2_1}$// STO [0-22],

which may also be written:
(a) GFO $(001)_{Pna2_1}$// STO (111), GFO $[010]_{Pna2_1}$// STO [-110],
(b) GFO $(001)_{Pna2_1}$// STO (111) , GFO $[010]_{Pna2_1}$// STO [-101],
(c) GFO $(001)_{Pna2_1}$// STO (111) , GFO $[010]_{Pna2_1}$// STO [0-11].

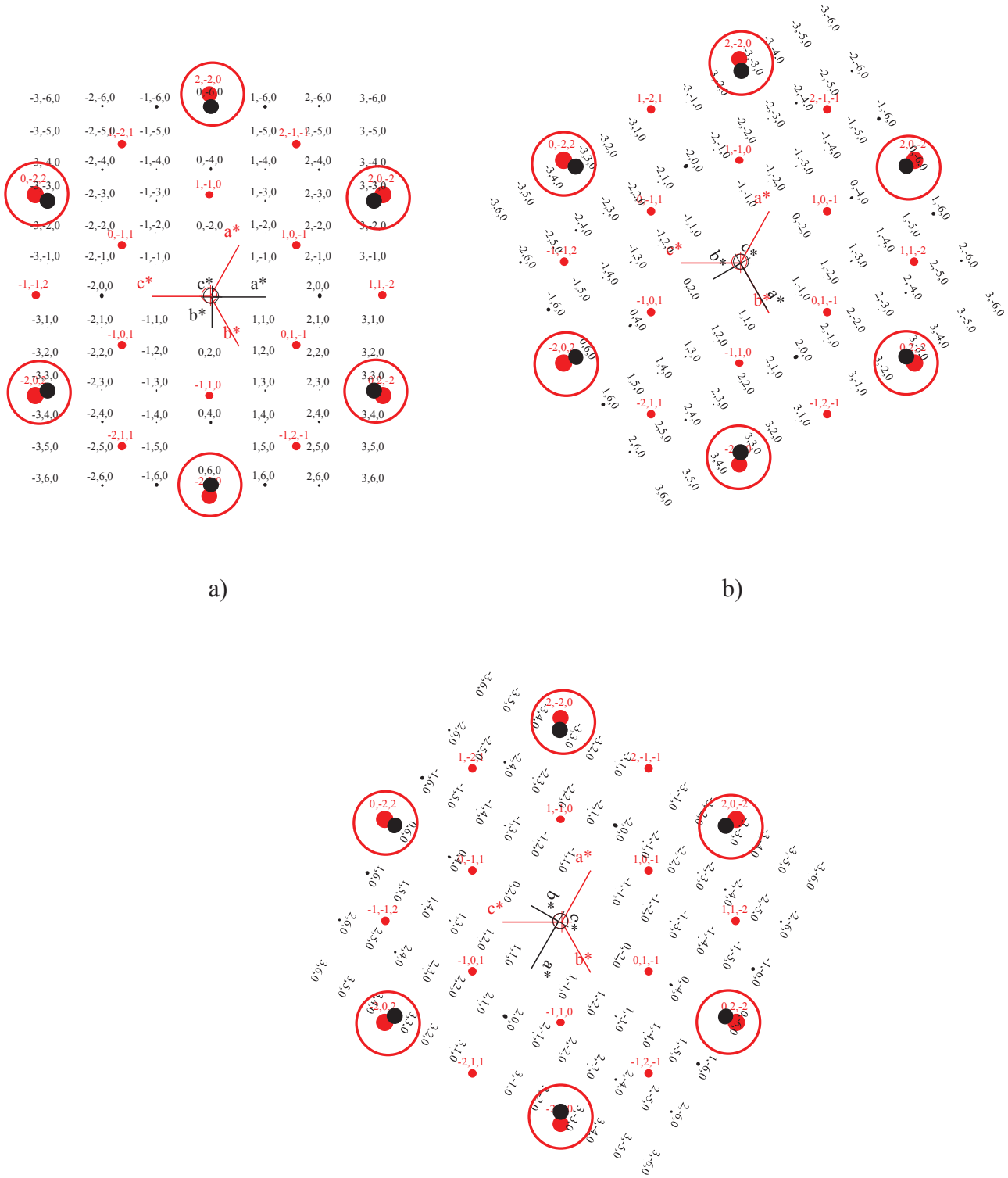

Figure 4-10. The three matching possibilities for the growth of GFO(001)$_{Pna2_1}$ onto STO(111), (the reciprocal lattice of GFO is in black, that of STO in red).

TEM cross section images of GFO$(001)_{Pna2_1}$ thin films onto STO(111) which will show resolution in the substrate part will be taken either in the STO<110> or in the STO<112> zone axes and will allow the simultaneous observation of three variants: the GFO variants in the $[010]_{Pna2_1}$, $[310]_{Pna2_1}$, and $[-310]_{Pna2_1}$ zone axes for an observation of STO in a <110> zone axis, and the GFO variants in $[100]_{Pna2_1}$, $[110]_{Pna2_1}$, and $[-110]_{Pna2_1}$ zone axes, for an observation of STO in the <-211> zone axis (see Figure 4-11).

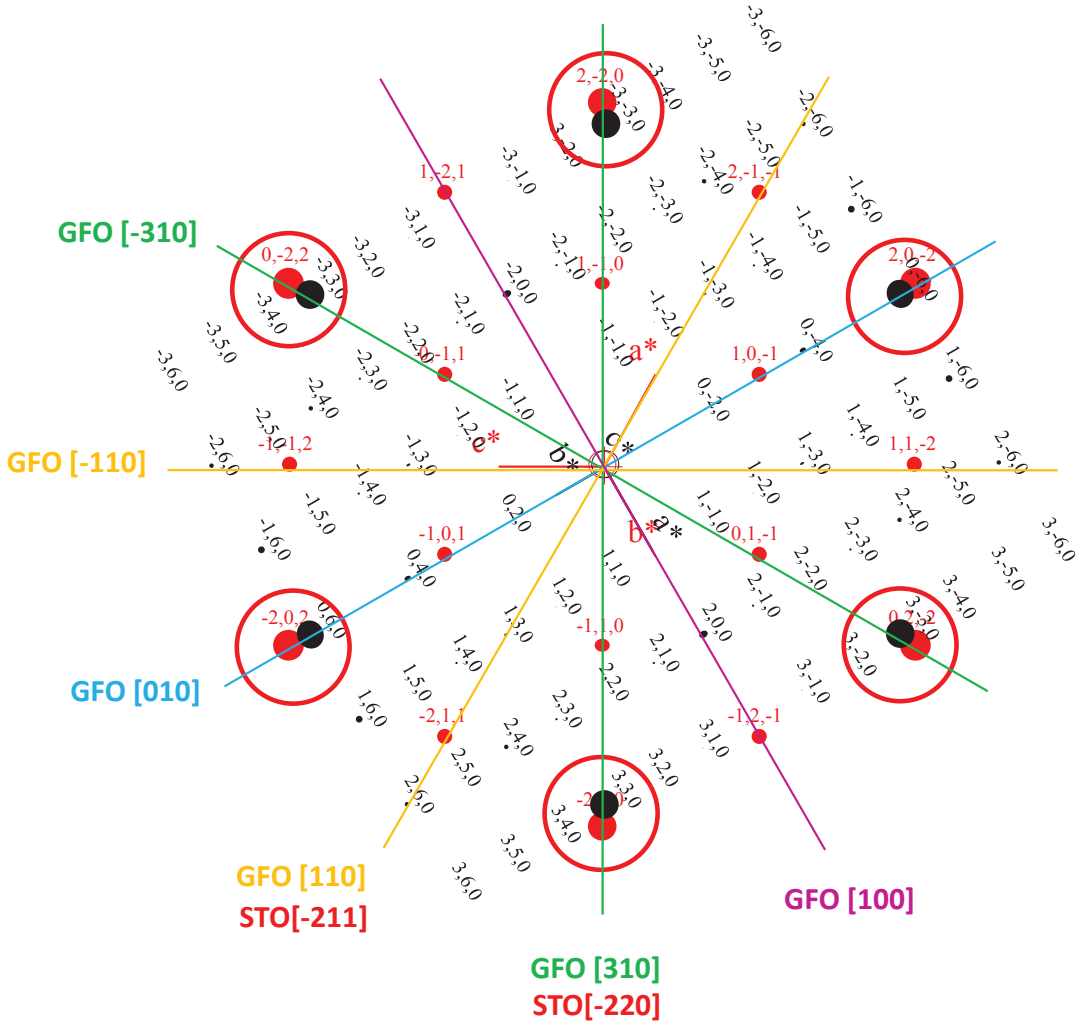

Figure 4-11. The six different zone axes available for observation of GFO thin films in cross views, associated in two groups, depending upon the zone axis in which STO is observed: the $[010]_{Pna2_1}$, $[310]_{Pna2_1}$, and $[-310]_{Pna2_1}$ for an observation of STO in a <110> zone axis, and the $[100]_{Pna2_1}$, $[110]_{Pna2_1}$, and $[-110]_{Pna2_1}$, for an observation of STO in the <112> zone axis.

Four different contrasts are expected, corresponding to four inequivalent zones axes: GFO$[310]_{Pna2_1}$, GFO$[110]_{Pna2_1}$, GFO$[010]_{Pna2_1}$, GFO$[100]_{Pna2_1}$(GFO$[310]_{Pna2_1}$ and GFO$[-310]_{Pna2_1}$, on the one hand, and GFO$[110]_{Pna2_1}$ and GFO$[-110]_{Pna2_1}$, on the other

hand, are strictly equivalent). The reciprocal lattices of GFO in the $[310]_{Pna2_1}$ and $[010]_{Pna2_1}$, on the one hand, and $[110]_{Pna2_1}$ and $[100]_{Pna2_1}$, on the other hand, are very similar and will result in images with similar contrasts (Figure 4-12). So, in fact, only two different contrasts may be observed for GFO, depending upon the zone axis in which STO is observed: the contrast corresponding to the $[010]_{Pna2_1}$ (and $[310]_{Pna2_1}$, $[-310]_{Pna2_1}$) zone axis, for an observation of STO in a <110> zone axis, and the contrast corresponding to the $[100]_{Pna2_1}$ (and $[110]_{Pna2_1}$, $[-110]_{Pna2_1}$) zone axis, for an observation of STO in the <112> zone axis.

Table 4-2. Crystallographic orientations of the two different contrasts which may be observed on TEM images

	STO zone axes	GFO zone axes
TEM contrast 1	<110>	$[010]_{Pna2_1}$ $[310]_{Pna2_1}$ $[-310]_{Pna2_1}$
TEM contrast 2	<112>	$[100]_{Pna2_1}$ $[110]_{Pna2_1}$ $[-110]_{Pna2_1}$

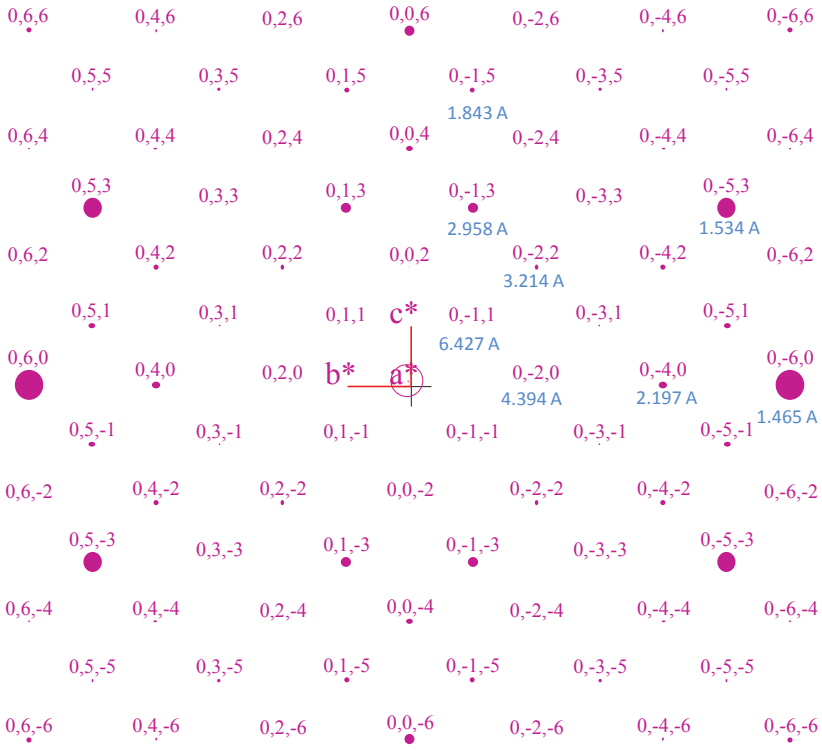

(a) GFO reciprocal lattice in the $[100]_{Pna2_1}$ zone axis

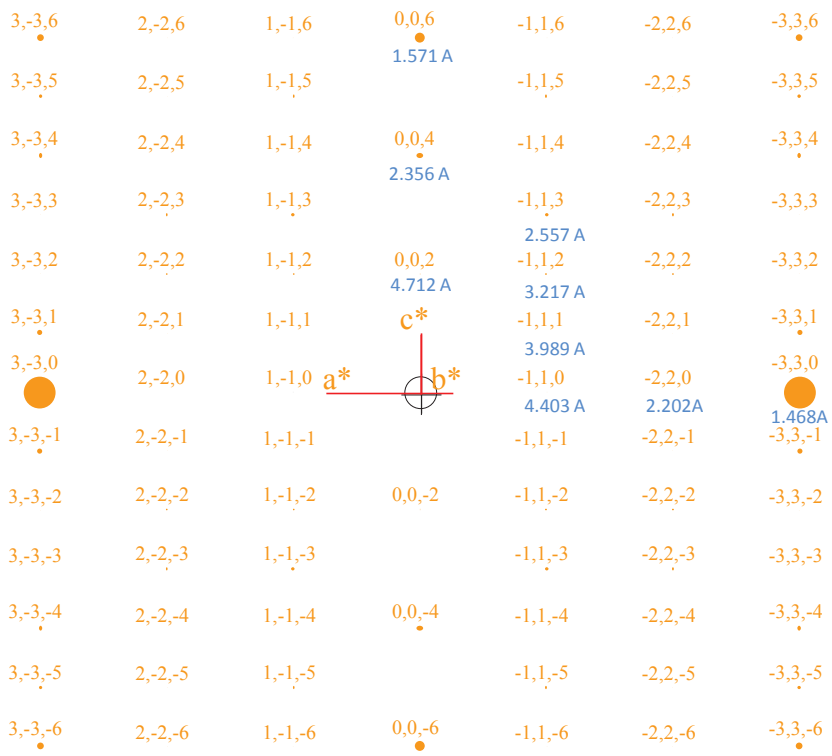

(b) GFO reciprocal lattice in the $[110]_{Pna2_1}$ zone axis

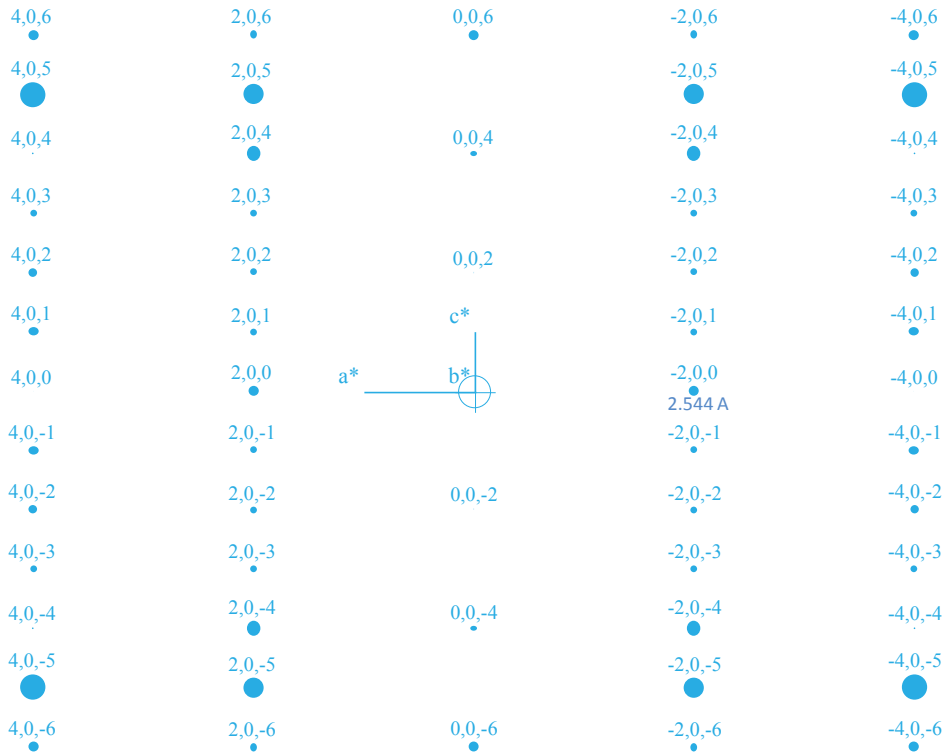

(c) GFO reciprocal lattice in the$[010]_{Pna2_1}$ zone axis

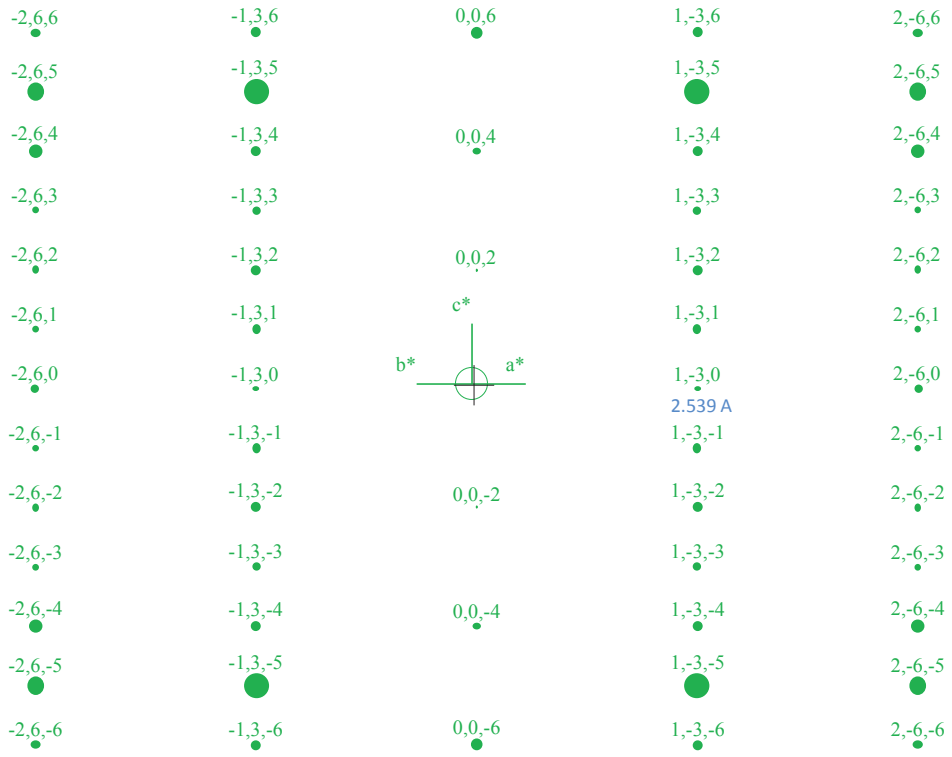

(d) GFO reciprocal lattice in the $[310]_{Pna2_1}$ zone axis

Figure 4-12. GFO reciprocal lattices in the (a) $[100]_{Pna2_1}$, (b) $[110]_{Pna2_1}$, (c) $[010]_{Pna2_1}$, and (d) $[310]_{Pna2_1}$ zone axes. The patterns of the $[100]_{Pna2_1}$ and $[110]_{Pna2_1}$ zone axes, on the one hand, and $[010]_{Pna2_1}$ and $[310]_{Pna2_1}$ zone axes, on the other hand, are very similar.

It is possible to simulate the contrast observed on TEM images using the JEMS software package (P.A. Stadelmann), using the parameters of the used microscope (JEOL 2100 FCs corrected from spherical aberration at the condenser) and choosing the defocus and thickness parameters, which can change from one image to another. The first step consists in calculating the projected potentials of the cell along the chosen zone axis (Figure 4-13).

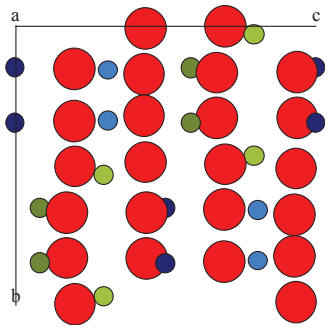

(a)

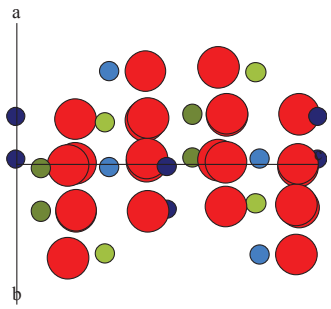

(a)

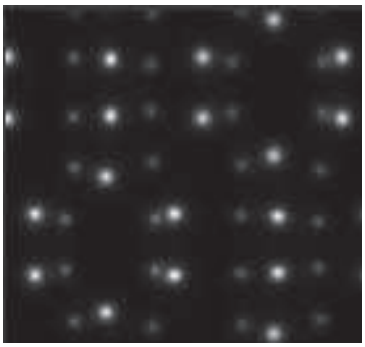

(b)

(a) GFO cell in the $[100]_{Pna2_1}$ zone axis and (b) its projected potential

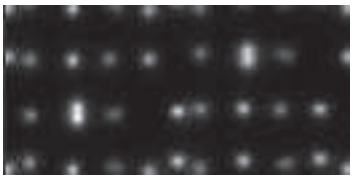

(b)

(a) GFO cell in the $[110]_{Pna2_1}$ zone axis and (b) its projected potential

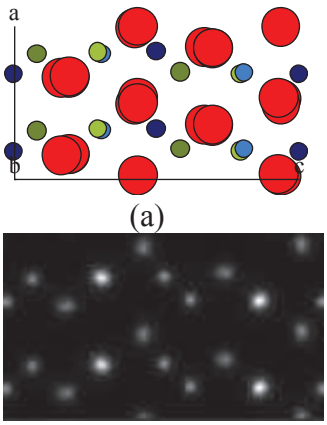

(a)

(b)

GFO cell in the $[010]_{Pna2_1}$ zone axis

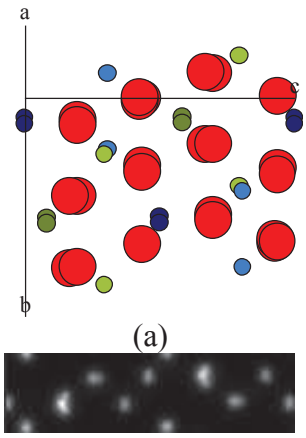

(a)

(b)

GFO cell in the $[310]_{Pna2_1}$ zone axis

Figure 4-13. GFO cells and projected potentials for orientations in the $[100]_{Pna2_1}$, $[110]_{Pna2_1}$, $[010]_{Pna2_1}$, and $[310]_{Pna2_1}$ zone axes.

Figure 4-14 shows a TEM image of a pure GFO1.4 thin film on STO(111) in cross view. The growth is columnar with columns of *ca.* 10-15 nm wide. As expected, only one type of contrast is visible for the entire image. The contrast corresponds to the observation of STO in the <110> zone axis, and GFO in either the $[310]_{Pna2_1}$, $[-310]_{Pna2_1}$ or $[010]_{Pna2_1}$ zone axes, as confirmed by the electronic diffraction pattern of this cross view (Figure 4-15).

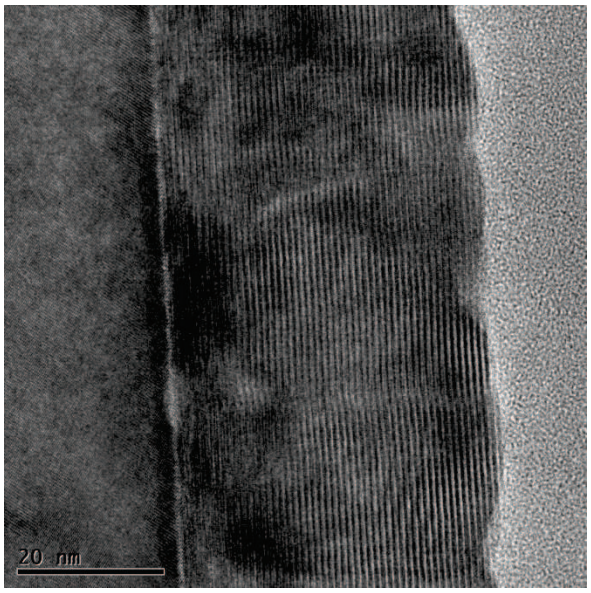

(a)

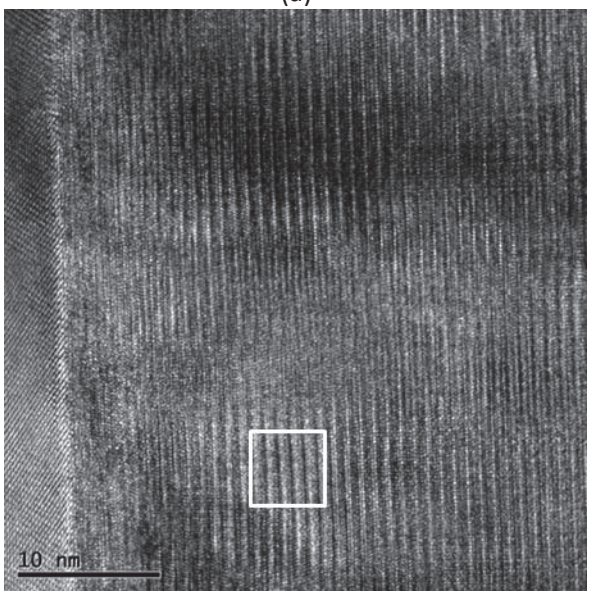

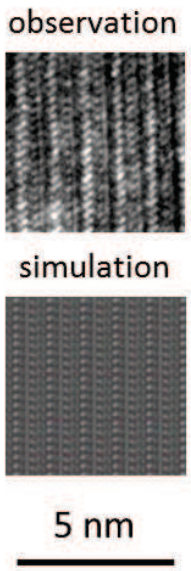

(b)

Figure 4-14. (a) TEM cross view of an undoped GFO1.4 thin film deposited on STO:Nb(111). Only one type of contrast is visible: the one corresponding to GFO in either the $[010]_{Pna2_1}$, $[310]_{Pna2_1}$, or $[-310]_{Pna2_1}$ zone axes (TEM contrast 1) (sample prepared by FIB). (b) Same observation at higher magnification, with a simulation of the contrast in the white square performed with the JEMS software package (P.A. Stadelmann) for a JEOL 2100 FCs corrected from spherical aberration at the condenser (defocus=11 nm, thickness=30 nm).

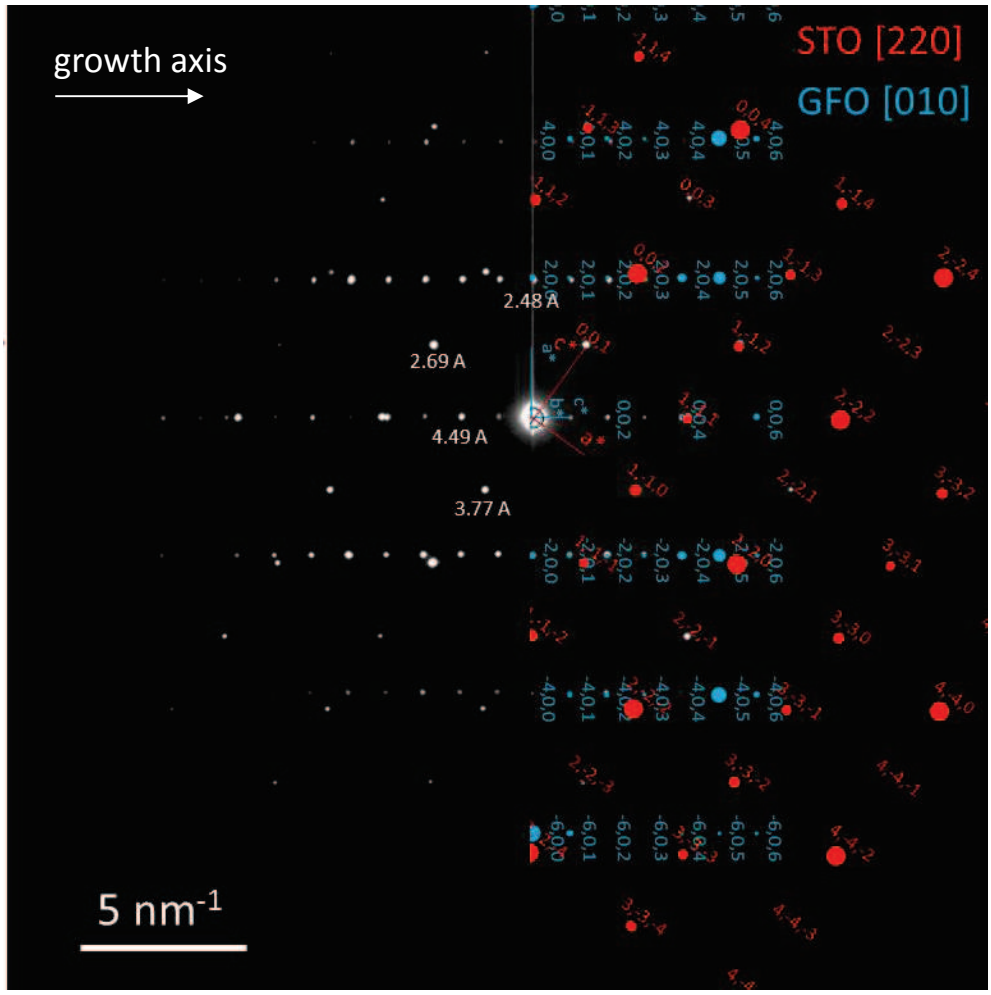

Figure 4-15. (a) Electronic diffraction pattern of the undoped GFO1.4 thin film deposited on STO:Nb(111) of which cross views are presented on Figure 4-14. (b) STO is visible in its [110] zone axis and GFO can be indexed in the $[010]_{Pna2_1}$ zone axis, as an example, but could also be indexed in the $[310]_{Pna2_1}$ or$[-310]_{Pna2_1}$ zone axes (similar patterns).

The TEM observation of cross views of the Ni-doped GFO films deposited onto STO substrates show that the first 5-10 nm of the growth do not present the same contrast as the rest of the films (Figure 4-16).

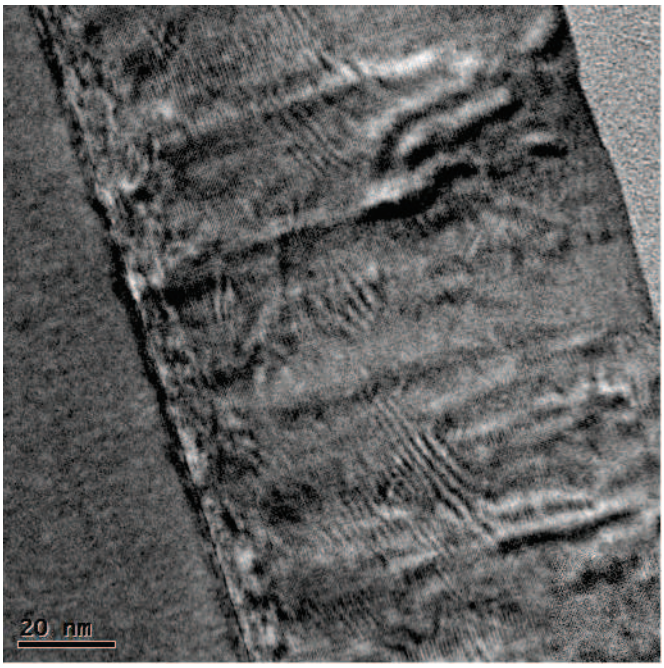

Figure 4-16. TEM cross view image of a 3%-Ni-doped GFO thin film deposited onto STO, showing a difference in contrast between the first 5-10 nm of the growth and the rest of the film (sample prepared by FIB).

When performing fast Fourier transform (FFT) of these first 5-10 nm of the film, one obtains a pattern which matches with a spinel-like phase (space group *F*d-3m), while the rest of the image show FFT corresponding to GFO in the $[100]_{P\mathrm{na}2_1}$ zone axis (TEM contrast 2) (Figure 4-17). This cross view is therefore not in the same orientation as that of the undoped sample presented in Figure 4-14, but this does not explain the peculiar contrast of the first 5-10 nm. The precision of the measurement of the distances in the FFT image is too low to give a precise value of the cell parameter of the spinel-like phase, but it is of *ca.* 8.3(1)Å, therefore within the range of the expected cell parameters for Fe_3O_4 (8.3985 Å, ICDD pattern #04-015-9120), $GaFe_2O_4$ (8.378 Å,ICDD pattern #01-072-9576), or $NiFe_2O_4$ (8.334 Å, ICDD pattern #04-014-8286), for example.

(a)

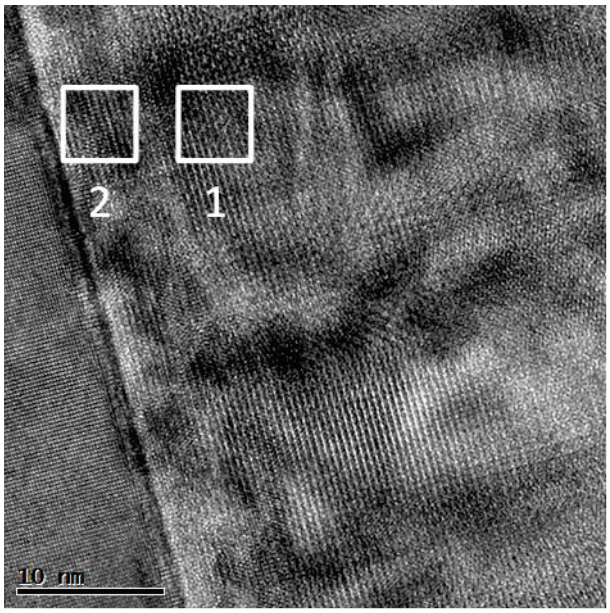

(b1)

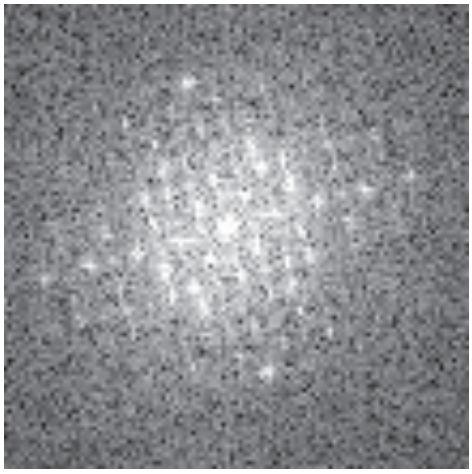

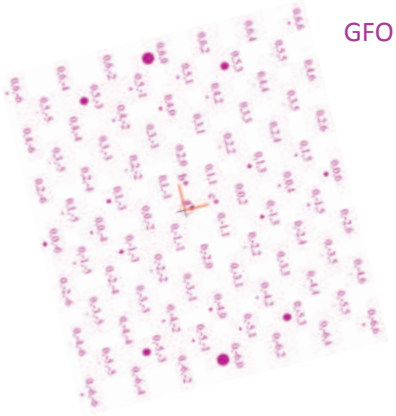

GFO [100]

(b2)

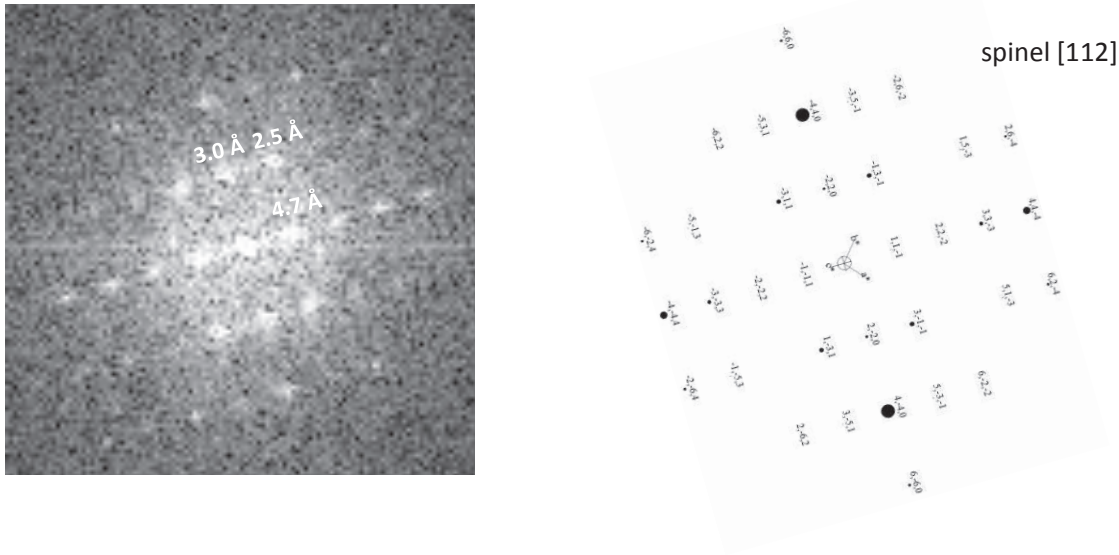

Figure 4-17. (a) Same image as in Figure 4-16 with higher magnification, and (b) FFT of parts of the image taken in (1) the first 5-10 nm of the growth and (2) at a thickness higher than 10 nm. The FFT patterns match with (1) GFO in the $[100]_{Pna2_1}$ zone axis, and (2) a spinel-like phase in the [112] zone axis.

The electronic diffraction pattern of this 3% Ni-doped GFO thin film deposited on STO:Nb(111) is presented on Figure 4-18. STO is visible in its [112] zone axis and GFO can be indexed in the $[100]_{Pna2_1}$ zone axis, as expected from Figure 4-17. One can notice that the GFO layer is fully relaxed and not strained by the substrate. Some extra dots are seen as superintensities along lines perpendicular to the growth axis. They probably result from stacking faults between adjacent grains. The superintensities in the yellow circles, d=2.5Å, are perfectly integrated within the GFO pattern; they could correspond to $(032)_{Pna2_1}$ dots of the GFO phase. However the $(032)_{Pna2_1}$ reflection is excluded from the GFO diffraction pattern by extinction conditions. These conditions may of course be removed if one considers some displacements, even small, of the atoms away from their original crystallographic sites. This would lower the symmetry and allow some forbidden reflections. Still, the d=2.5Å dots present on the diffraction pattern also present a contrast which is slightly different from the other dots originating from this phase. This could be because they result from the 5-10 nm interfacial zone which presents the reciprocal lattice shown in Figure 4-17 (b2). A spinel-like phase matches with those extra spots (Figure 4-19). One can notice that numerous periodicities are similar in GFO and the spinel-like phase. This is due to the fact that both structures derive from similar close packed of oxygens stackings, respectively ABAC for GFO and ABCABC for the spinel-like phase. Stacking faults allow to go from one to the

other. As expected from similarities between the GFO and spinel-like phases, the growth axis for the spinel-like phase is along its [111] axis, similar to the $[001]_{Pna2_1}$ axis of the GFO phase in the fact that it is along the direction of the oxygen stacking.

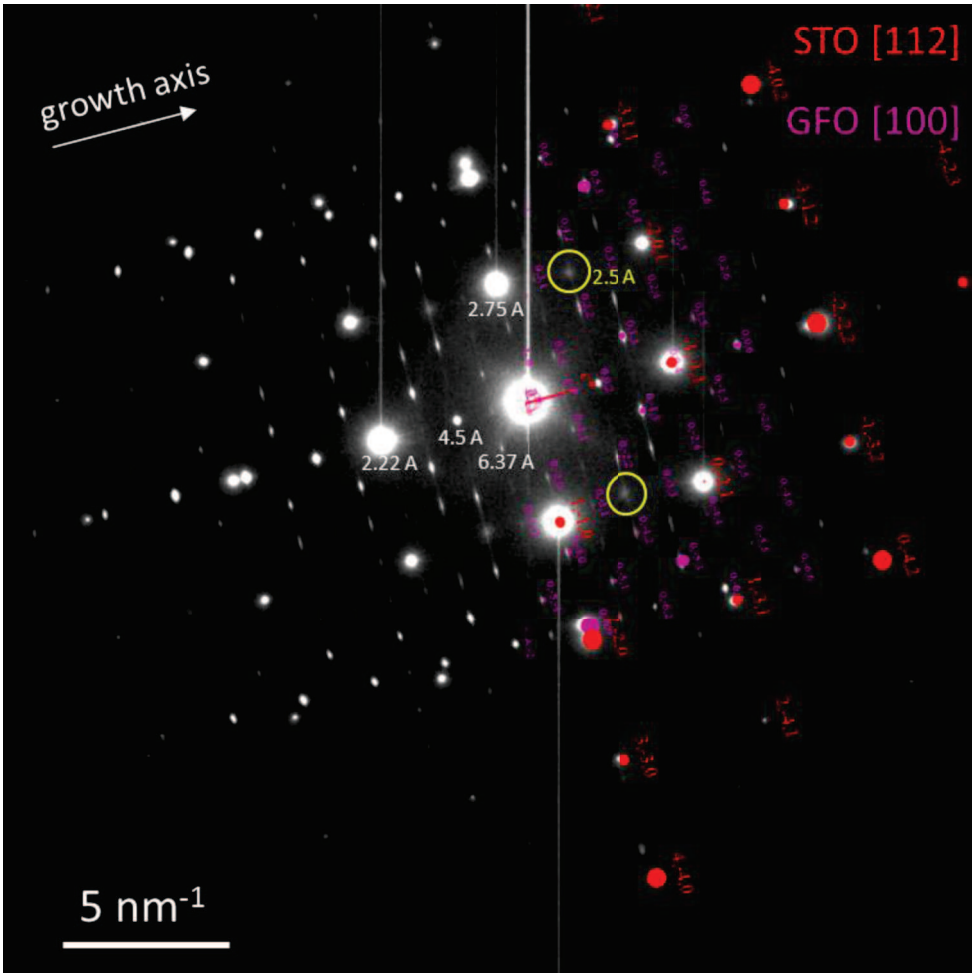

Figure 4-18. Electronic diffraction pattern of the 3% Ni-doped GFO thin film deposited on STO:Nb(111) of which cross views are presented on Figure 4-15. STO is visible in its [112] zone axis and GFO can be indexed in the $[100]_{Pna2_1}$ zone axis. Some extra dots are seen as superintensities along lines perpendicular to the growth axis. The superintensities in the yellow circles present a contrast which is slightly different from the others.

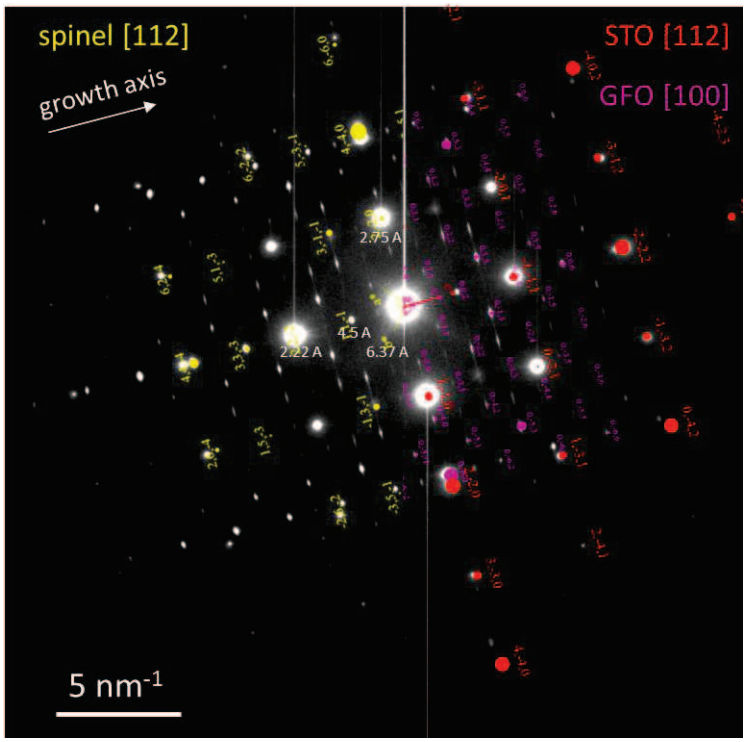

Figure 4-19. Electronic diffraction pattern of the 3% Ni-doped GFO thin film deposited on STO:Nb(111). The additional spots observed in Figure 4-18 may be accounted for when considering a spinel-like phase (a≈8.3Å) in its [112] zone axis. The matching along the growth axis is along the [111] axis of the spinel-like phase.

When observed along the STO:Nb[110] zone axis (on another TEM preparation, Figure 4-20), GFO is observed in its $[010]_{Pna2_1}$ (or equivalent, namely $[310]_{Pna2_1}$ or $[-310]_{Pna2_1}$) zone axis. Some extra spots are also observed, in particular with a distance of *ca.* 2.5 A. The presence of these extra spots can again be understood when considering the existence of a periodicity corresponding to a spinel-like phase in the [011] zone axis (Figure 4-21). This configuration presents two directions for the [111] axis, which is the one matching with the growth direction. One can see that both directions are present on the diffraction pattern (Figure 4-21).

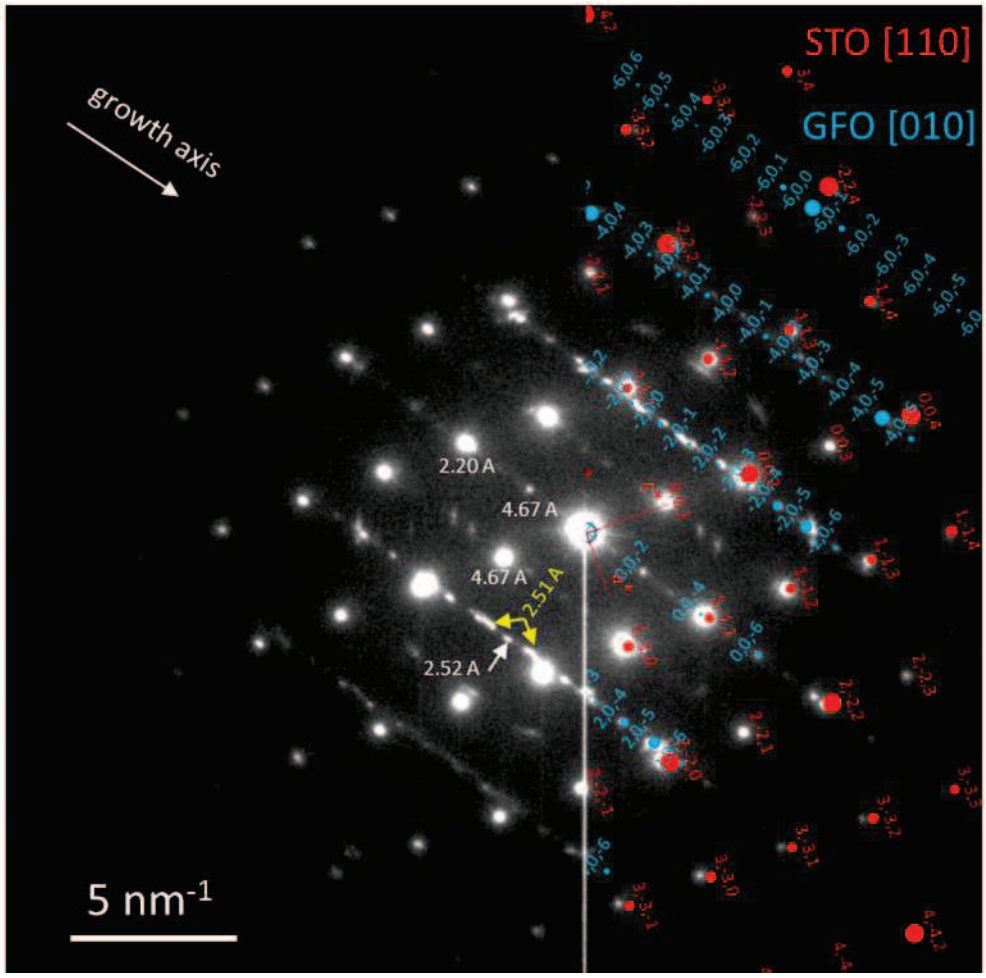

Figure 4-20. Electronic diffraction pattern of the 3% Ni-doped GFO thin film deposited on STO:Nb(111), with STO in its [110] zone axis and GFO indexed in the $[010]_{Pna2_1}$ zone axis. Some extra dots are seen, with distances d=2.5 Å for example (yellow arrows).

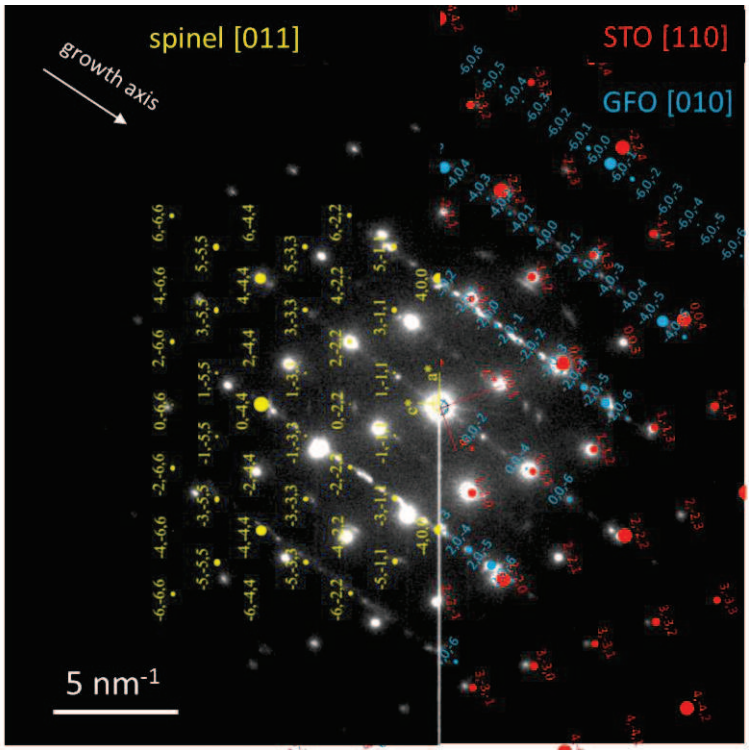

(a)

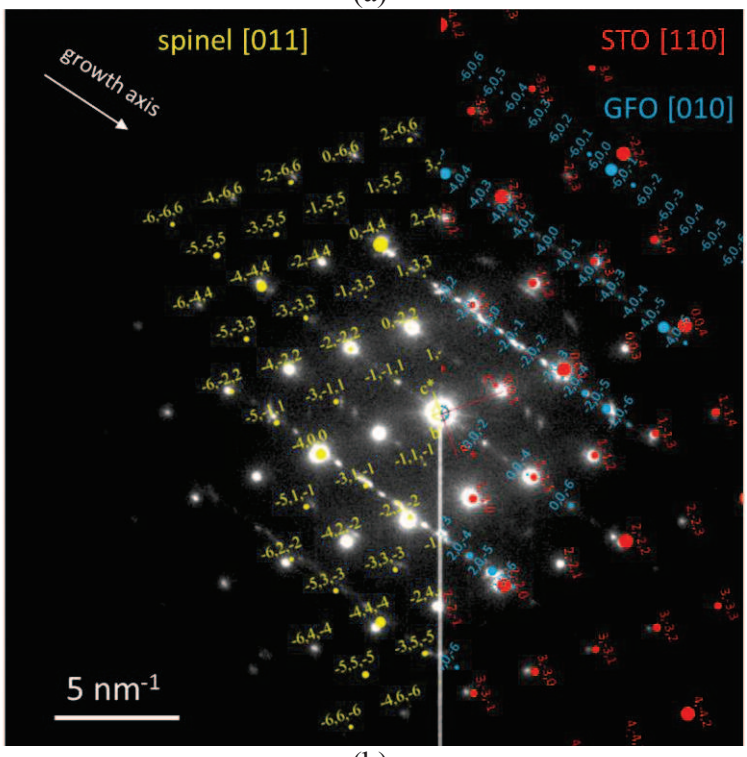

(b)

Figure 4-21. Electronic diffraction pattern of the 3% Ni-doped GFO thin film deposited on STO:Nb(111). The additional spots observed in Figure 4-20 may be accounted for when considering a spinel-like phase (a≈8.3Å) in its [110] zone axis. The matching along the growth axis is along the [111] axis of the spinel-like phase and two orientations are possible: (a) and (b). Both are observed and explain the extra dots of the electron diffraction pattern.

The growth of this spinel-like phase at the interface between the STO:Nb (111) substrate and the GFO layer can be understood when considering its possible epitaxial matchings with these materials (Figure 4-22). The matching possibilities of the spinel-like phase onto STO are similar to those of GFO. The possible observations of this phase may therefore be established in a similar way as we established those for GFO onto STO (*Table 4-3*).

Figure 4-21 is therefore an example for TEM contrast 1 and Figure 4-19 for TEM contrast 2.

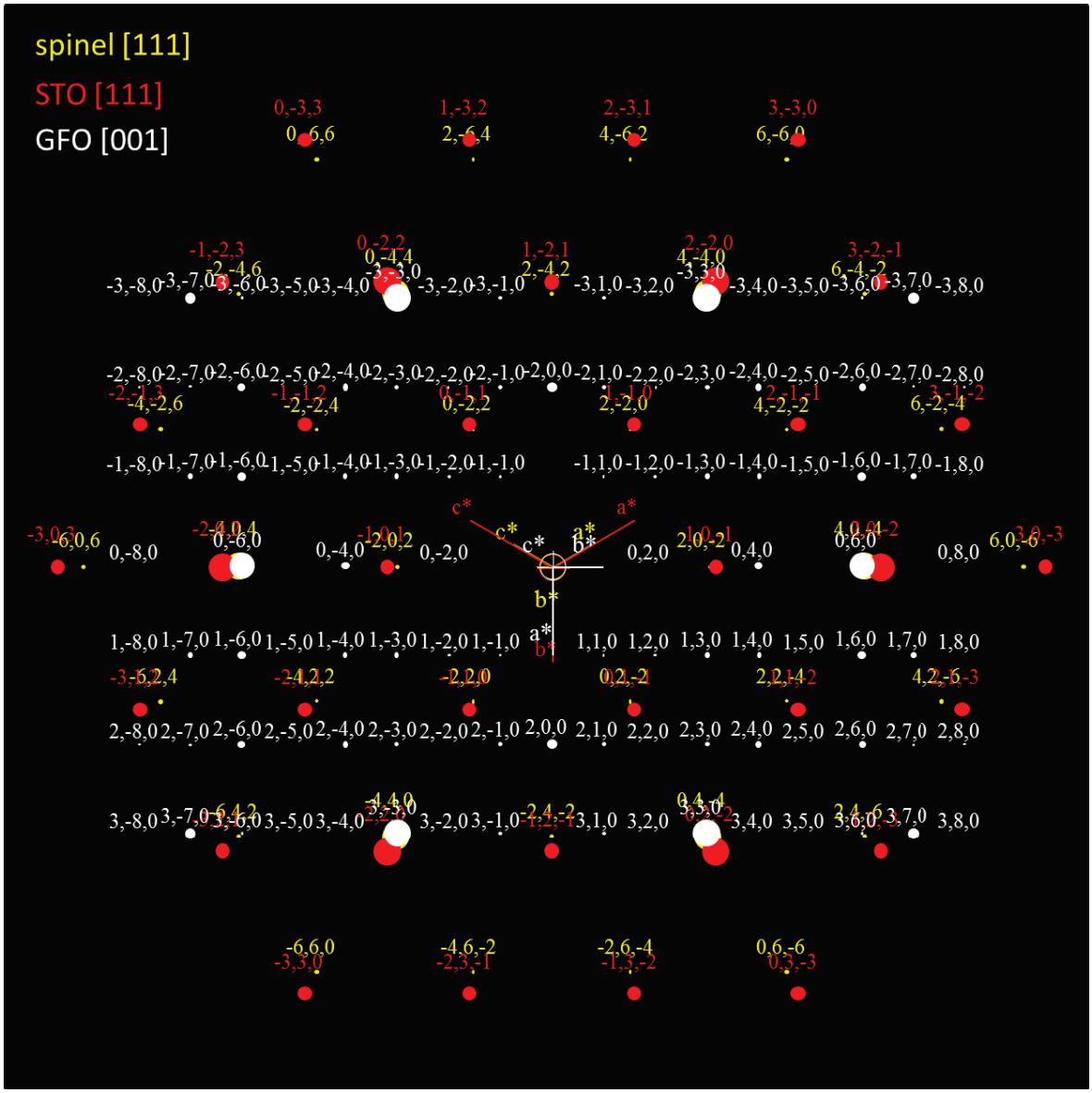

Figure 4-22. Reciprocal lattices of the STO:Nb substrate, GFO, and spinel-like phase in their [111], $[001]_{Pna2_1}$ and [111] zone axes, respectively, showing the possible matchings for epitaxial growth.

Table 4-3. Crystallographic orientations of the two different contrasts which may be observed on TEM images, including the possibility to observe a spinel-like phase

	STO zone axes	GFO zone axes	Spinel-like phase zone axes
TEM contrast 1	<110>	$[010]_{Pna2_1}$ $[310]_{Pna2_1}$ $[-310]_{Pna2_1}$	<110>
TEM contrast 2	<112>	$[100]_{Pna2_1}$ $[110]_{Pna2_1}$ $[-110]_{Pna2_1}$	<112>

The composition of the layer is homogeneous over the entire thickness, with Ga, Fe, and Ni contents in very good agreement with the expected values for x% Ni-doped GFO1.4, *i.e.* $Ga_{0.6}Fe_{1.4-2x}Ni_{2x}$. Figure 4-23 shows an EDX analysis in scanning transmission electron microscopy high angle annular dark field (STEM HAADF) mode of the cross view of a 3% Ni-doped GFO film as an example.

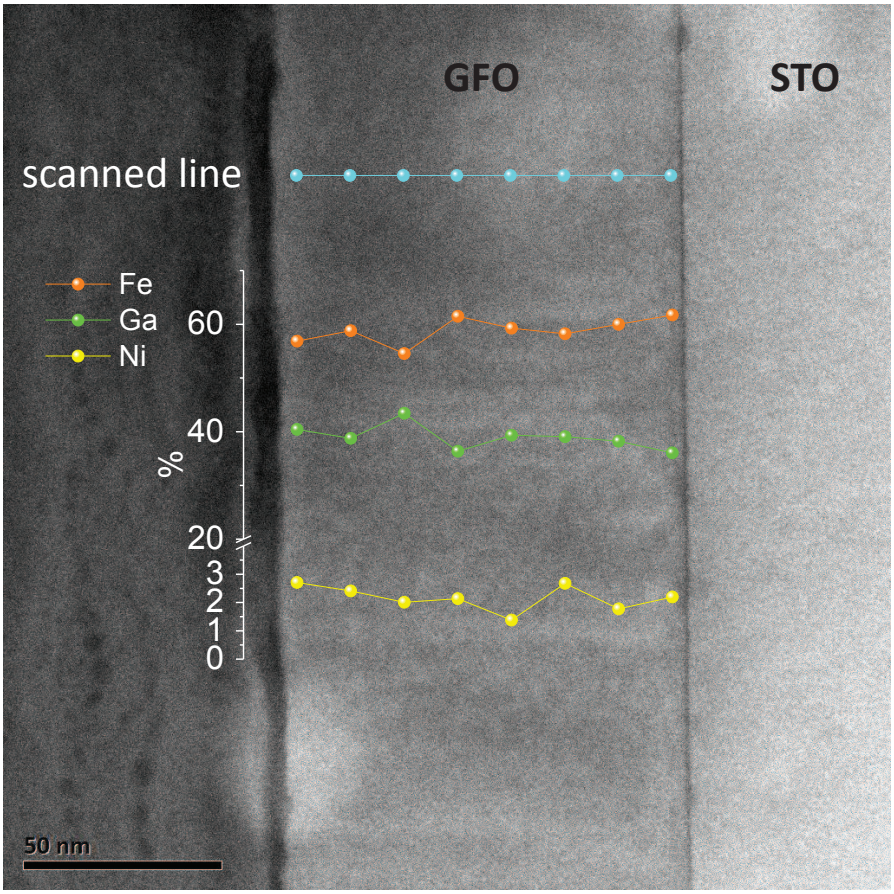

Figure 4-23. Cross view composition of the 3% Ni-doped GFO thin film deposited on STO:Nb(111), determined from EDX analysis in STEM HAADF mode.

The 5-10 nm layer of spinel-like phase is not visible on the undoped GFO films deposited on STO:Nb(111). However some dots, which could belong to the spinel-like phase and not to the *P*na2$_1$ GFO phase, are also present on the FFT of the interfacial part of the film, and not in the rest of the layer, as an indicator of the presence of this periodicity typical of the spinel-phase.

The spinel like phase could not be detected on the *θ–2θ* diffractogram because it adopts exactly the same out-of-plane parameter as the GFO one.

The cell parameters of the GFO phase of the films were determined from {057} and {206} nodes. Their evolution with the Ni content is plotted on Figure 4-24.

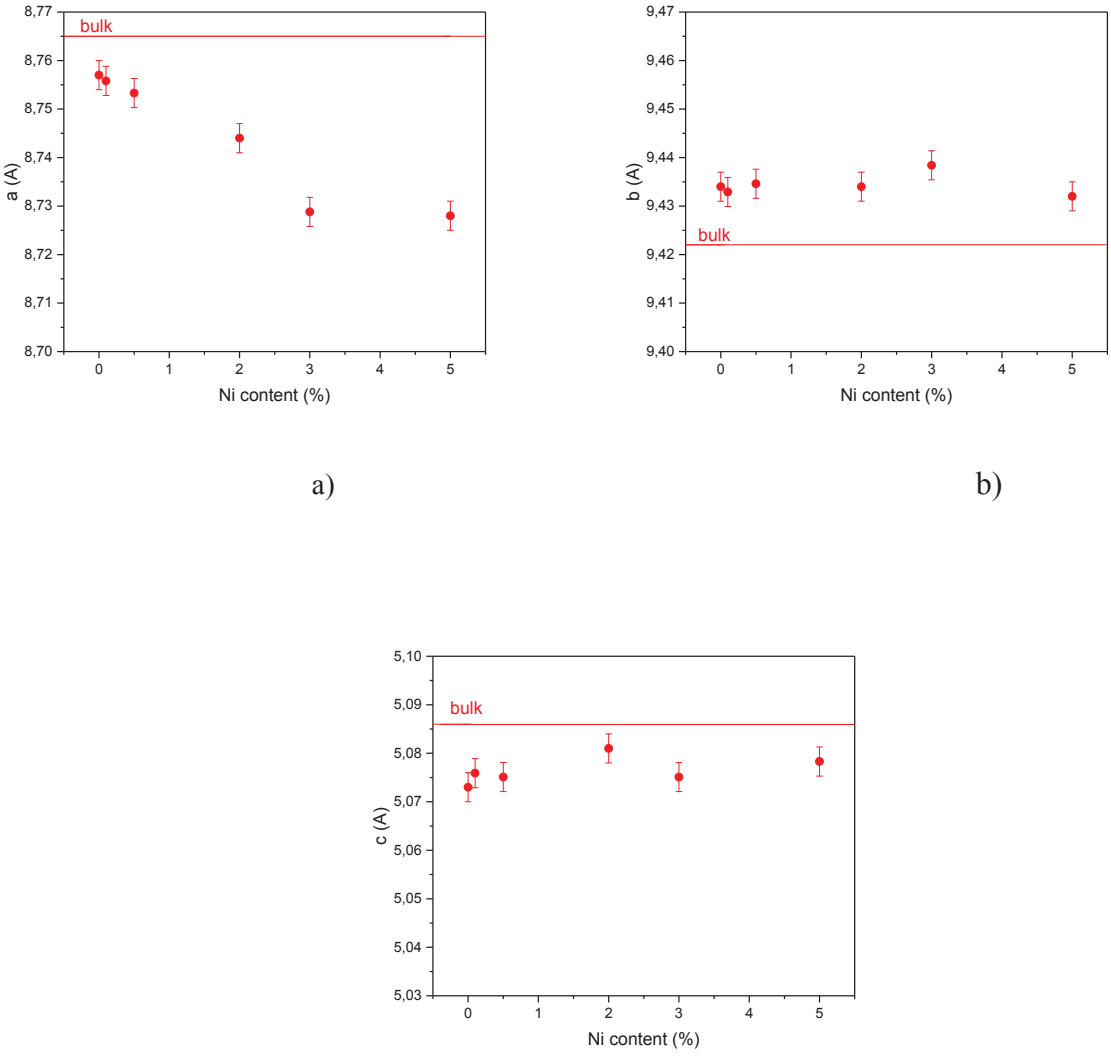

a) b)

c)

Figure 4-24. The evolution of cell parameters with Ni insertion into the structure of the GFO thin films deposited on STO:Nb(111).

The *a* and *c* parameters are smaller than expected for bulk, when the *b* parameter is higher. The a parameter tends to decrease with the Ni content, but the out-of-plane parameter b and the in-plane parameter c stay more or less the same. The fact that the in plane cell parameters are smaller in thin film than in bulk for all Ni contents, can't be explained by a stress which could be imposed by the substrate because, as can be seen in Figure 4-25, the GFO layer is fully relaxed and its in-plane parameters do not follow those of STO:Nb.

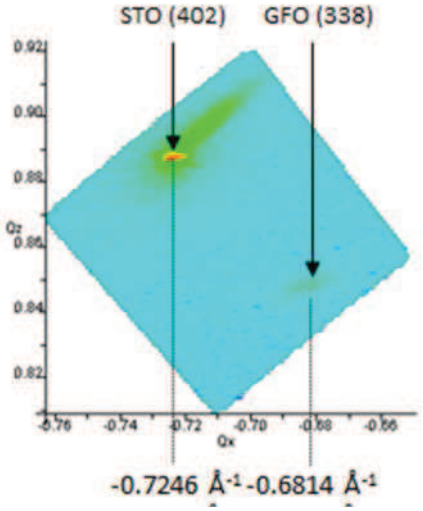

Figure 4-25. Rsm maps for the nodes of STO:Nb (402) $_{Pna21}$ and GFO (338)$_{Pna21}$.

The elongation of the GFO cell along its b axis is therefore more likely to be related to the existence of oxygen vacancies within the material.

3.2.3 Magnetic properties

The magnetic properties of the films were studied by SQUID magnetometry. The hysteresis cycles measured at 5 and 300 K are shown in Figure 4-26. Hysteresis loops measured at 300 K indicate that the samples are more easily magnetized within the plane of the films (ac plane) ($Pc2_1n$) than out of plane (b direction). This is consistent with the easy and hard magnetization axes observed in single crystal: c is the easy axis while b is the hard axis. Magnetization in GFO results from the uncompensated antiparallel ordering of two sublattices constituted by the Ga1 and Fe1 sites, on the one hand, and Ga2 and Fe2, on the other hand. It strongly depends upon the cation distribution on the four different sites [11]. The cations contributing to the samples magnetization are Fe^{3+} (5 μB), Fe^{2+} (4 μB), and Ni^{2+} (2 μB).

GFO:Ni 0%

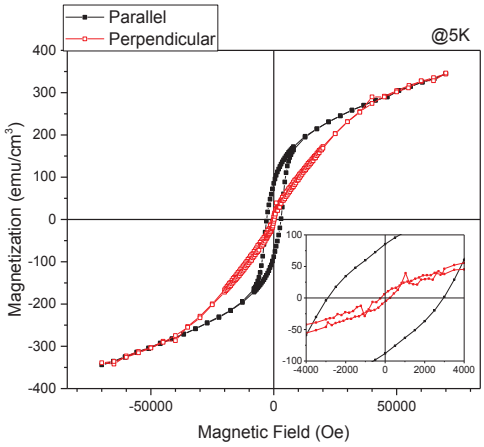

(a)

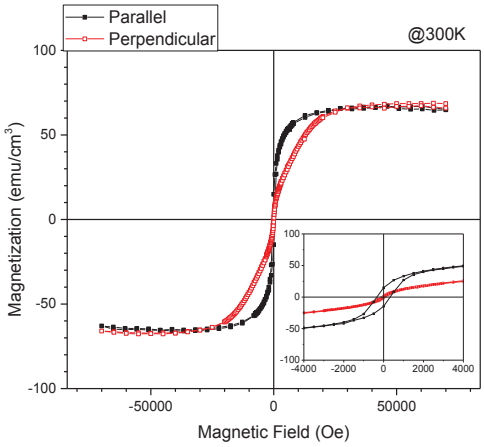

(b)

GFO:Ni 0.1%

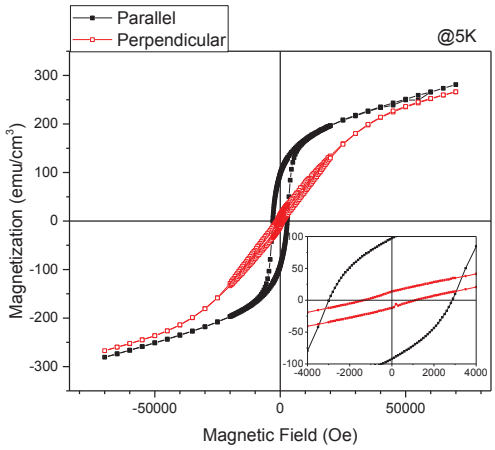

(c)

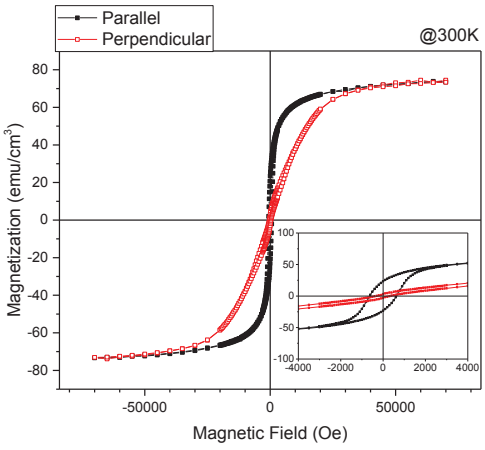

(d)

GFO:Ni 0.5%

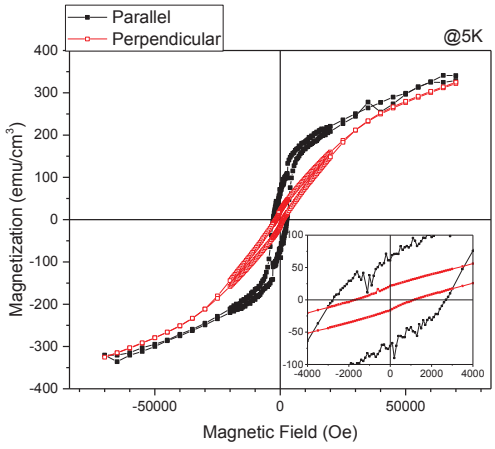

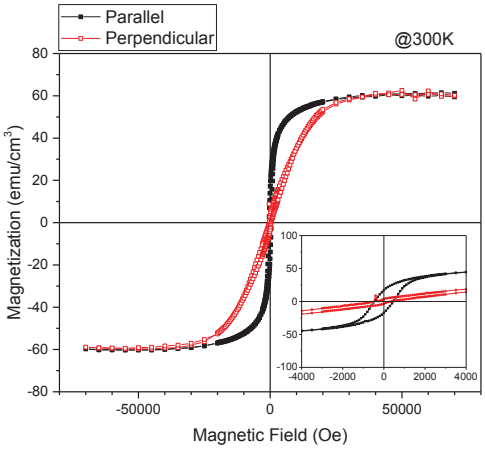

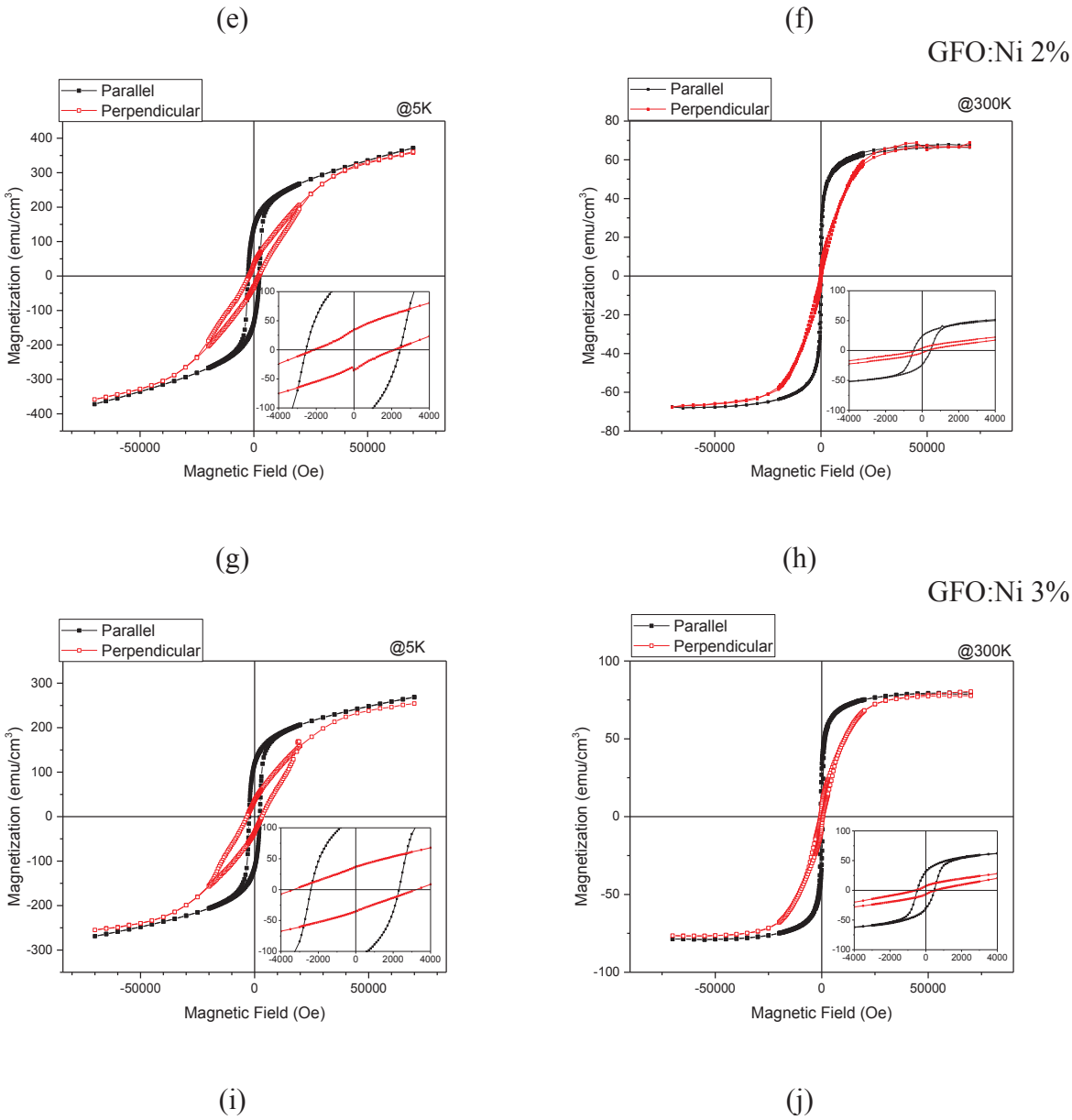

Figure 4-26. Hysteresis loops of the (a.b) undoped, and Ni (c,d) 0.1% (e,f) 0.5%, (g,h) 2%, (i, j) 3% doped GFO thin films, measured at 5 K and 300 K in parallel (filled black squares) and perpendicular (red hollow squares).

A small exchange bias could be observed for the measurements performed at 5 K (*Table 4-4*). The error bar being ±30 Oe, only samples 0.1 and 0.5% show a real exchange bias in perpendicular. No exchange bias was observed at room temperature.

Table 4-4. Coercive fields and exchange bias observed on hysteresis cycles measured at 5 K for GFO:Ni samples deposited on STO:Nb(111)

	Parallel measurements		Perpendicular measurements	
Ni %	Hc (Oe)	Exchange bias (Oe)	Hc (Oe)	Exchange bias (Oe)
0	2932	12	240	0
0.1	2926	-73	1465	-147
0.5	2734	-32	1428	-272
2	2501	-44	2121	25
3	2347	-42	3295	-45

The observed bias may be due to the interaction between phases in the film: the orthorhombic GFO one and probably the spinel that could be observed by TEM. This additional phase in 5 nm thick layer between substrate and the GFO layer (Figure 4-16).

The fact that no exchange bias is observed at room temperature means that the ordering temperature of this spinel like phase is below room temperature. No shift of the hysteresis loops in magnetization is observed. The same values are measured for + and – 70 000 Oe. This means that if the spinel like phase is responsible for the coupling. It is antiferromagnetic and has no resulting magnetization.

No electric characterizations could be performed on those samples because the substrate isn't conducting enough for measurements in perpendicular configuration and too conducting for parallel configuration.

3.3 Thin films of Ni doped GFO deposited on YSZ(100)

3.3.1 Structural analysis

In order to continue the investigation of the influence of Ni doping, further series of GFO depositions were performed on YSZ(100). Figure 4-27 present their x-ray diffractograms.

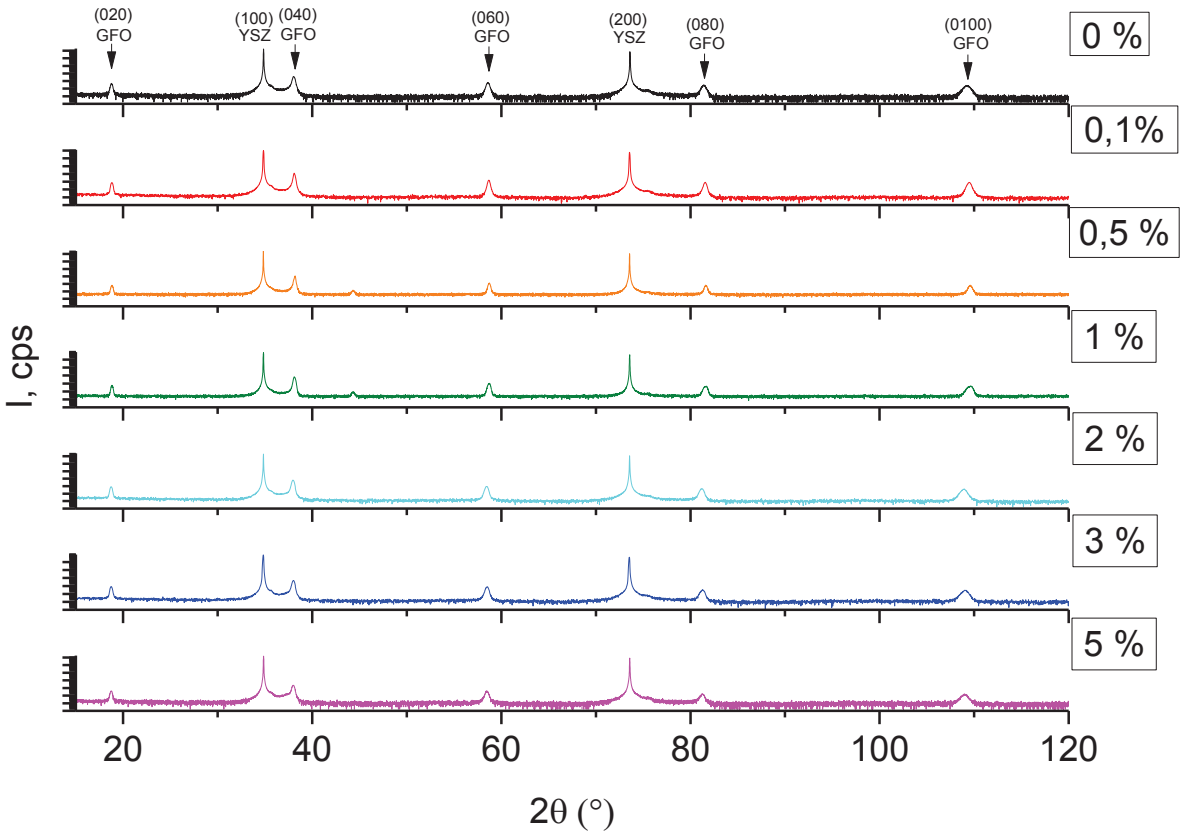

Figure 4-27. X-ray diffractograms of GFO :Ni (0-5%) doped thin films deposited on YSZ(100).

The diffractograms show that is possible to insert up to 5% of Ni into the structure without detecting a parasitic phase. The films are well crystallized and oriented along the *b* direction, as demonstrated by the x-ray diffraction patterns of the films in *θ-2θ* mode (Figure 4-27). The *Φ*-scans around reflections (057), (206) for GFO ($Pna2_1$) and (240) of YSZ show the existence of 6 in-plane variants for GFO, at 30° from each other (Figure 4-28). The orientations of the GFO variants are due to the different matching possibilities of GFO (0k0) onto YSZ(100): $c_{Ga_{0.6}Fe_{1.4}O_3} = 0.5086$ nm[12] $\approx a_{YSZ} = 0.5139$ nm (1% mismatch), on the one hand, and $\sqrt{a^2_{Ga_{0.6}Fe_{1.4}O_3} + c^2_{Ga_{0.6}Fe_{1.4}O_3}} \approx 2a_{YSZ}$ (1% mismatch), on the other hand. The

angle between $c_{Ga_{0.6}Fe_{1.4}O_3}$ and the diagonal of the ac plane is $\alpha = \cos^{-1}\left(a_{Ga_{0.6}Fe_{1.4}O_3}/\sqrt{a^2_{Ga_{0.6}Fe_{1.4}O_3} + c^2_{Ga_{0.6}Fe_{1.4}O_3}}\right) \approx 30°$, which explains the existence of six GFO variants located every 30°[14].

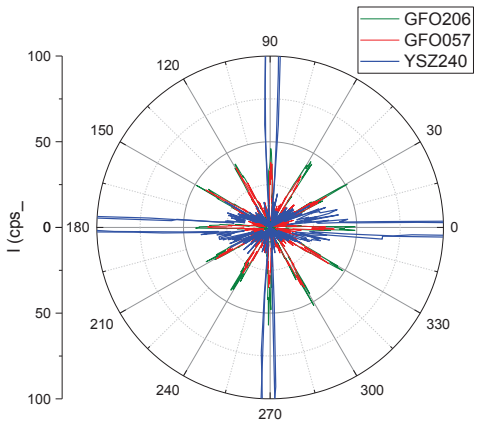

Figure 4-28. ϕ–scans around reflections (570) and (206) of GFO and (240) of YSZ, respectively, for the undoped GFO film, as representative of all films.

The matching possibilities between GFO and the substrates onto which it grows may be predicted from the observation of their reciprocal lattices. For the growth of GFO$(001)_{Pna2_1}$ onto YSZ(001), the reciprocal lattices must be observed in the [001] zone axes for each material (Figure 4-29). The possible matching distances are $d_{GFO(130)_{Pna2_1}}$ =2.539 Å and $d_{GFO(200)_{Pna2_1}}$ =2.544 Å and $d_{YSZ(200)}$=2.570 Å. The mismatch is only of *ca.* 1% in all cases.

There are 6 possibilities of matching (Figure 4-30), which may be described according to the following epitaxial relationships:

(a) GFO $(001)_{Pna2_1}$// YSZ (001), GFO $[200]_{Pna2_1}$// YSZ [200],
(b) GFO $(001)_{Pna2_1}$// YSZ (001), GFO $[110]_{Pna2_1}$// YSZ [020],
(c) GFO $(001)_{Pna2_1}$// YSZ (001), GFO $[110]_{Pna2_1}$// YSZ [200],
(d) GFO $(001)_{Pna2_1}$// YSZ (001), GFO $[200]_{Pna2_1}$// YSZ [020],
(e) GFO $(001)_{Pna2_1}$// YSZ (001), GFO $[-110]_{Pna2_1}$// YSZ [200],
(f) GFO $(001)_{Pna2_1}$// YSZ (001), GFO $[-110]_{Pna2_1}$// YSZ [020],

which can also be written as

(a) GFO $(001)_{Pna2_1}$// YSZ (001), GFO $[100]_{Pna2_1}$// YSZ [100],
(b) GFO $(001)_{Pna2_1}$// YSZ (001), GFO $[110]_{Pna2_1}$// YSZ [010],
(c) GFO $(001)_{Pna2_1}$// YSZ (001), GFO $[110]_{Pna2_1}$// YSZ [100],
(d) GFO $(001)_{Pna2_1}$// YSZ (001), GFO $[100]_{Pna2_1}$// YSZ [010],
(e) GFO $(001)_{Pna2_1}$// YSZ (001), GFO $[-110]_{Pna2_1}$// YSZ [100],
(f) GFO $(001)_{Pna2_1}$// YSZ (001), GFO $[-110]_{Pna2_1}$// YSZ [010].

The relationship between planes and directions normal to the planes is not as straightforward in the orthorhombic system as in the cubic system. For example, for GFO, the direction normal to the $(130)_{Pna2_1}$ planes is not the $[130]_{Pna2_1}$ direction, but the $[110]_{Pna2_1}$ direction.

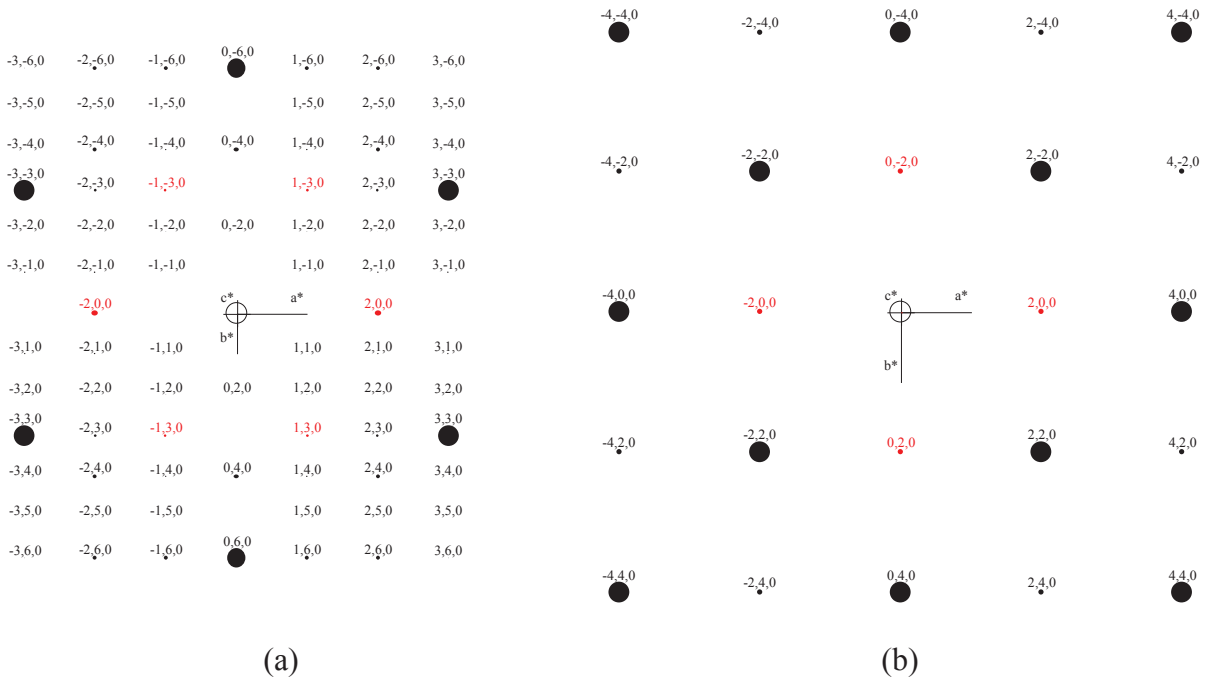

Figure 4-29. Reciprocal lattices of (a) GFO in the $[001]_{Pna2_1}$ zone axis, and (b) YSZ in the [001] zone axis. The possible matching distances are indicated on each lattice in red.

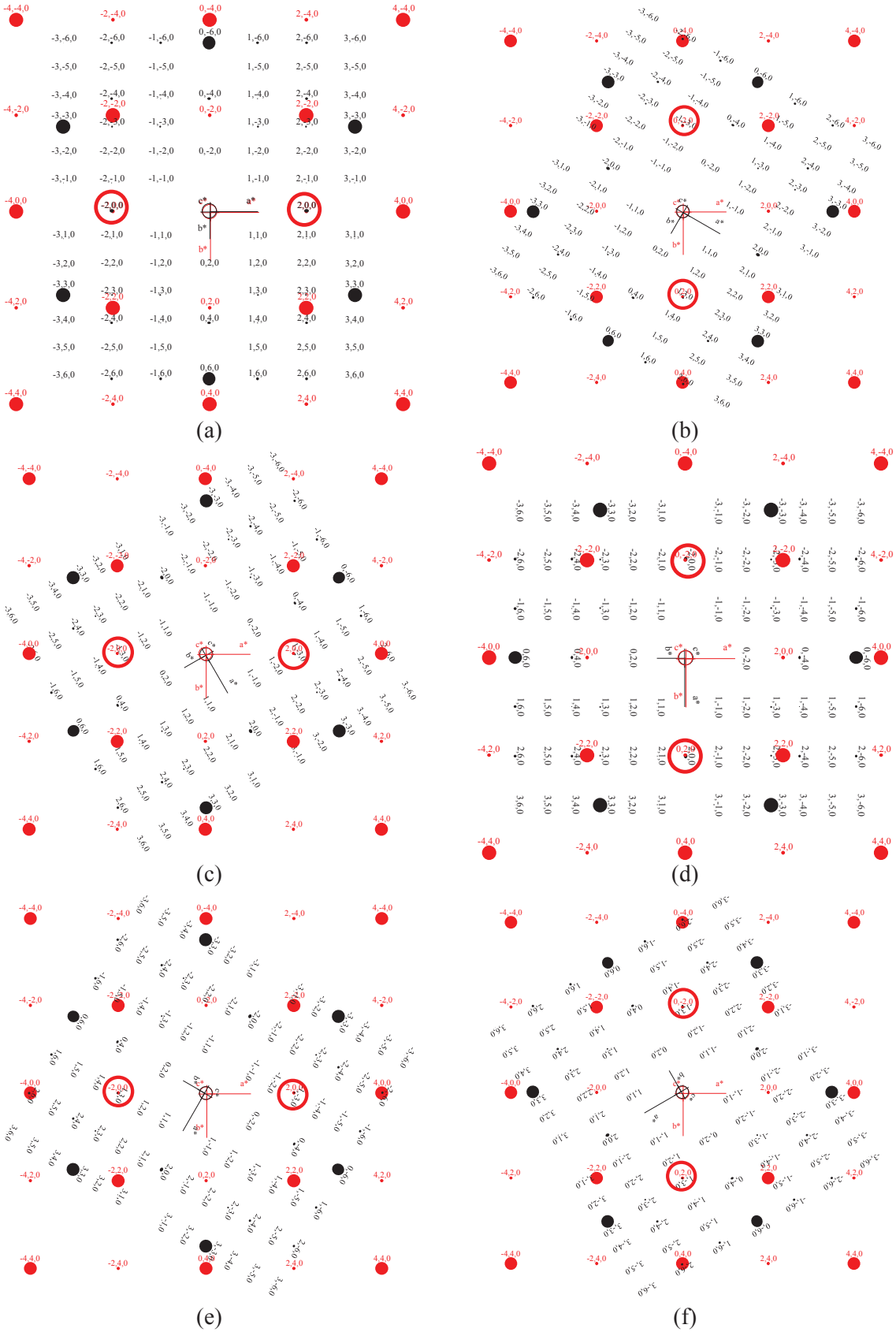

Figure 4-30. The six matching possibilities for the growth of GFO(001)$_{Pna2_1}$ onto YSZ(001). (the reciprocal lattice of GFO is in black, that of YSZ in red)

TEM cross sections images of GFO$(001)_{Pna2_1}$ thin films onto YSZ(001) which will show resolution in the substrate part will be taken in the YSZ<100> zone axes and will allow the simultaneous observation of the six variants (a) to (f). But, because of similarities between the reciprocal lattices of the $[110]_{Pna2_1}$,$[-110]_{Pna2_1}$, and $[100]_{Pna2_1}$ zone axes (Figure 4-31), on the one hand, and $[310]_{Pna2_1}$, $[310]_{Pna2_1}$and $[010]_{Pna2_1}$ zone axes on the other hand, only two contrasts have been observed in the GFO layer (*Table 4-5*).

Table 4-5. Crystallographic orientations of the two different contrasts which may be observed on TEM images for the GFO phase

	YSZ zone axes	GFO zone axes
TEM contrast 1	<100>	$[010]_{Pna2_1}$ $[310]_{Pna2_1}$ $[-310]_{Pna2_1}$
TEM contrast 2	<100>	$[100]_{Pna2_1}$ $[110]_{Pna2_1}$ $[-110]_{Pna2_1}$

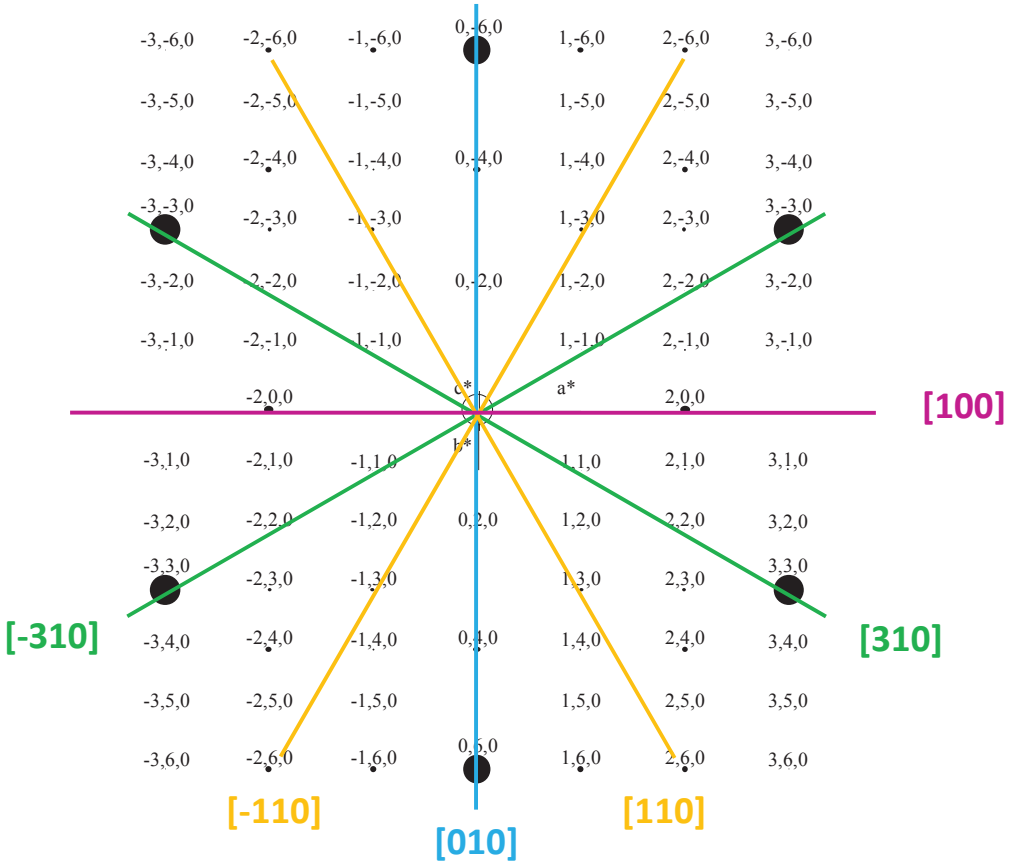

Figure 4-31. The six different zone axes available for observation of GFO thin films in cross views

Figure 4-32 shows a TEM image of a pure GFO1.4 thin film on YSZ(001) in cross view. The growth is columnar with columns of *ca.* 10-15 nm wide. Two different contrasts are visible on the image in zones 1 and 2. The FFT of Zone 1 indicates that GFO is in either the $[110]_{Pna2_1}$ or $[100]_{Pna2_1}$, (TEM contrast 2) while the FFT of Zone 2 indicates it is in either the $[310]_{Pna2_1}$ or $[010]_{Pna2_1}$ zone axes (TEM contrast 1).

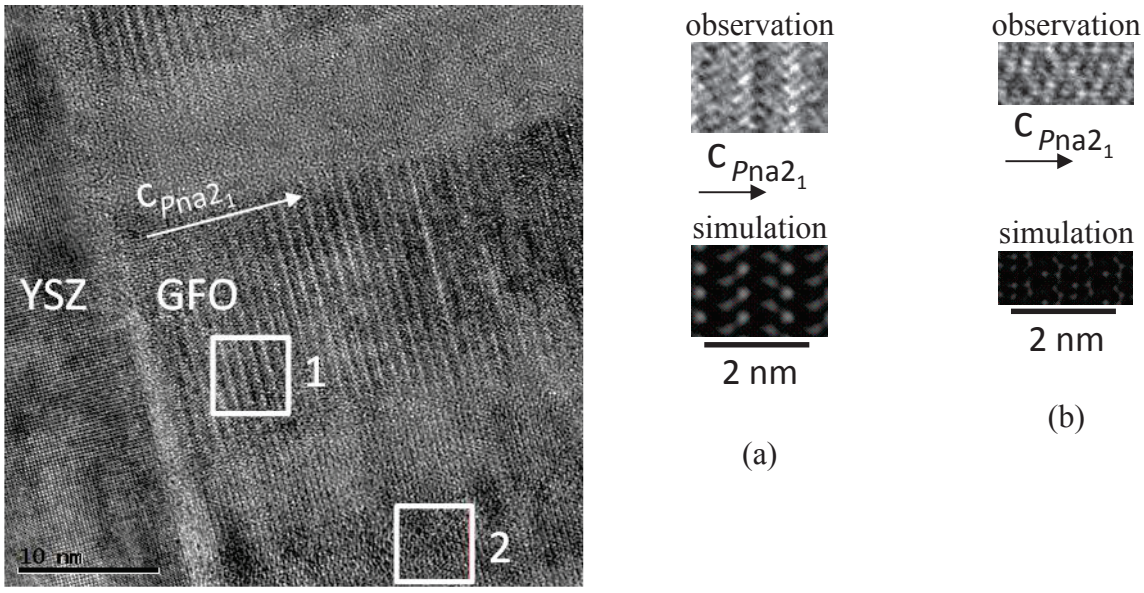

Figure 4-32. TEM cross view image of an undoped GFO1.4 thin film deposited on YSZ(001)

Further analysis of the zones through FFT are shown on the Figure 4-33.

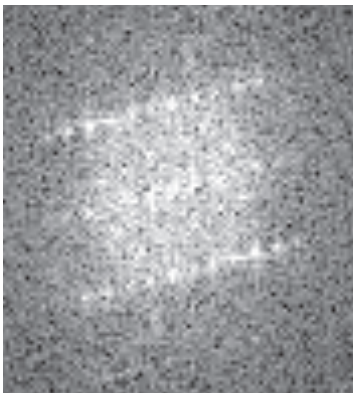

FFT of zone 1

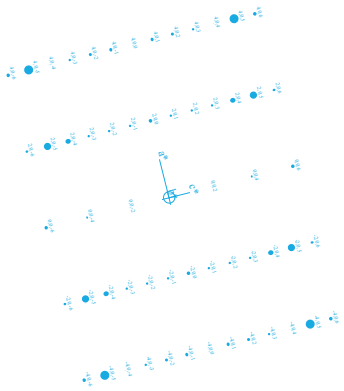

GFO reciprocal lattice in the $[010]_{Pna2_1}$ zone axis

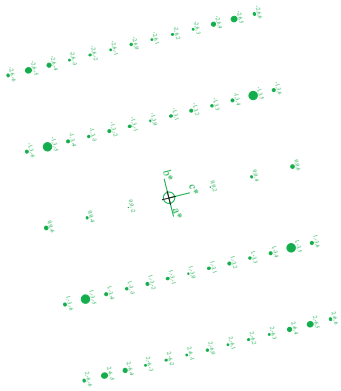

GFO reciprocal lattice in the $[310]_{Pna2_1}$ zone axis

(a)

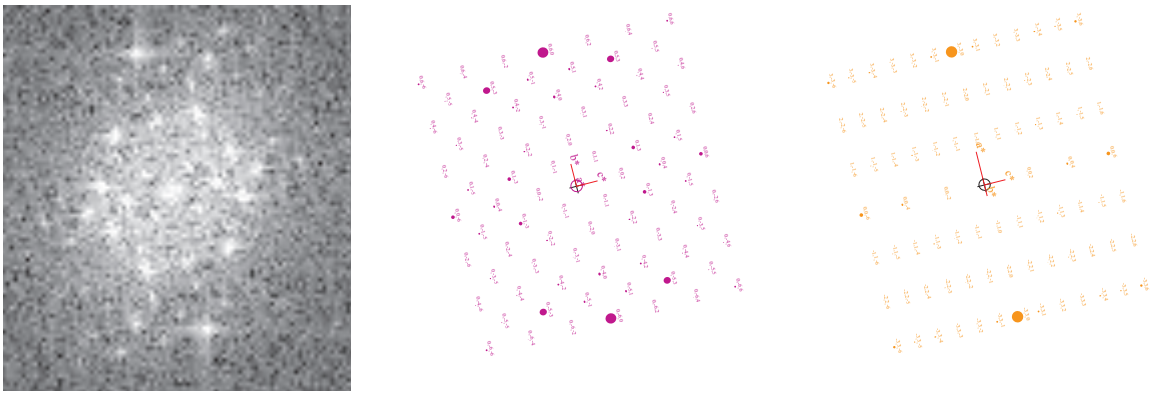

FFT of Zone 2

GFO reciprocal lattice in the $[100]_{Pna2_1}$ zone axis

GFO reciprocal lattice in the $[110]_{Pna2_1}$ zone axis

(b)

Figure 4-33. FFT of Zones (a) 1 and (b) 2 of the TEM cross view image of GFO1.4 on YSZ(001) thin film presented in Figure 4-32.

The TEM observations of Ni-doped GFO samples deposited onto YSZ(001) do not show any interfacial layer presenting a contrast different from the rest of the layer, as it was the case for the Ni-doped GFO deposited onto STO:Nb(111) (Figure 4-34). However, when doing FFT of zones which are intermediate between grains of different contrasts (Figure 4-35), one can see additional spots corresponding to distances typical of the spinel-like phase (Figure 4-35).

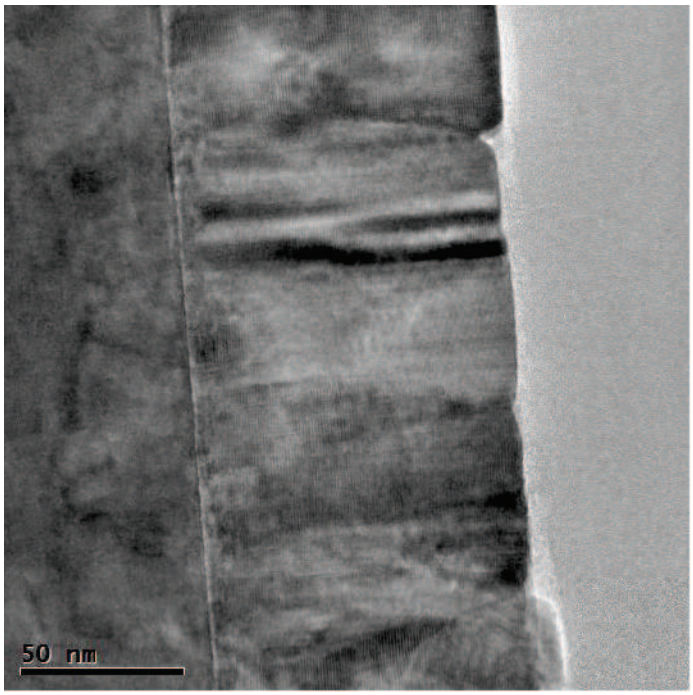

Figure 4-34. TEM cross view image of a 3%-Ni-doped GFO thin film deposited onto YSZ(001) (sample prepared by FIB)

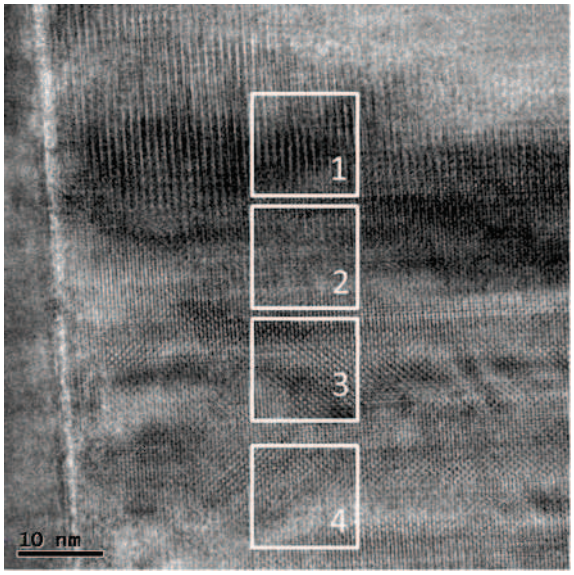

a) zones between grains, bright field image

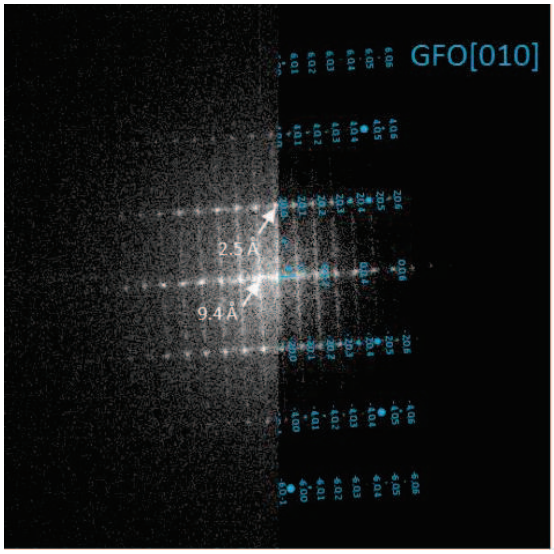

(b)

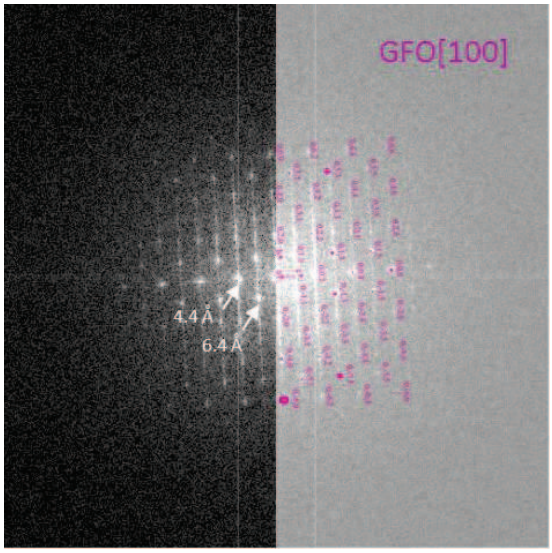

(c)

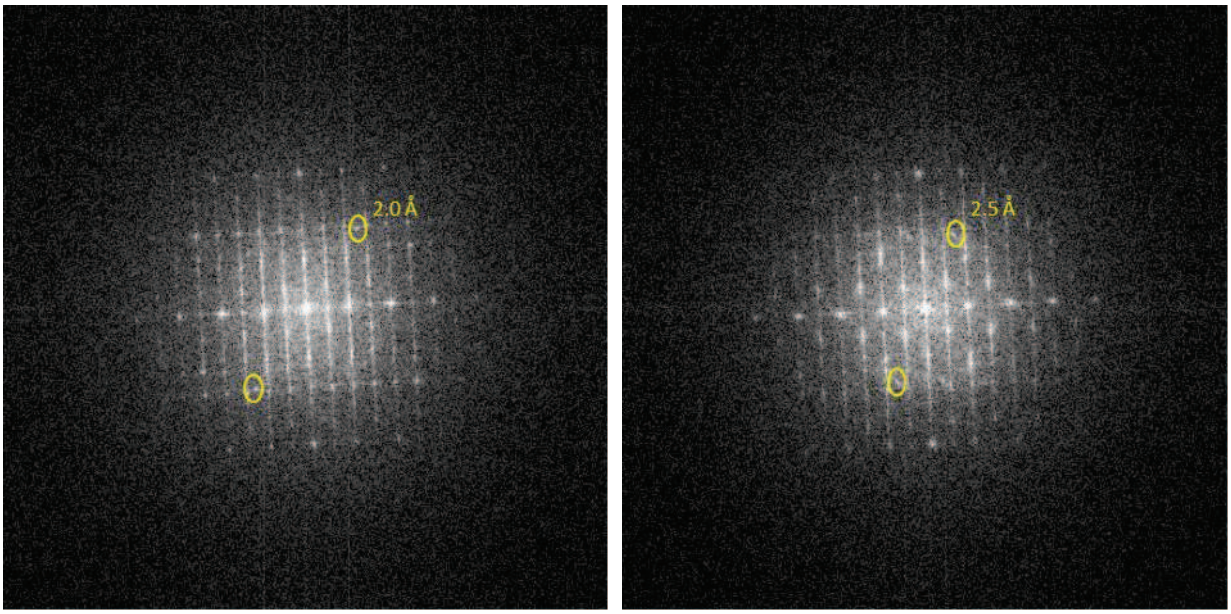

(d) (e)

Figure 4-35. (a) Same image as in Figure 4-32 with higher magnification, (b) and (c) FFT of parts of the image taken within one grain, in zones (1) and (3), respectively, and (d) and (e) FFT of parts of the image taken in zones intermediate between two grains (2) and (4), respectively. Zone (1) corresponds to a TEM contrast 1, and Zone (3) to a TEM contrast 2. In both intermediate zones, one can spot extra dots (yellow) corresponding to either d_{400}=2.0Å or d_{311}=2.5 Å of the spinel-like phase.

Indeed, when indexing the electronic diffraction patterns of wide zones of Ni-doped thin films, one does see the fingerprint of this phase (Figure 4-36). The dots within the dotted yellow circles in Figure 4-36 correspond to a distance d=2.0 Å, which may be assigned to the (400) planes of a spinel-like phase, when observed in its [110] zone axis. The <111> direction of the spinel-like phase will be along the growth axis, for it is the direction of the oxygen stacking. In the [110] zone axis, there are two possible directions for the <111> direction. Figure 4-36 (b) shows each of the possibilities in the left (1) and right (2) part of the image. Both are necessary to account for the four d=2.0 Å dots observed. The dots within the full line circles correspond to a distance d=2.5 Å, which may be assigned to the (311) planes of the spinel-like phase, when observed in its [112] zone axis. Figure 4-36 (c) shows the matching between the reciprocal space lattice of the spinel-like phase in this zone axis and the observed diffraction pattern.

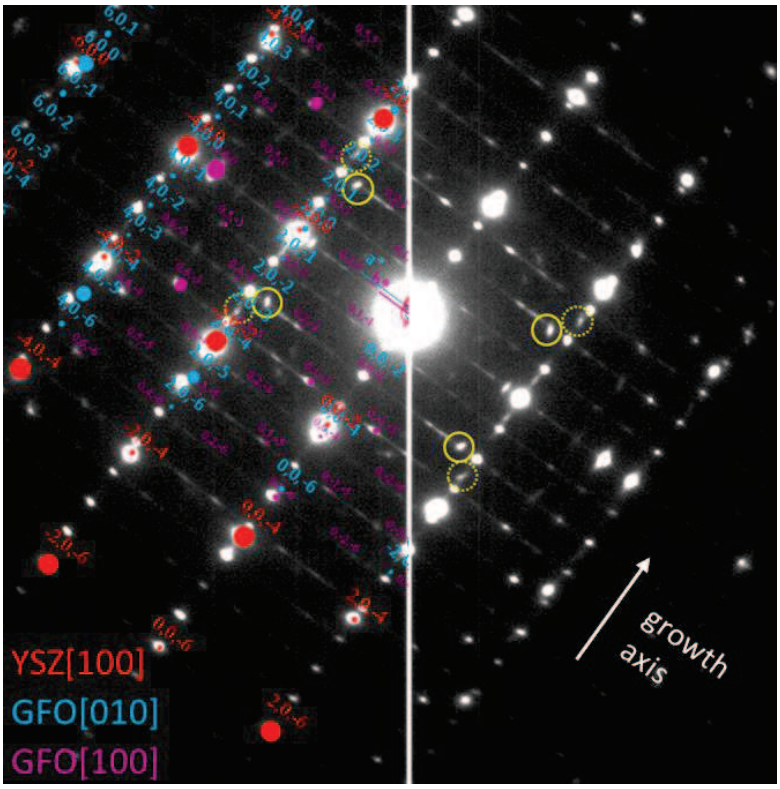

(a)

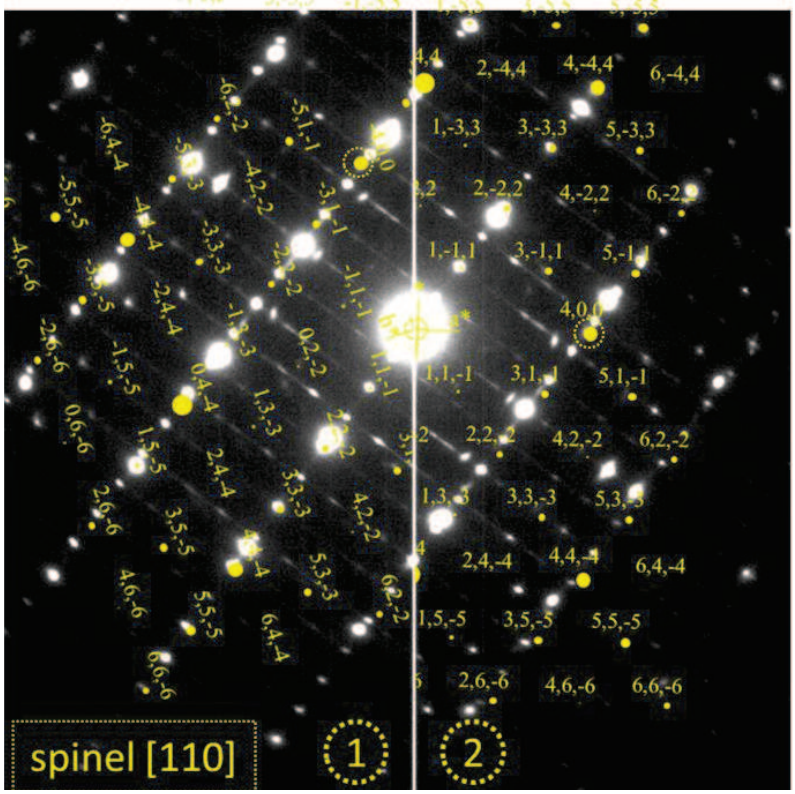

(b)

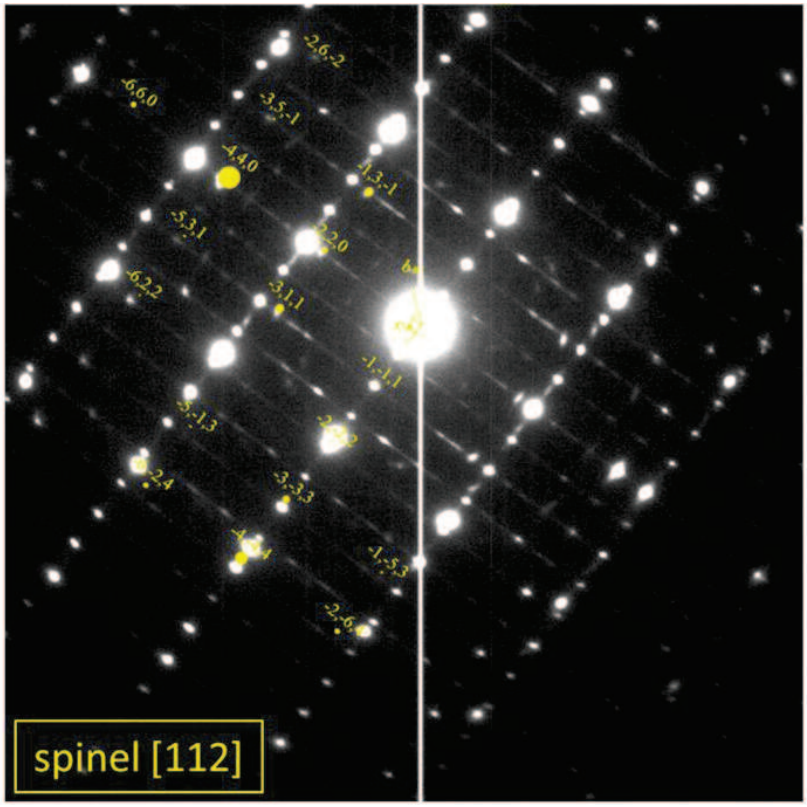

(c)

Figure 4-36. Electronic diffraction pattern of the 3% Ni-doped GFO thin film deposited on YSZ(001). It can be indexed with YSZ in its [100] zone axis and GFO in both its $[010]_{Pna2_1}$ and $[100]_{Pna2_1}$ zone axes (all variants may be observed on a cross view of GFO deposited onto YSZ(001). Additional spots are however observed, with distances of 2.0 and 2.5 Å, (dotted and full line yellow rings, respectively). These distances may be accounted for when considering a spinel-like phase (a≈8.3Å) in its [110] (b) and [112] (c) zone axes, respectively. In the [110] zone axis, two orientations are possible and shown in (b).

The epitaxial relationships observed on the TEM images of films deposited onto YSZ(001) substrates is summarized in *Table 4-6*. When analyzing the matching possibilities of the spinel-like phase with the YSZ substrate and the GFO layer (Figure 4-37), one notices that no matching can be found between YSZ(001) and the spinel-like phase (111). The observation of a [111] oriented growth of the spinel-like phase, and not of a randomly oriented one, cannot therefore be due to the substrate, but is rather in relationship with the GFO phase. This is probably the reason why, in contrast to what was observed in the case of a growth onto STO:Nb(111), no interfacial layer of spinel-like phase is observed between the substrate and the GFO layer. Here the spinel-like phase is distributed over the entire thickness of the films, located in between grains, probably promoted by stacking faults.

Table 4-6. Crystallographic orientations of the two different contrasts which may be observed on TEM images for a growth onto YSZ(001) substrates

	YSZ zone axes	GFO zone axes	Spinel-like phase zone axes
TEM contrast 1	<100>	$[010]_{Pna2_1}$ $[310]_{Pna2_1}$ $[-310]_{Pna2_1}$	<110>
TEM contrast 2	<100>	$[100]_{Pna2_1}$ $[110]_{Pna2_1}$ $[-110]_{Pna2_1}$	<112>

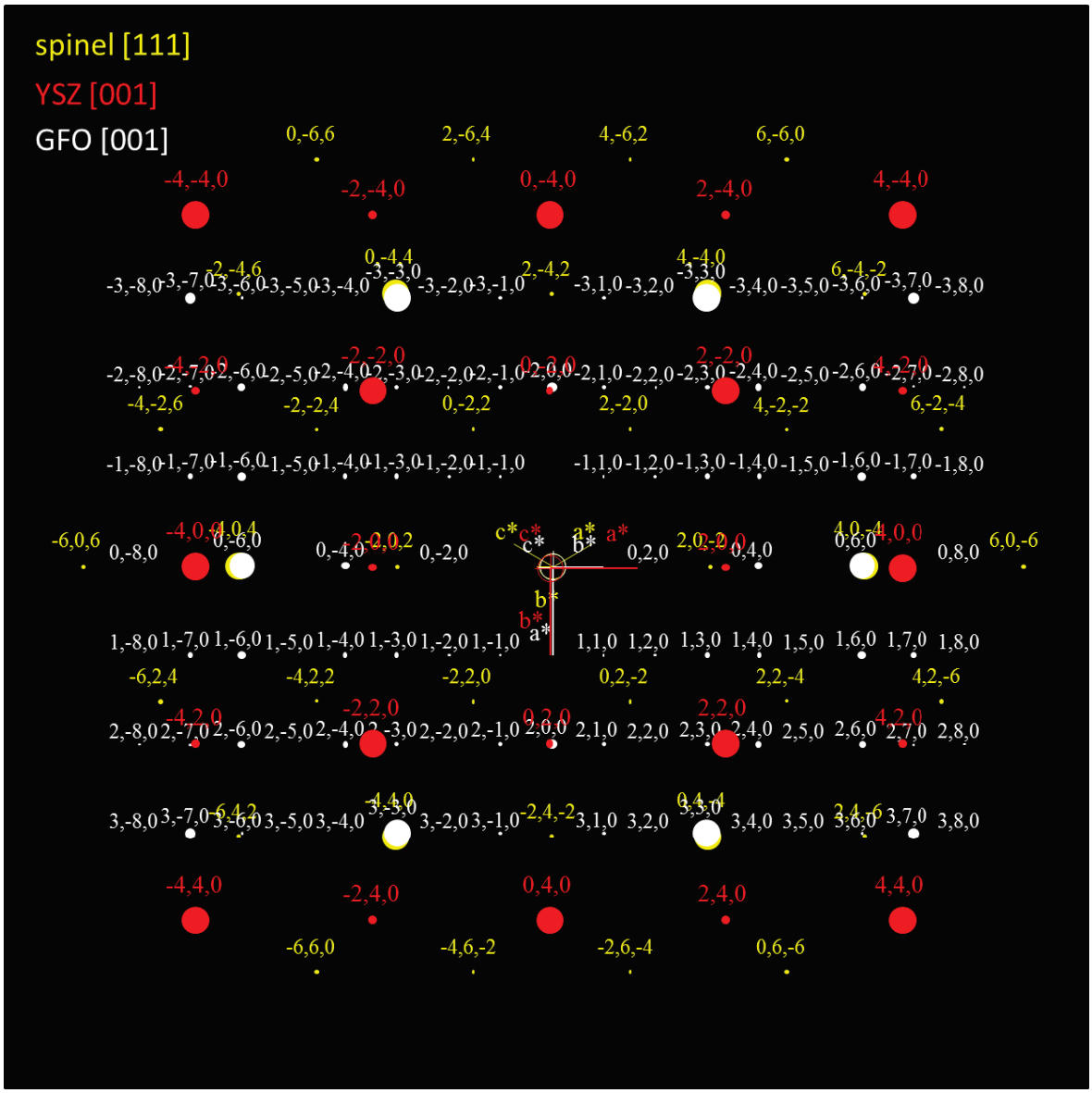

Figure 4-37. Reciprocal lattices of the YSZ substrate, GFO, and spinel-like phase in their [001], $[001]_{Pna2_1}$ and [111] zone axes, respectively, corresponding to the growth axis, showing the possible matchings for epitaxial growth.

As in case of the GFO thin film deposited on STO:Nb(111), the composition of the layer in case of YSZ(100) is homogeneous throughout the thickness, with Ga, Fe, and Ni contents in agreement with the expected values for x% Ni-doped GFO1.4, *i.e.* $Ga_{0.6}Fe_{1.4-2x}Ni_{2x}$. Figure 4-38 shows an EDX analysis in STEM HAADF mode of the cross view of a 3% Ni-doped GFO film as an example.

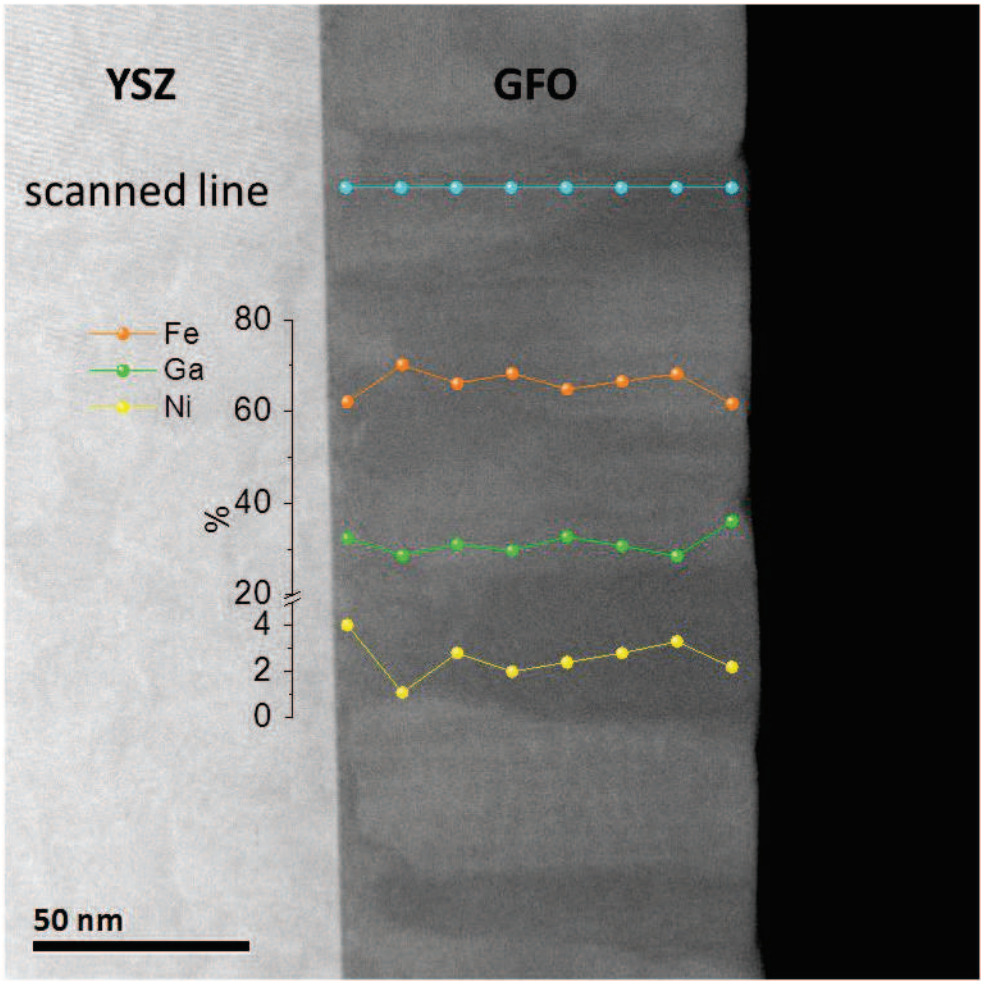

Figure 4-38. Cross view composition of the 3% Ni-doped GFO thin film deposited on YSZ(001), determined from EDX analysis in STEM HAADF mode.

The cell parameters were calculated from reciprocal space mappings of the (062) $_{Pc21n}$ and (570)$_{Pc21n}$ reflections. As observed for the film grown onto STO:Nb(111) substrate, the in-plane a and c parameters are lower than observed for the same Fe/Ga ratio in bulk[15], the out-of-plane b parameter is higher (Figure 4-39).

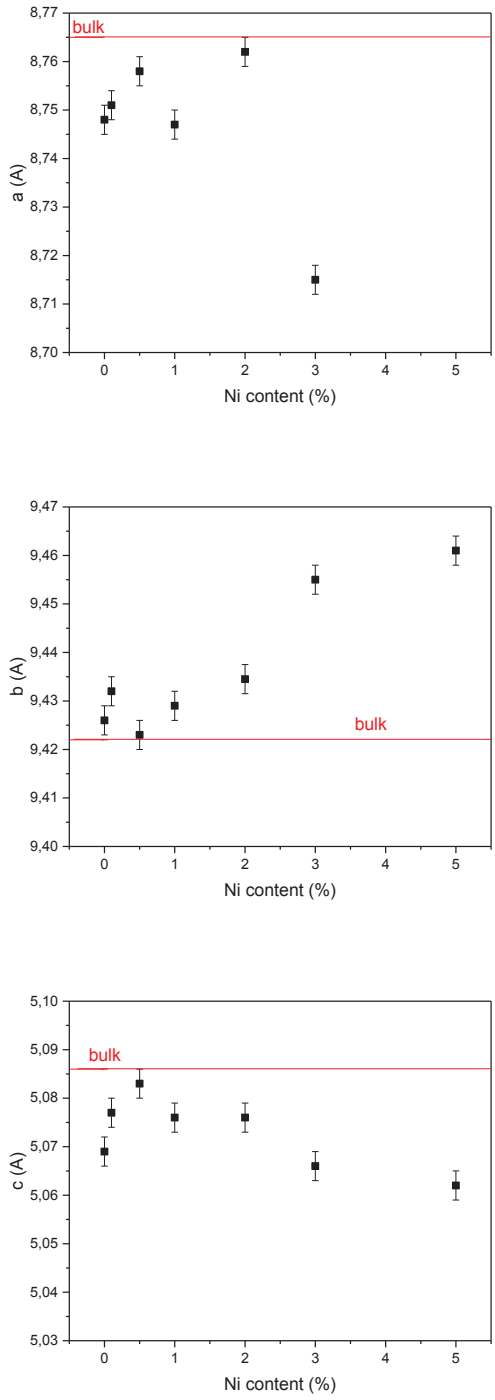

Figure 4-39. Evolution of cell parameters with increase of Ni doping in thin films deposited on YSZ(100).

As in the case of the GFO:Ni thin films deposited on STO:Nb(111), the mismatch between YSZ(100) and GFO(010) along the YSZ[010]//GFO[001] direction cannot account for the low c parameters observed. Indeed a_{YSZ}=5.139 Å is higher than 5.086(2) Å, observed for c in bulk $Ga_{0.6}Fe_{1.4}O_3$ and would therefore impose a tensile stress rather than a compressive one. The different thermal expansion coefficients between the substrate and the layer cannot account for the smaller in-plane parameters observed for GFO thin films either. The samples are deposited at 800°C and then cooled down to room temperature. One could therefore expect a matching of c_{GFO} onto a_{YSZ} at 800°C. The thermal expansion coefficient of YSZ being $\alpha_{YSZ}=9.10^{-6}$ /K [16] whereas its cell parameter at 800°C is 5.151 Å. Assuming a_{GFO} adopts this value when deposited, upon cooling, considering a thermal volume expansion coefficient of $\alpha_{GFO}=2.6.10^{-5}$ /K,[17] it would become, if one considers that this thermal coefficient is isotropic, $a_{GFO\,RT} = a_{GFO\,800°C} * (1 + \frac{\alpha_{GFO}}{3} * \Delta T) = 5.151(1 + 8.67.10^{-6} * (20 - 800)) = 5.12$ Å. This value is higher than the experimentally observed one, even for undoped samples. Moreover, x-ray diffraction of the rsm GFO nodes $(2010)_{Pna21}$ and YSZ(206) show that the layer is fully relaxed (Figure 4-40).

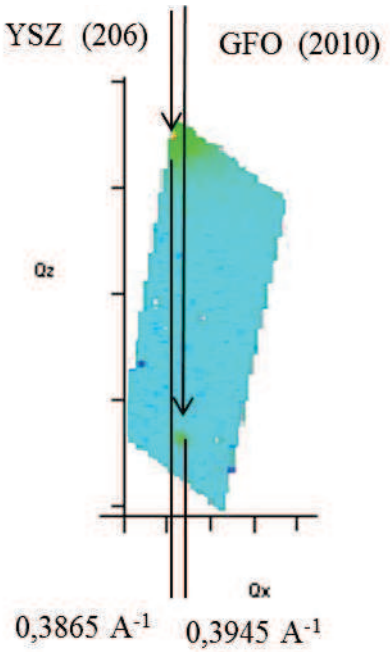

Figure 4-40. RSM maps for nodes of substrate YSZ(206) and GFO (2010) $_{Pna21}$.

The elongation of the GFO cell along its b axis is therefore more likely to be related to the existence of oxygen vacancies within the material. Some increase in the cell parameters have already been observed in materials like perovskites and explained by the oxygen vacancies resulting in the partial reduction of some of the cations, which having more

electrons in their reduced form, have a bigger radius. The cell parameters which have the closest values to those observed for the bulk are obtained for the 0.5-2% Ni doping.

The insertion of the Ni atoms within the crystallographic structure of GFO was checked by means of resonant diffraction at the Ni K edge. Three independent Bragg reflections of the GFO structure, (110), (211), and (510), were scanned. An anomalous signal could be observed in all cases (Figure 4-41). It originates from a modification of the diffracted intensity due to absorption processes involving interactions between the x-ray beam and the Ni atoms in the sample and is a proof that Ni atoms contribute to the structure factor for this crystallographic reflection. It is therefore an unequivocal proof of the insertion of the Ni atoms within the GFO crystallographic structure.

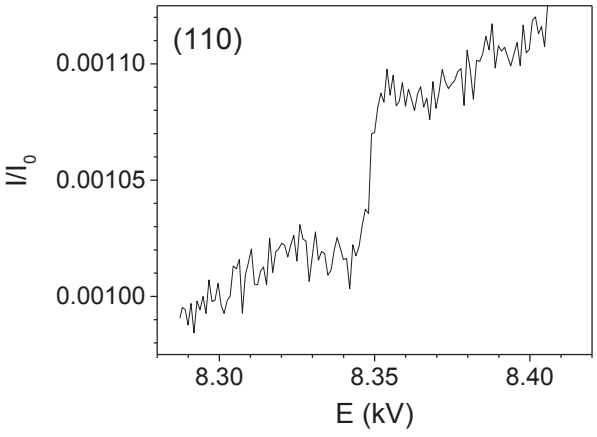

(a)

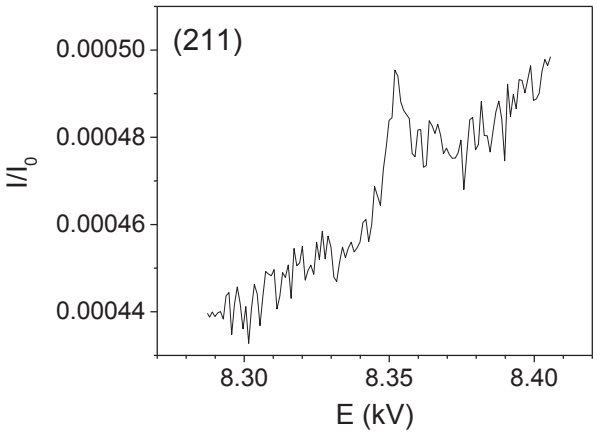

(b)

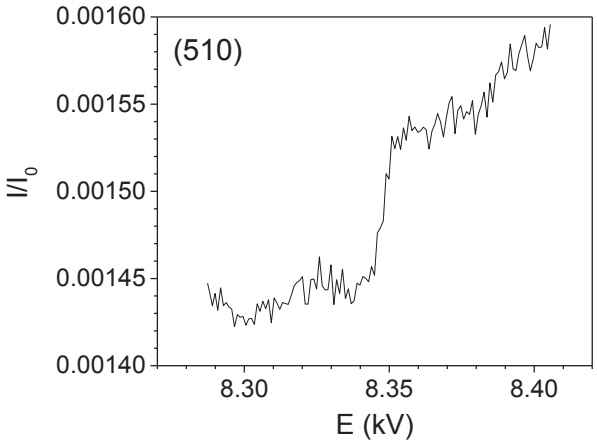

(c)

Figure 4-41. Intensity variations of the (a) (110), (b) (211), and (c) (510) reflections at the Ni K edge

3.3.2 Magnetic properties

The Neel temperature of the GFO films was measured as the inflexion point of the field-cooled magnetization curve measured in a 50 Oe magnetic field (Figure 4-42). It riches a maximum for the 2% Ni content (Figure 4-43). The magnetic properties in GFO are governed by the superexchange interactions between neighboring magnetic ions. They will therefore be strongly affected by the M−O−M bond angles, where M is a magnetic cation, and by the cationic ordering. In addition to the cationic site distribution, the distortion of the polyhedra also plays an important role. The 2 % Ni-doped sample is among those for which the cell is the less distorted when compared to bulk (Figure 4-44). The maximum in the Néel temperature is therefore probably due to a maximum in the orbitals overlapping. For lower doping, the cell is distorted by the presence of oxygen vacancies inducing the presence of Fe^{2+} ($rFe^{2+}_{(VI)}$= 78 pm, $rFe^{3+}_{(VI)}$= 64 pm).

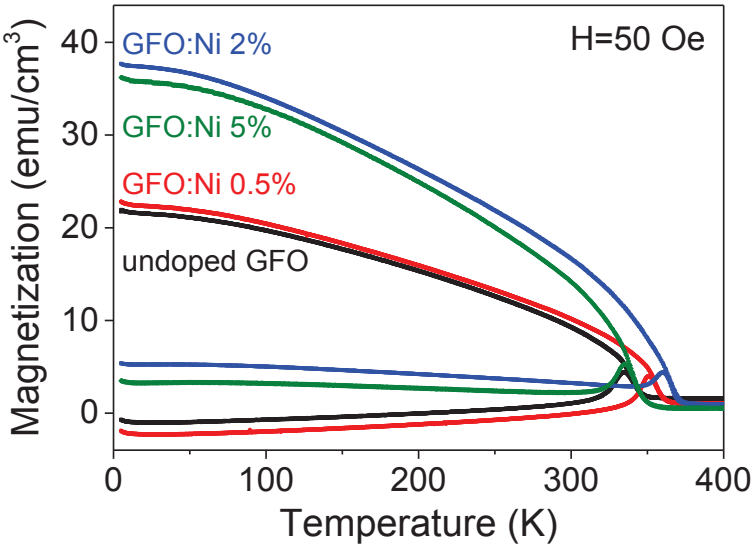

Figure 4-42. Zero field cooled and field-cooled magnetization curves of the doped and undoped GFO thin films, measured in a 50 Oe magnetic field applied parallel to the films

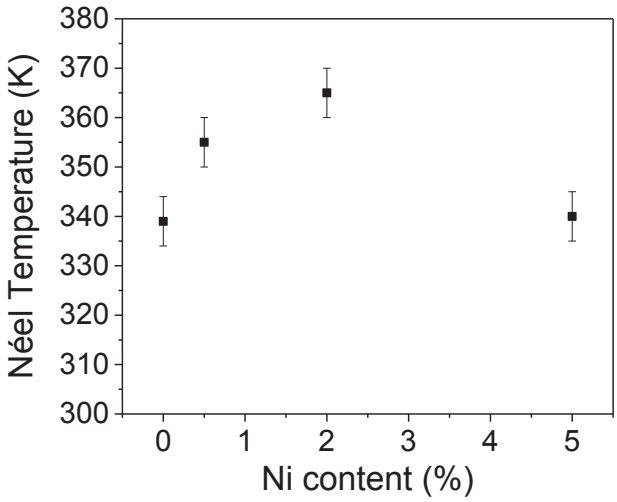

Figure 4-43. Evolution of the Néel temperature of the Ni-doped GFO films with the Ni content

Hysteresis curves measured at 300 K (Figure 4-44) indicate that the samples are more easily magnetized within the plane of the films (*ac* plane) than out of plane (*b* direction).

GFO :Ni 0%

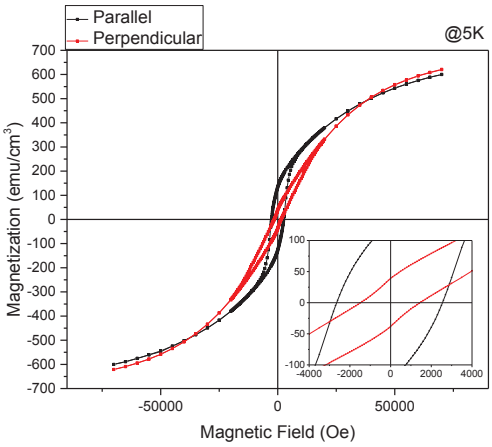

a)

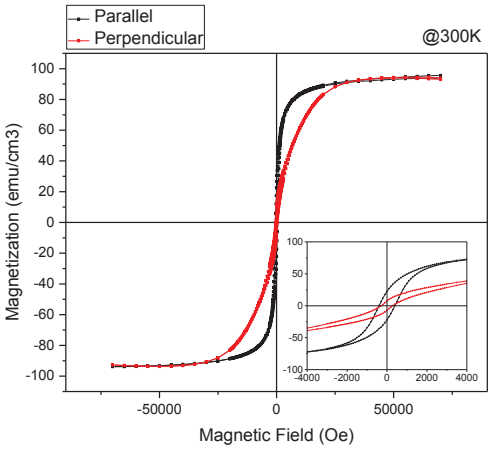

b)

GFO :Ni 0.1%

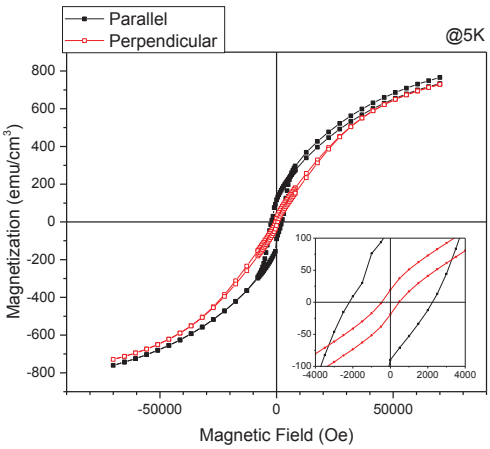

c)

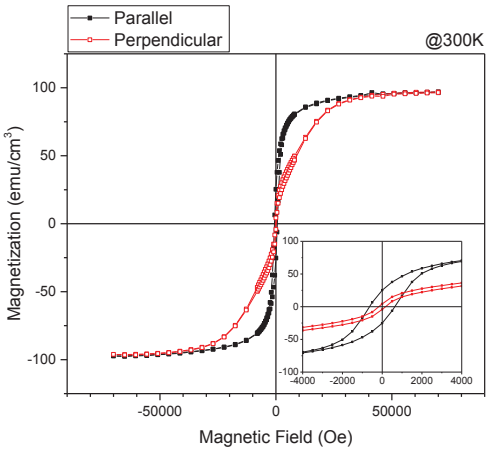

d)

GFO :Ni 0.5%

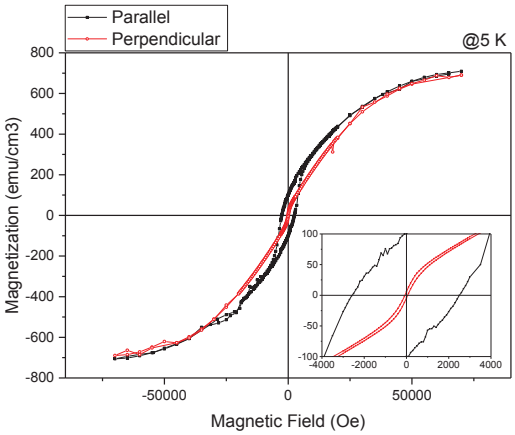

e)

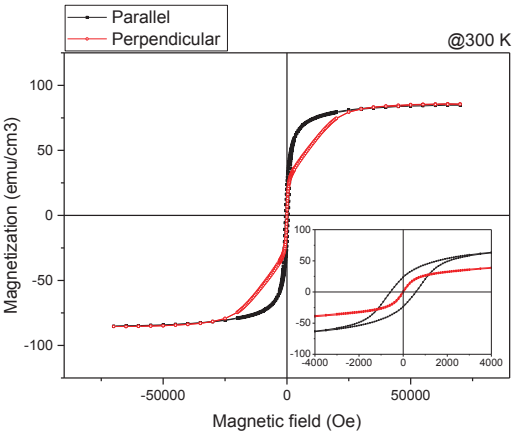

f)

GFO :Ni 1%

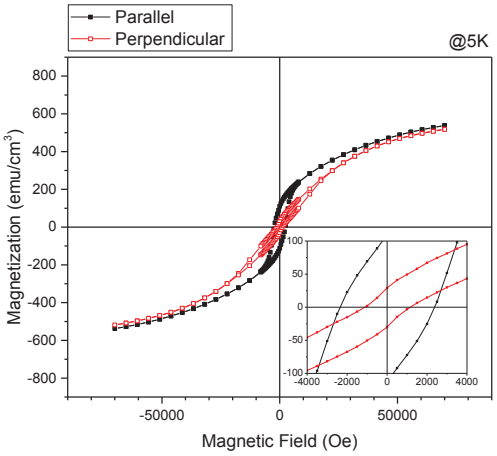

g)

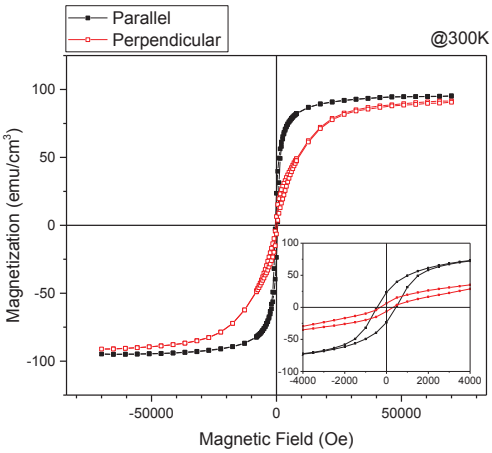

h)

GFO :Ni 2%

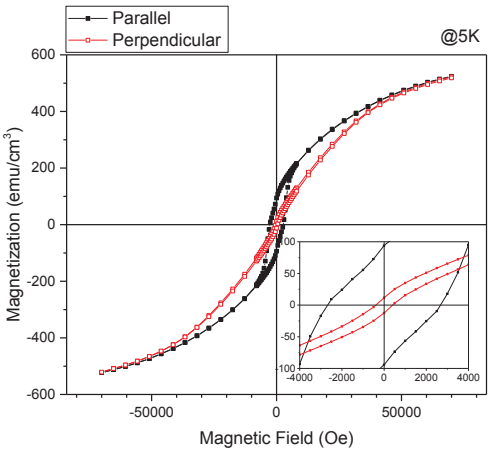

i)

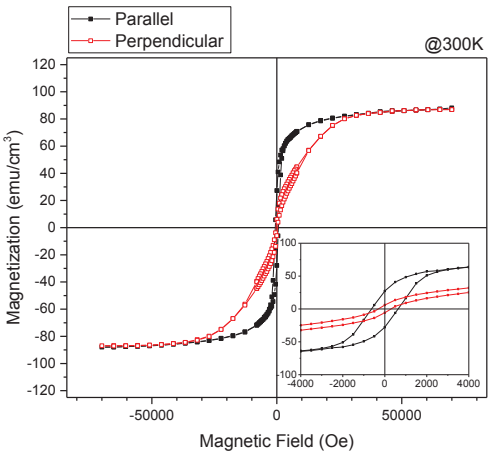

j)

GFO :Ni 3%

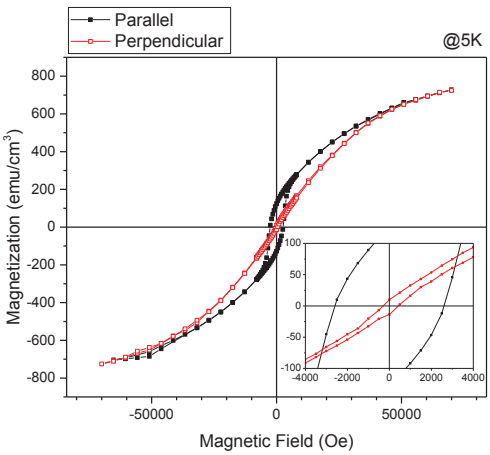

k)

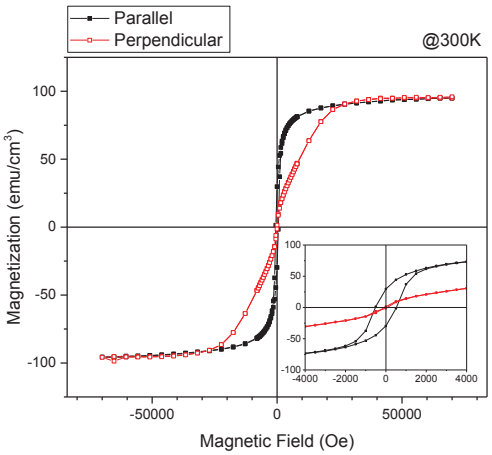

l)

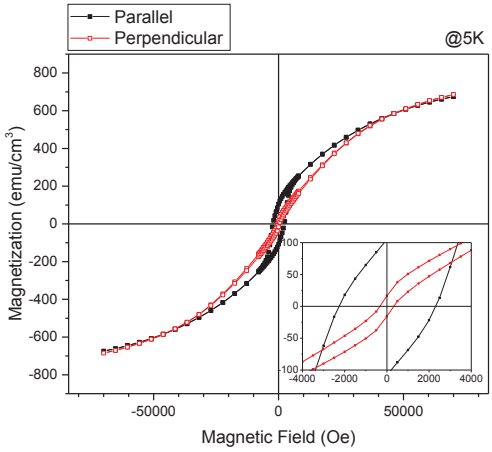

m)

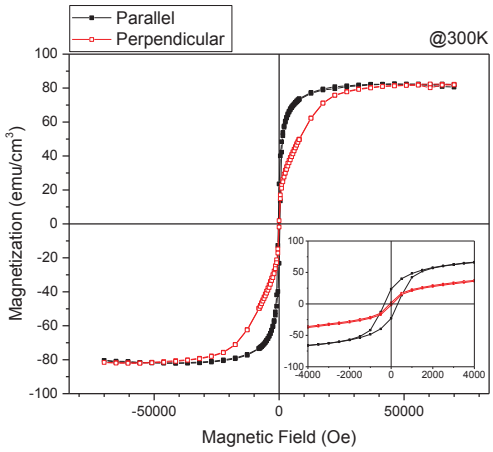

n)

Figure 4-44. Hysteresis loops of the (a,b) undoped, and Ni (c,d) 0.1% (e,f) 0.5%, (g,h) 1%, (i, j) 2%, (k, l) 3% and (m, n) 5% doped GFO thin films, measured at 5K and 300 K in parallel (filled black squares) and perpendicular (red hollow squares).

This is consistent with the easy and hard magnetization axes observed in bulk: c is the easy axis while b is the hard axis. Some exchange bias may be observed on the hysteresis loops measured at 5 K. But their low value is within the error bar of ±30 Oe. No exchange bias is observed at 300K (*Table 4-7*).

Table 4-7. Coercive fields and exchange bias observed for GFO:Ni thin films at 5K.

	Parallel measurements		Perpendicular measurements	
Ni %	Hc (Oe)	Exchange bias (Oe)	Hc (Oe)	Exchange bias (Oe)
0	2727	-46	1400	-29
0.1	2212	35	520	0
0.5	2542	-26	65	0
1	2363	-9	1290	0
2	2670	0	400	0
3	2593	-5	380	0
5	2279	22	360	0

3.3.3 Electrical properties

The electric characterizations of GFO:Ni samples deposited on non-conducting YSZ(100) substrates were performed in plane by Yue Chang, Ekaterina Chikoidze and Yves Dumont in GEMaC-CNRS, Versailles.

Figure 4-45 shows the temperature dependence of resistivity for Ni-doped GFO thin films in the 300-500 K temperature range. The resistivity of the films increases with decreasing temperature, indicating a semiconducting behavior of the electronic conductivity. Room temperature resistivity (ρ) values and conductivity activation energy values (Ea) for different Ni contents, as determined from the slope of ln(1/ρ) versus 1/T, are summarized in *Table 4-8*. Room temperature resistivity values vary between 5.5 x 10^3 and 7.1 x 10^4 Ω.cm. The maximum value is obtained for the 2% Ni-doping. The value of the conductivity activation energy in the undoped GFO sample is of 0.28 eV and remains practically unchanged for all Ni contents between 0 and 5%, confirming the hopping nature of conductivity for all samples.

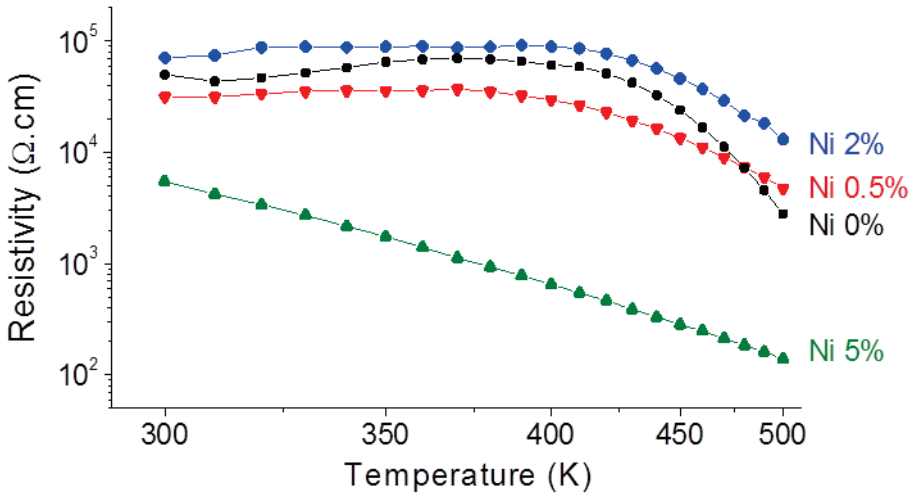

Figure 4-45. Temperature evolution of the resistivity of the films for various Ni content.

Table 4-8. Room temperature resistivity and conductivity activation energies for different Ni contents in the GFO films

	Resistivity (ρ, Ω.cm)		Conductivity activation energy
	300 K	500 K	(E_a, eV)
Undoped GFO	5.0×10^4	2.8×10^3	0.28
Ni:0.5%	3.2×10^4	4.8×10^3	0.30
Ni:2%	7.1×10^4	1.3×10^4	0.40
Ni:5%	5.5×10^3	1.4×10^2	0.23

Seebeck and Hall effects measurements allowed unambiguous determination of the nature of the carriers, and of their concentration (*Table 4-9*).

Table 4-9. Type, concentration, and mobility of the carriers at 300 and 500 K for different Ni contents in the GFO films

	Carriers concentration (cm^{-3})		Mobility (cm/V/s)	
	(p) : holes, (n) : electrons			
	300K	500K	300K	500K
Undoped GFO	N/A	(n) 2.80×10^{16}	N/A	0.10
Ni:0.5%	N/A	(n) 1.20×10^{15}	N/A	0.99
Ni:2%	N/A	(p) 3.60×10^{15}	N/A	0.20
Ni:5%	(p) 1.2×10^{15}	(p) 1.04×10^{17}	0.71	0.41

The nature of the carriers varies with the Ni content: for doping contents below 2 %, the carriers are electrons, while for Ni contents higher than 2 %, they are holes. The number of carriers is minimum for Ni contents between 0.5 and 2 % (Figure 4-46). This confirms our assumption concerning the mechanism responsible for conduction in the films.

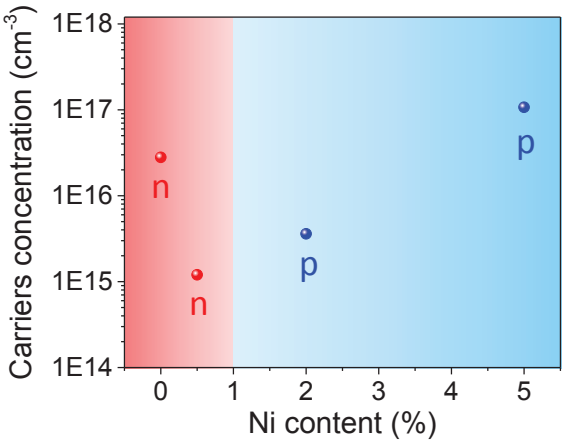

Figure 4-46. Evolution of the nature of the carriers and of their concentration with their Ni content in the GFO structure

The substitution of Fe with Ni indeed leads to the creation of holes according to

$m\,NiO \rightarrow m\left(Ni'_{Fe} + h^{\bullet} + \frac{1}{2}O_2\right)$, where Ni'_{Fe} stands for Ni in the Fe site with an apparent negative charge and $h^{\bullet}$ represents a hole. These holes can be recombined with electrons according to : $e^{-} + h^{\bullet} \rightarrow 0$. The substitution of Fe with Ni therefore first leads to a decrease of the leakage currents thanks to the electrons-holes recombination mechanism. When the substituted Ni content m is too high when compared to the number of oxygen vacancies δ, supernumerary holes are eventually created and the materials becomes a p-type conductor. Since each oxygen vacancy generates 2 electrons, this is the case when $m > 2\,\delta$.

4. Conclusion to the chapter

We have observed the evolution of structural, electric and magnetic properties of thin films of a ferrimagnetic oxide, $Ga_{0.6}Fe_{1.4}O_3$, upon Ni^{2+} doping, for Ni contents up to 5% on different substrates: Pt buffered YSZ(111), STO:Nb(111) and YSZ(100). In case of Pt buffered YSZ(111), it wasn't possible to obtain a parasitic free GFO films. In case of depositions on other substrates, it was possible to insert into the structure up to 5 % of Ni without detecting any parasitic phase in θ-2θ mode by XRD.

Some spinel-like phase is observed in the TEM images of the GFO films, for depositions on both STO:Nb(111) and YSZ(001) substrates, in a much more pronounced way for Ni-doped films. Its growth is perfectly oriented along its [111] direction and it even shows perfect epitaxial relationships with the GFO phase. The cell parameter of this spinel-

like phase is such that most of its interplanar distances are fully compatible with those of the GFO phase. This may explain why this extra phase was never detected in θ–2θ x-ray diffraction patterns. The localization of this spinel-like phase is different for the two types of substrates: at the interfacial zone between the substrate and the GFO layer for STO:Nb(111) and in between grains, throughout the entire layer, for YSZ(001). This difference in the localization can be explained by the fact that while there is a perfect matching between the (111) plane of the spinel-like phase and STO:Nb(111), no matching can be found between spinel-like phase (111) and YSZ(001). The spinel phase, whose formation is probably chemically driven by the presence of the bivalent cations Fe^{2+} and Ni^{2+}, cannot grow directly on the YSZ substrate and rather grows from the existing GFO grains, taking advantage of the stacking faults existing at the grain boundaries. It has to be recalled that the spinel-like phase only differs from the GFO phase in the ordering of its oxygen stacking, ABCABC for the spinel-like phase, instead of ABAC for GFO. The spinel-like structure is however probably preferred for materials containing bivalent cations, such as Fe^{2+} and Ni^{2+}, as it is the case in spinels. It has been shown that the presence of Ni^{2+} stabilized the spinel structure.

The study performed on the samples deposited onto YSZ(100) demonstrate that the 2 % Ni doping is clearly a particular value as the insertion of 2 % Ni shifts the cell parameters of GFO thin films towards the values observed for bulk, while they are different for Ni contents below and above this value. All the films are ferrimagnetic with a net room temperature saturation magnetization between 65 and 90 emu/cm^3, for undoped and 5 % Ni doped GFO samples, respectively. The Néel temperature reaches a maximum for the 2 % Ni content, probably because its structure is the closest to the bulk one, allowing optimized orbital overlapping and superexchange interactions. A minimum conductivity was observed for the 2 % Ni-doped sample. The number of carriers and their mobilities were evaluated from Hall Effect. A conductivity type inversion, from n to p, is clearly evidenced when going from low to high doping contents. The semi-conducting behavior of room temperature ferrimagnetic Ni-doped $Ga_{0.6}Fe_{1.4}O_3$ epitaxial thin films, with tunable type of conductivity, paves the way towards new all oxide electronic devices.

Bibliography

[1] Lawes, G., Harris, A. B., Kimura, T., Rogado, N., Cava, R. J., Aharony, A., Entin-Wohlman, O., Yildirim, T., Kenzelmann, M., Broholm, C. and Ramirez, A. P., Physical Review Letters 95 (2005) 087205.
[2] Lawes, G. and Srinivasan, G., Journal Of Physics D-Applied Physics 44 (2011) 243001.
[3] Mohamed, M. B. and Fuess, H., Journal of Magnetism and Magnetic Materials 323 (2011) 2090.
[4] Mohamed, M. B., Hinterstein, M. and Fuess, H., Materials Letters 85 (2012) 102.
[5] Mohamed, M. B., Wang, H. and Fuess, H., Journal Of Physics D-Applied Physics 43 (2010) 455409.
[6] Lefevre, C., Shin, R. H., Lee, J. H., Oh, S. H., Roulland, F., Thomasson, A., Autissier, E., Meny, C., Jo, W. and Viart, N., Applied Physics Letters 100 (2012) 262904.
[7] Thomasson, A., Cherifi, S., Lefevre, C., Roulland, F., Gautier, B., Albertini, D., Meny, C. and Viart, N., Journal of Applied Physics 113 (2013) 214101.
[8] Shireen, A., Saha, R., Mandal, P., Sundaresan, A. and Rao, C. N. R., Journal of Materials Chemistry 21 (2011) 57.
[9] Thomasson, A. (2013). Ordres électriques et magnétiques dans le composé magnétoélectrique $GaFeO_3$: optimisation par dopage, Université de Strasbourg.
[10] Trassin, M., Viart, N., Ulhaq-Bouillet, C., Versini, G., Barre, S., Leuvrey, C. and Pourroy, G., Journal of Applied Physics 105 (2009) 6101.
[11] Mohamed, M. B., Senyshyn, A., Ehrenberg, H. and Fuess, H., Journal Of Alloys And Compounds 492 (2010) L20.
[12] Lefèvre, C., Roulland, F., Thomasson, A., Mény, C., Porcher, F., André, G. and Viart, N., The Journal of Physical Chemistry C 117 (2013) 14832.
[13] Whatmore, R. (2007). Ferroelectric Materials. Springer Handbook of Electronic and Photonic Materials. Kasap, S. and Capper, P., Springer US**:** 597.
[14] Trassin, M., Viart, N., Versini, G., Barre, S., Pourroy, G., Lee, J., Jo, W., Dumesnil, K., Dufour, C. and Robert, S., Journal of Materials Chemistry 19 (2009) 8876.
[15] Lefevre, C., Roulland, F., Thomasson, A., Meny, C., Porcher, F., Andre, G. and Viart, N., Journal of Physical Chemistry C 117 (2013) 14832.
[16] Valasek, J., Physical Review 17 (1921) 475.
[17] Gupta, M. K., Mittal, R., Zbiri, M., Singh, R., Rols, S., Schober, H. and Chaplot, S. L., Physical Review B 90 (2014) 134304.
[18] Levine, B. F., Nowlin, C. H. and Jones, R. V., Physical Review 174 (1968) 571.

CHAPTER 5

Optimization of the sputtering process for the elaboration of GFO thin films

Introduction

1. Optimization of the deposition parameters
   - 1.1 Optimizing the stoichiometry of the transfer
   - 1.2 Optimizing the films' roughness
   - 1.3 Optimizing thin films' crystallinity
   - 1.4 Magnetic properties of the film
   - 1.5 Structural study by TEM
2. Deposition of GFO on conducting electrodes
   - 2.1 Deposition on Pt buffered YSZ(111)
   - 2.2 Deposition on STO:Nb(111)
3. Deposition under an electric bias
   - 3.1 Deposition of GFO thin films on YSZ(100)
   - 3.2 Deposition of GFO thin films on STO:Nb(111)

Conclusion

Bibliography

1. Introduction

As described before, our group has optimized the deposition of GFO thin films by PLD and widely studied the properties of the material. Since GFO has been brought to thin film investigations, a numerous amount of techniques, both chemical and physical, have been focused on the deposition of GFO [1],[2]. Nevertheless, depositions of GFO thin films by sputtering are not mentioned until now in the literature. Sputtering is however a thin film deposition process at the core of today's semiconductors industries. Sputtering is also a technique that easily allows the application of positive or negative potential (V_p) during the film deposition. This may have an influence on the cell formation, resulting in possible distortion, which is always promising when studying ferroelectricity. Thus, it was interesting, first, to optimize the deposition by sputtering with a view to compare the properties of the obtained thin films with those obtained by PLD. And secondly, it was interesting to study the influence of a voltage bias applied to the substrate during deposition of the films on their structure and properties.

2. Optimization of the deposition parameters

2.1 Optimizing the stoichiometry of the transfer

An important issue in the sputtering process is the possible non-stoichiometric transfer of the elements from the target to the substrate.

The growth of the film on the substrate is happening due to sputtered atoms of material from the target on the magnetron. We noticed a variation in the composition of the deposited films which was influenced by the pre-sputtering time. An optimization of the stoichiometry of the transfer was performed doing depositions from a $Ga_{0,8}Fe_{1,2}O_3$ target (sintered ceramics of 7.5 cm diameter) onto YSZ(100) substrates in the radiofrequency mode. The structure of the GFO thin films strongly depend on the parameters of deposition: type of gas in the chamber, temperature, substrate, power applied on the target, etc… [3; 4]. The temperature was fixed to the highest allowed value of 700 °C. The power and the total pressure during deposition were 40 W and $1.6x10^{-8}$ mBar, respectively. The films were grown in a mixed Ar + O_2 atmosphere, where the argon flow rates were 20 sccm and the oxygen flow rates between 2 and 4 sccm. Depositions were performed after 2 different pre-sputtering times of 15 and 60 min.

Table 5-1 presents the results obtained for the composition of the films, as determined by EDX for the different experimental conditions. Figure 5-1 shows the variation of the Ga/Fe ratio measured on the films deposited with different pre-sputtering time. The expected value for the Ga/Fe ratio in a $Ga_{0,8}Fe_{1,2}O_3$ film is 0.67.

Table 5-1. Deposition conditions for the pre-sputtering time investigation.

Pre-sputtering, min	**Oxygen flux in the chamber, sccm**	**Composition**	**Ga\Fe**
15	4	$Ga_{0,71}Fe_{1,29}O_3$	0,55
60	4	$Ga_{0,8}Fe_{1,2}O_3$	0,67
60	2	$Ga_{0,77}Fe_{1,23}O_3$	0,63
60	2	$Ga_{0,79}Fe_{1,21}O_3$	0,65

The evolution of the Ga/Fe ratio with the pre-sputtering time is shown on Figure 5-1.

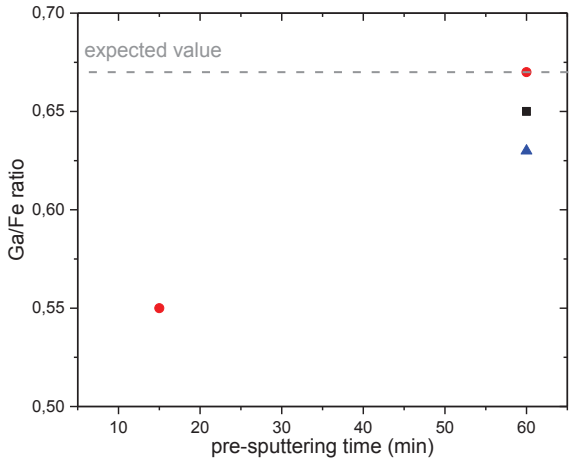

Figure 5-1. Evolution of the Ga/Fe ratio with the pre-sputtering time.

When sputtering a surface of a complex oxide target, the composition vapor which is formed strongly depends on the difference in weight between the species composing the target [5; 6].

As it is seen on Figure 5-1, in case of longer pre-sputtering time, the Ga/Fe ratio is close to the expected one. This is related to the presence of a surface layer of different composition which must be removed before the bulk target material can be sputtered [5; 6]. The vapor will first be richer in one of the components. The composition of the target will

thus be poorer in this component. The equilibrium composition will be reached when the equilibrium is done between the superficial composition of the target and the sputtering yield of the species.

Thus, we can conclude that to get a composition equal to the target one, a long time pre-sputtering must be done. One hour pre-sputtering time seems to be enough to get the equilibrium in the plasma and have a film of the composition of the target.

2.2 Optimizing the films' roughness

A surface study was done by SEM and AFM in order to investigate the influence of oxygen amount in the chamber during the deposition on the surface of the thin film. Figure 5-2 presents SEM images of the surface for layers deposited with 2 and 4 sccm O_2.

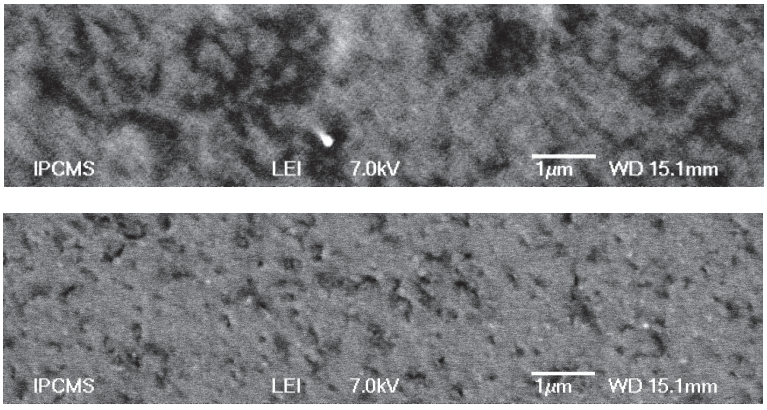

Figure 5-2. SEM images of the layers deposited with 20 sccm Ar and a) 2 sccm O_2 b) 4 sccm O_2.

In both cases the roughness seems high, but in case of higher amount of O_2 the quality improves. Same results were observed with AFM as shown on Figure 5-3.

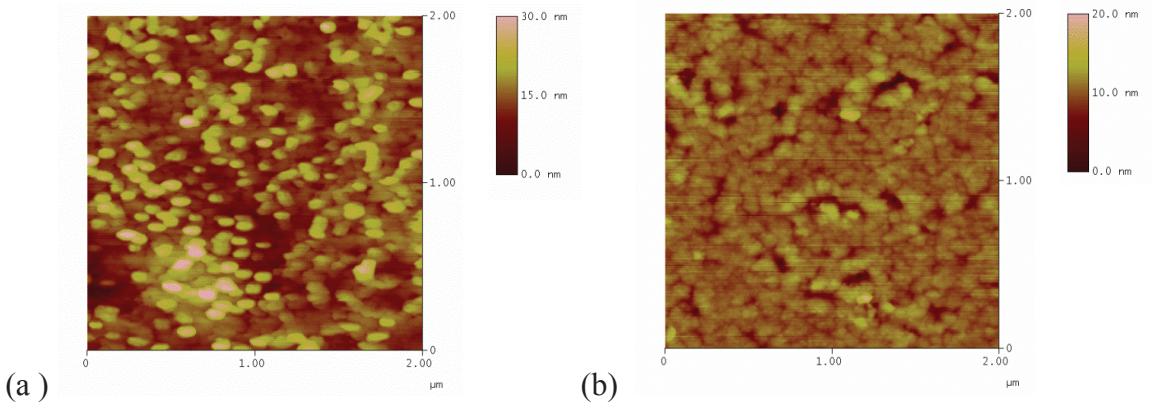

Figure 5-3. AFM images of the layers deposited with a) 2 sccm O_2 b) 4 sccm O_2.

The AFM roughness of the surface of the thin films is 2.0 and 1.5 nm for 2 and 4 sccm of O_2, respectively. Those values are in perfect agreement with the values calculated from reflectivity measurements.

2.3 Optimizing thin films' crystallinity

The optimization of the crystallinity was performed using a $Ga_{0.6}Fe_{1.4}O_3$ target, because this composition is the one for which the magnetic order temperature is the highest. XRD patterns of gallium ferrite films deposited at different Ar/O_2 ratios are shown in Figure 5-4.

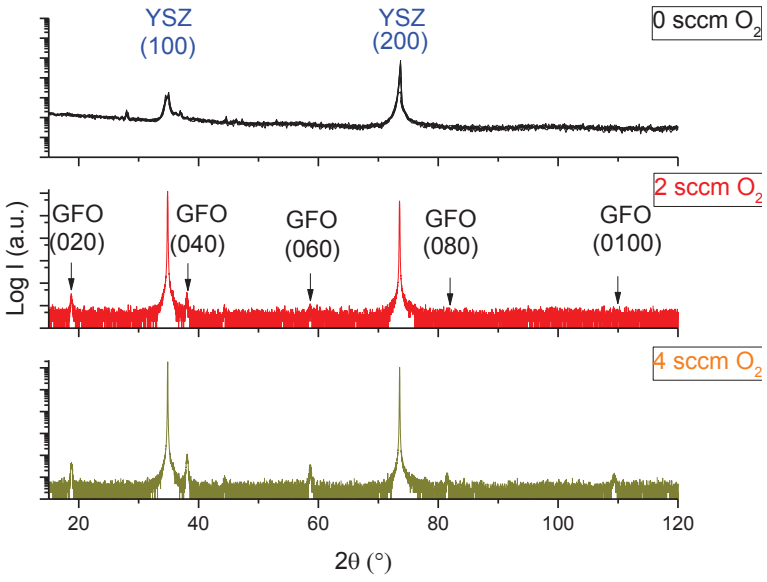

Figure 5-4. X-Ray diffractograms of GFO thin films deposited with different amount of oxygen in the chamber: no oxygen, 2 sccm O_2, and 4 sccm O_2. The flow rate of Ar was 20 sccm in all cases.

The composition of the deposited films was checked by EDX and is in good agreement with to the composition of the target, $Ga_{0.6}Fe_{1.4}O_3$, within 3% error bar.

The film deposited with no oxygen didn't show any crystallization. On the other hand, starting from 2 sccm of O_2 introduced in the chamber, the (0*k*0) diffraction peaks are observed, indicating a formation of oriented GFO. In case of 4 sccm of O_2, the peaks are becoming even stronger. No parasitic phase was detected. Since a GFO layer deposited with 4 sccm of O_2 showed the best results, it was decided to perform further characterizations on this layer. Reflectivity measurements allowed evaluating the thickness to 40 nm. The *Φ*–scans of the $(057)_{Pc21n}$ and $(206)_{Pc21n}$ nodes of the GFO thin films deposited with 4 sccm O_2 presented twelve-fold peaks located every 30° (Figure 5-5).

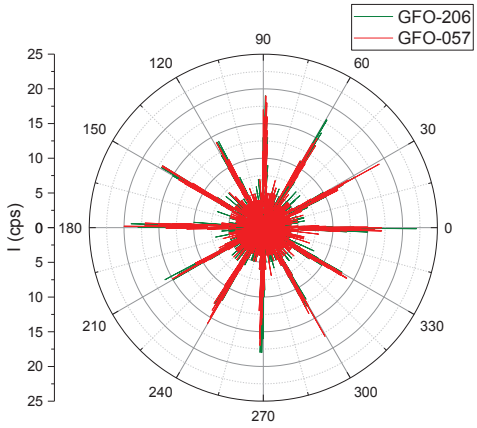

Figure 5-5. *Φ*-scans of the $(206)_{Pc21n}$ and $(057)_{Pc21n}$ nodes of the GFO thin film deposited with 4 sccm O_2.

Those nodes were selected due to their intensity, in order to perform a reciprocal space mapping for estimation of cell parameters of the GFO. The results are present on the Figure 5-6.

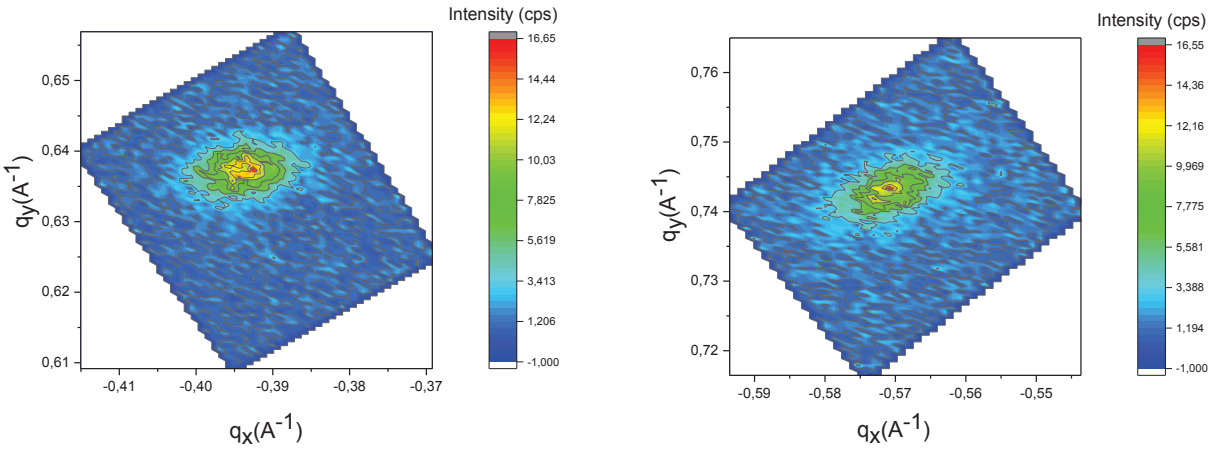

Figure 5-6. Reciprocal space mapping of reflections (062) and (570) of the GFO thin film deposited with 4 sccm O_2.

We deduce from all these measurements the lattice parameters a_{GFO} = 8.749 ± 0.002 Å, b_{GFO} = 9.436 ± 0.003 Å and c_{GFO} =5.072 ± 0.003 Å for the GFO thin film deposited with 4 sccm O_2. These values are in good agreement with the bulk lattice parameters of $Ga_{0.6}Fe_{1.4}O_3$ (Figure 5-7). The maps were performed for each lattice direction. No variation of the lattice parameters was observed.

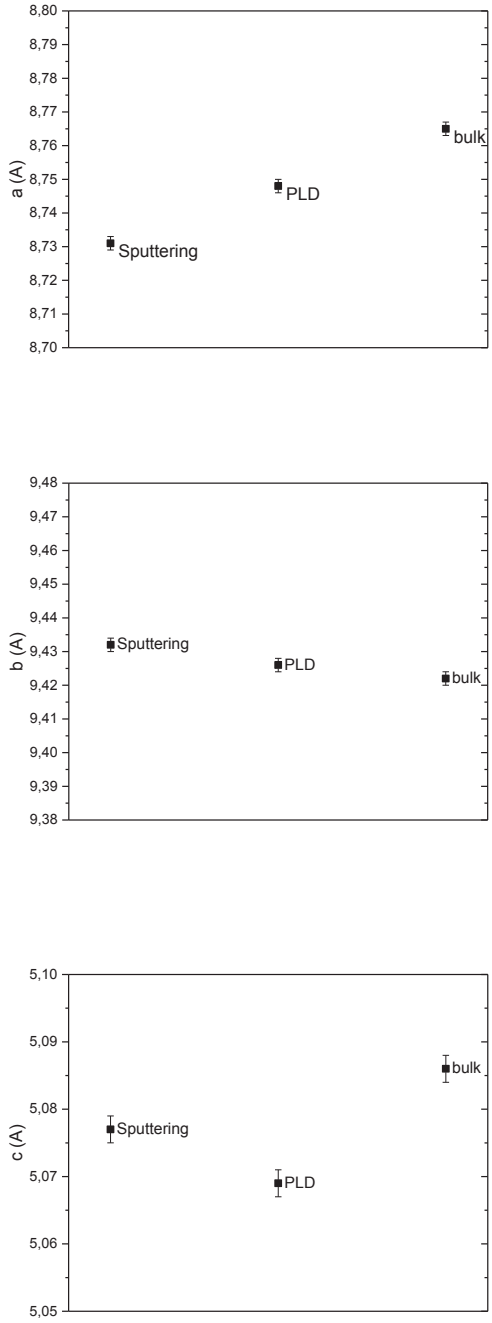

Figure 5-7. Cell parameters of the thin films obtained by sputtering, PLD (for depositions of the same composition on the same YSZ(100) substrate) and the bulk value[7].

As in the case of PLD deposited thin films, the *a* and *c* parameters are smaller than for bulk, when *b* is higher. The small difference in the PLD and sputtered samples could be due to the number of oxygen vacancies, as the main principal growth process is different.

2.4 Magnetic properties of GFO thin films made by sputtering

Figure 5-8 shows ZFC-FC curves obtained for a thin layer of GFO deposited on YSZ (100) with 4 sccm O_2 and 20 scccm Ar. The Néel temperature is determined to be 345 K. This value is in total agreement with the Neel temperature measured for the GFO thin films deposited by PLD.

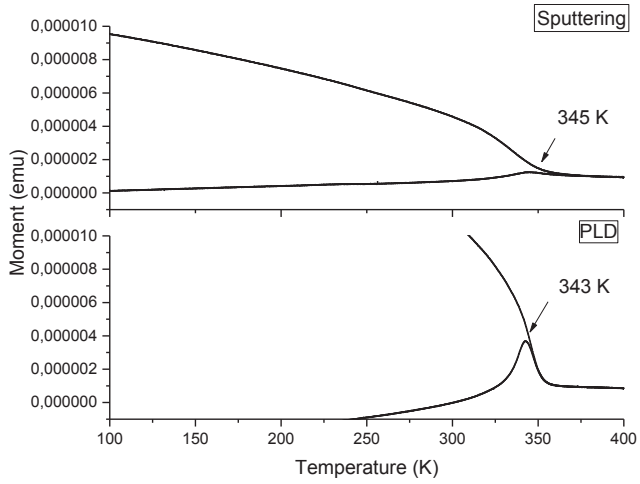

Figure 5-8. ZFC-FC curves measured with an applied field of 50 Oe for GFO thin films deposited by sputtering (40 nm) and PLD (100 nm)

Hysteresis loops of the samples, measured at 300K and 5K are shown in Figure 5-9.A strong anisotropy of the magnetization is observed, similar to the one observed for the layer done by PLD, with an easy magnetization direction within the plane of the sample. The *c*-axis ($Pc2_1n$) of GFO, which corresponds to the direction of easy magnetization, is oriented in the plane of the thin layer. The *b*-axis which is an axis of hard magnetization, is perpendicular to the plane of the layer. The existence of six variants of GFO is responsible for the quasi isotropic magnetic behavior in the plane of the thin layer of GFO on YSZ (100).

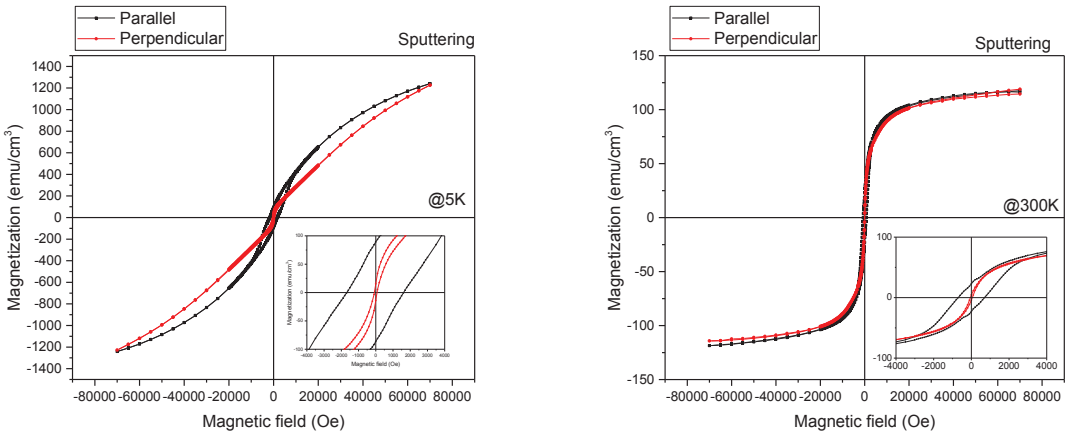

(a)

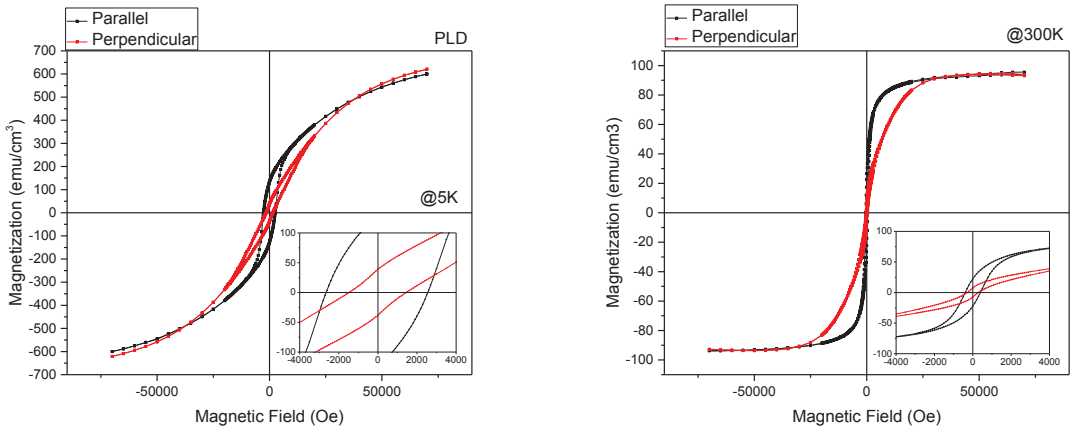

(b)

Figure 5-9 Hysteresis loops measured at 5 and 300 K for GFO made by sputtering (a) and by PLD (b) in both parallel and perpendicular directions to the plane of the sample.

Hysteresis loops measured at 300 K (Figure 5-9) indicate non negligible saturated room temperature magnetization for parallel measurement of about 100 emu/cm^3. This value measured for the sputtered layer is comparable to one obtained by PLD. The magnetization loops measured at 5K do not show saturation.

2.5 Structure study by TEM

The sample which showed the best crystallographic quality (4sccm O_2, 20 sccm Ar) was prepared for TEM observation. Two different sample preparation methods were used: an ion milling method for the sample in cross section (CS) and a plane view (PV) made by scratching the surface with a diamond tip and deposited on a copper grid covered with a membrane.

A TEM high resolution image of the CS sample prepared by ion milling is shown on Figure 5-10. A fast Fourier transform of this image shows the reciprocal lattice of the material. It does not correspond to the reciprocal lattice of the orthorhombic GFO but to that of a spinel phase (face centered cubic) in the zone axis [112]. The growth axis would then be along the [111] and it would have a lattice parameter of 8,2 Å (5.10 a,b).

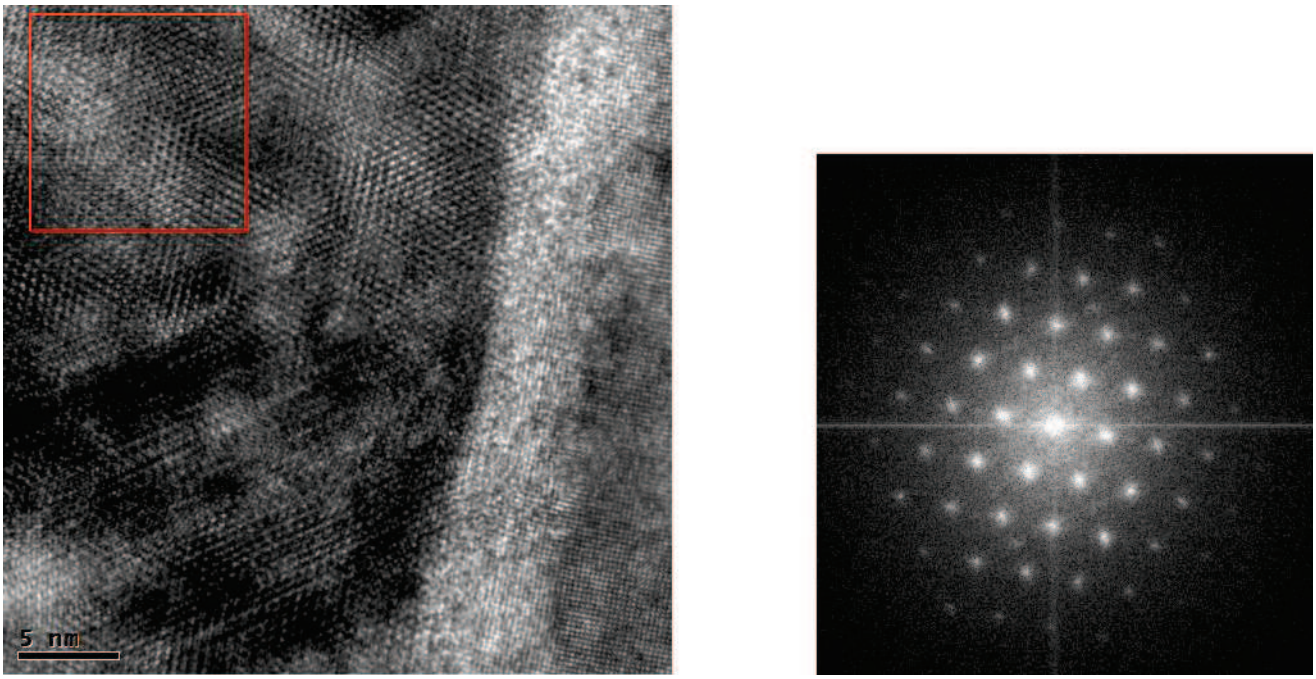

a) b)

Figure 5-10. a) TEM high resolution image of ion milled GFO thin film in CS deposited with 4 sccm O_2 and b) fast Fourier transform of the red square image (a).

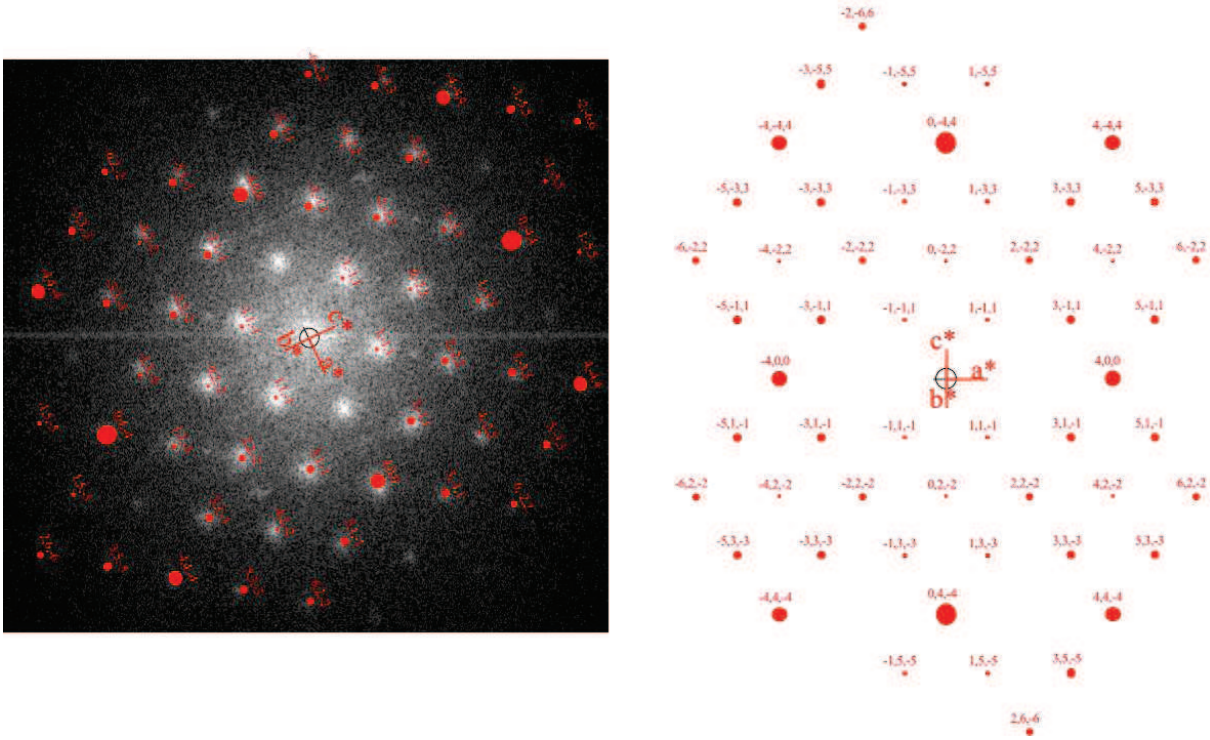

c) correlation of the FFT presented in (b) with the reciprocal lattice of a spinel phase in [112] zone axis.

The cell parameters of the spinel used to match with the structure observed by TEM (Figure 5-10) should lead to observation of peaks at angles of.18.4° (when GFO(020) is 18.8°), 37.4° (when GFO(040) is at 38.07°) and 57.1° (when GFO(060) is at 58.6°) (Figure 5-11).

The X-ray diffractograms of the sample before its preparation for TEM are shown on Figure 5-11 together with the positions of the peaks expected from the phase observed by TEM (Figure 5-10) with a cell parameter of a=8.2 Å and [111] direction perpendicular to the sample surface.

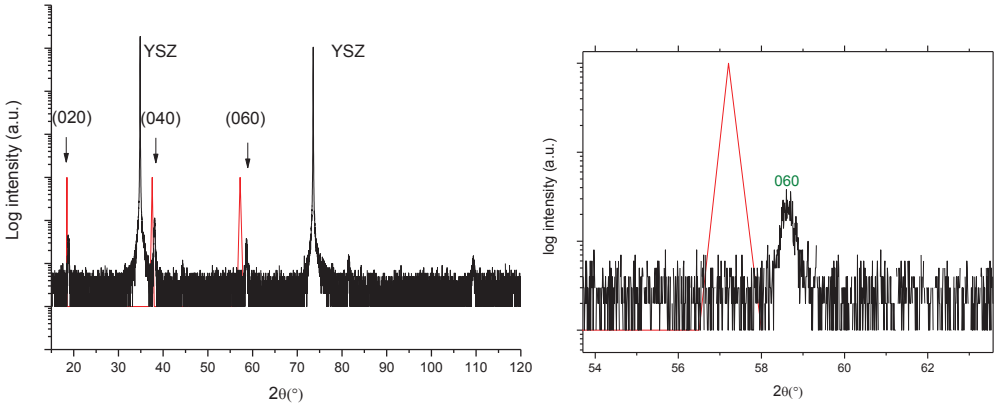

a) b)

Figure 5-11. Sputtered GFO film (4 sccm O_2, 20 sccm Ar) (in black) with the position of the peaks which should have been observed when considering the spinel-like phase observed by TEM (Figure 5-10) (in red) (b) magnification of the (060) peak.

The peaks that should be present due to the phase observed by TEM are far from the experimentally obtained peaks corresponding to the orthorhombic GFO.

The structure observed by TEM in case of the preparation of the sample by ion milling isn't corresponding to the original structure observed with XRD. This is a hint that the structure of the thin film transformed during ion-milling from the orthorhombic to the face centered cubic one.

A plane view was prepared in order to check the presence of this parasitic spinel phase. A plane view allows observing the layer perpendicular to the growth axis. A simple scratch with a diamond tool was performed on the surface of the film. A high resolution image of this plane view is shown on Figure 5-12.

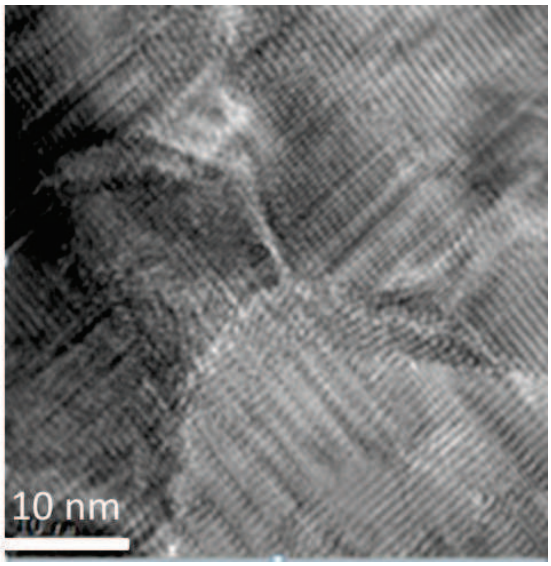

Figure 5-12. High resolution TEM image of the plane view of the GFO thin film deposited with 4 sccm O_2/20 sccm Ar.

The electron diffraction pattern obtained for this sample is the superimposition of two variants oriented 90° from one another (Figure 5-13).

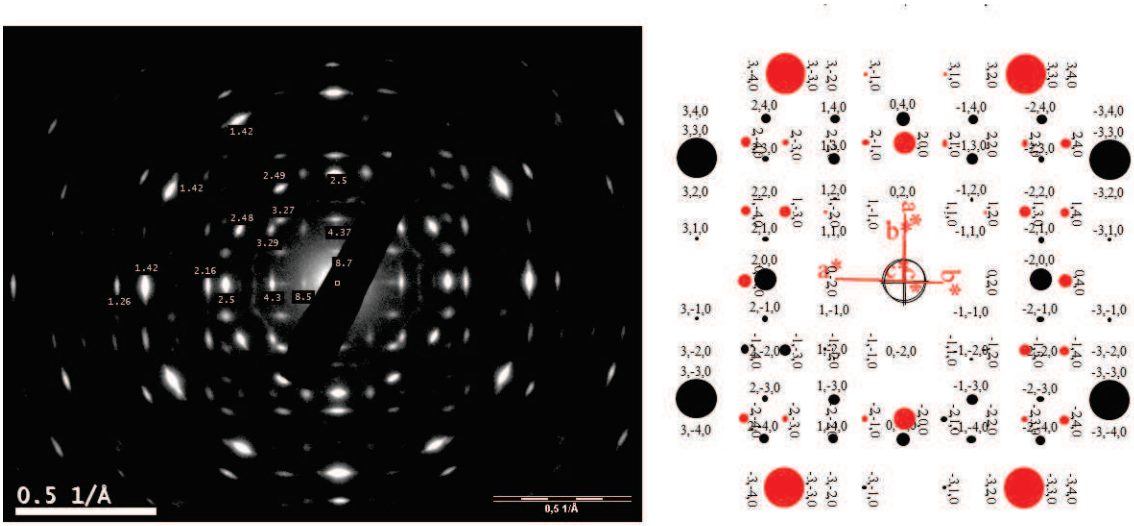

a) b)

Figure 5-13. (a) electron diffraction pattern of the GFO thin film presented in Figure 5-12; (b) corresponding reciprocal lattice of the orthorhombic GFO phase in its [001]Pna2$_1$ (*i.e.* [010] Pc2$_1$n) zone axis with 2 different orientations at 90° from each other reproducing well the electron diffraction pattern observed in a).

The analysis of the Figure 5-13 confirmed the orthorhombic $Pc2_1n$ crystallographic structure of the sample with a growth along the *b* axis.

The preparation method of samples for TEM analysis therefore plays an important role. It may yield to a phase transformation from orthorhombic to cubic spinel in case of the ion-milled sample. Scratching the layer is not an energetic process and it doesn't modify the crystallographic structure of the sample. This phase transformation is an indicator of a relative instability of the orthorhombic GFO structure deposited by sputtering.

3. Deposition on conducting substrates

3.1 Deposition on Pt buffered YSZ(111)

In order to perform electrical measurements on the thin films it was necessary to optimize depositions on a conducting substrate. Ultrathin Pt layers (20 nm) were deposited by PLD and then introduced into the sputtering chamber. The depositions were done with the 4 sccm O_2 and 20 sccm Ar, a temperature gradient starting from 600°C (lower than required for GFO deposition) and then increased with a step 10° per 3 min up to 750°C in order to avoid thermal stress for Pt [8]. On Figure5-14 is shown a diffractogram for depositions on Pt(111)//YSZ(111).

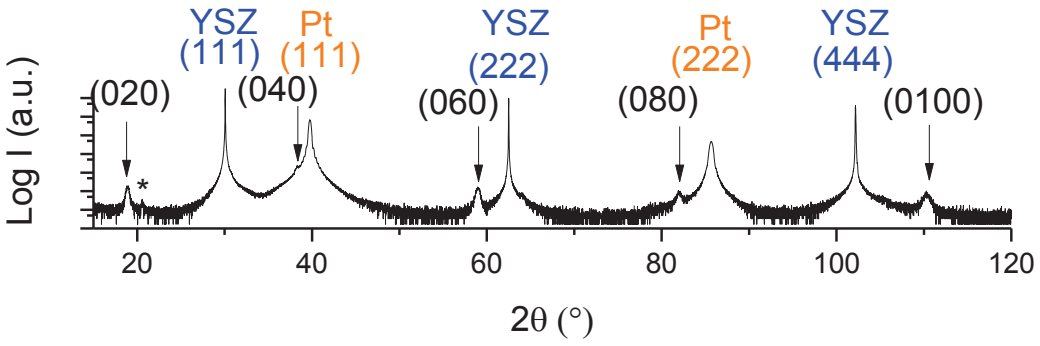

Figure 5-14. X-Ray diffractogram of a GFO thin film deposited on Pt buffered YSZ(111).

The XRD analysis didn't show any parasitic phase into GFO structure. The GFO structure showed a (0*k*0) orientation, with weakly intense peaks. By * is indicated an artifact from the equipment. However it wasn't possible to measure Φ–scans or RSM

maps of the (206) $_{Pc21n}$ and (057)$_{Pc21n}$. This is probably due to a lower quality of the films deposited onto Pt(111). The SEM analysis of the surface showed the formation of holes on the thin film of GFO as well as a problem with Pt itself (Figure 5-15).

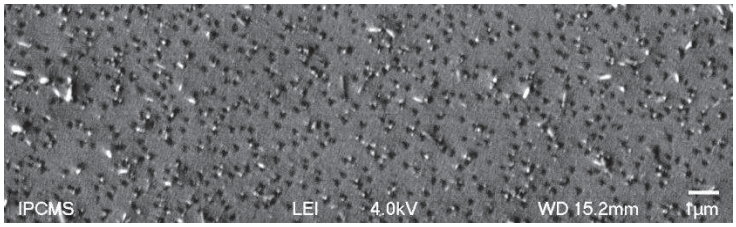

Figure 5-15. SEM image of GFO layer deposited on Pt//YSZ(111).

It was possible to detect a 'sticking' problem of the platinum to the substrate meaning that the GFO growth is prevented by the Pt itself.

3.2 Deposition on STO:Nb(111)

Figure 5-16 present the X-Ray diffractogram obtained for a GFO 1.4 thin film sputtered onto STO:Nb(111).

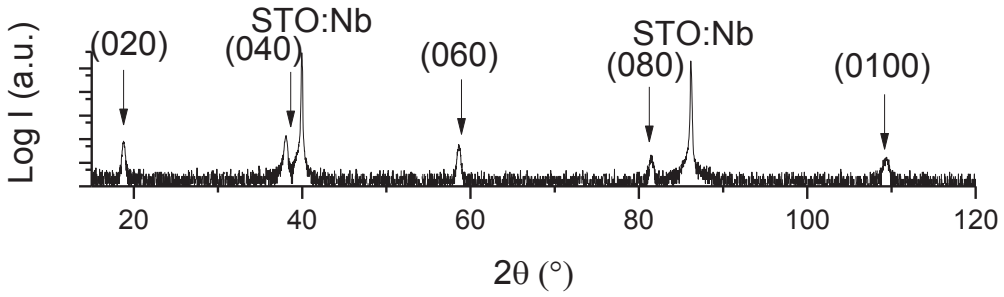

Figure 5-16. X-Ray diffractogram of a GFO thin film deposited on STO:Nb(111).

No parasitic phase is observed. The peaks of GFO are well defined and the out of plane cell parameter is corresponding to the expected value. Roughness, measured with reflectivity is less than 1 nm.

SEM image of the surface shows a smooth surface without surface defects. No holes, splashing or grains were observed (Figure5-17).

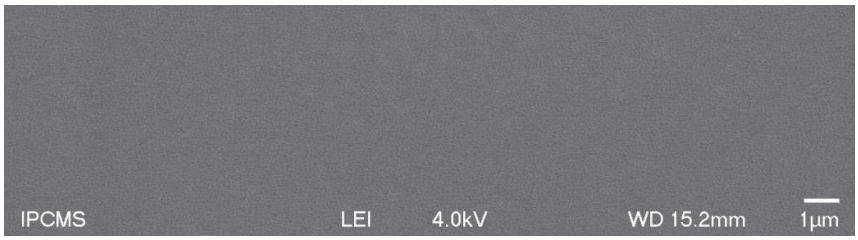

Figure 5-17 SEM image of the GFO layer deposited on STO:Nb(111).

The observed sample was also homogeneous in composition which was evaluated as $Ga_{0.53}Fe_{1.48}O_3$, in relatively good agreement with the target composition.

The Φ-scans of the nodes (057) and (206) show existence of three variants (Figure 5-18).

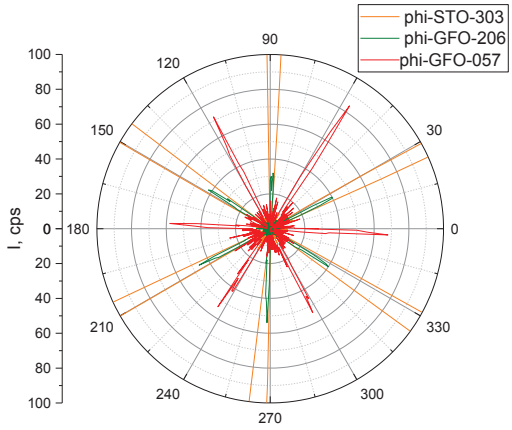

Figure 5-18. Φ-scans of (057) $_{Pna21}$ and (206)$_{Pna21}$ of GFO.

The quality of the layer was high enough to allow obtaining the RSM maps of (057) and (206) reflections (Figure 5-19). The lattice parameters could be calculated and are in good agreement with those obtained for PLD deposited samples (Figure 5-20).

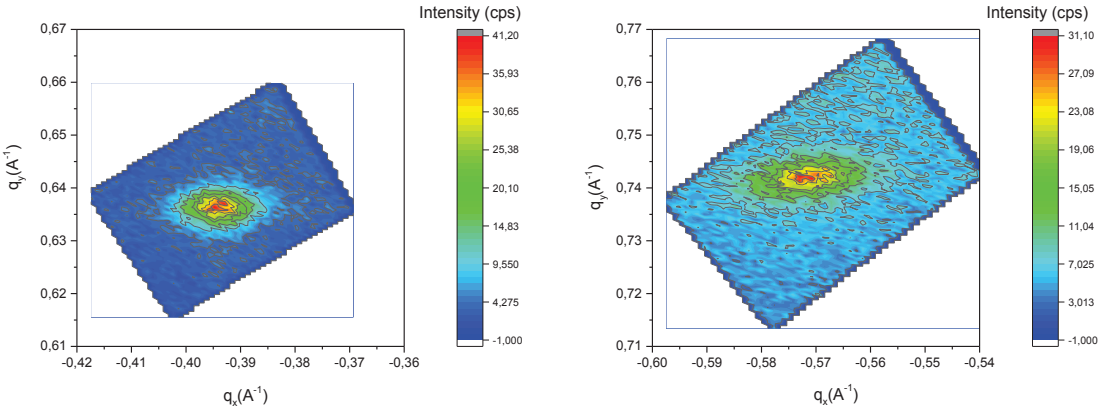

Figure 5-19. Reciprocal space maps of the (057) and (206) reflections of GFO.

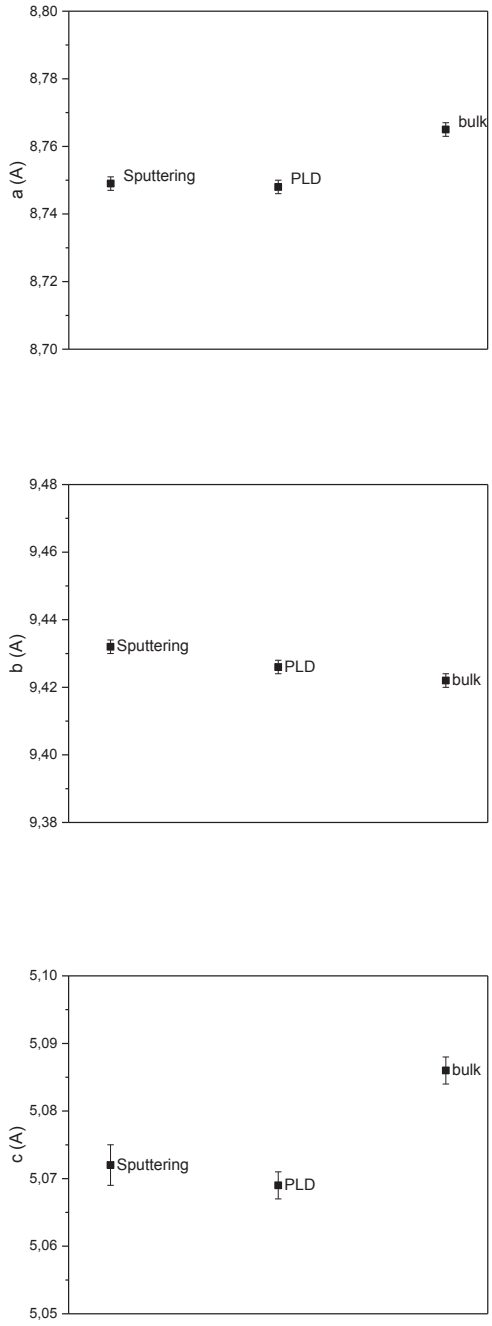

Figure 5-20. Cell parameters of the GFO 1.4 thin film sputtered on STO:Nb (111) with those of the PLD deposited films and bulk materials of the same composition.

As in case of the depositions done on YSZ(100) substrate, the cell parameters of the samples deposited on STO:Nb(111) are lower than the bulk value for the in-plane parameters and higher for the out of plane parameter.

Conclusion

It was possible to optimize the depositions of GFO thin films into both YSZ(100) and STO:Nb(111). The deposition on conducting electrode Pt buffered YSZ(111) still requires some more studies, neither the crystallization of the thin film nor the roughness are suitable for further investigations.

4. Deposition under electric bias

4.1 Deposition on YSZ(100)

Substrate biases between O and 50 V were applied during the deposition process. X-Ray diffractograms (Figure 5-21) indicate that the application of the substrate bias resulted in a significant decrease of the thin film quality.

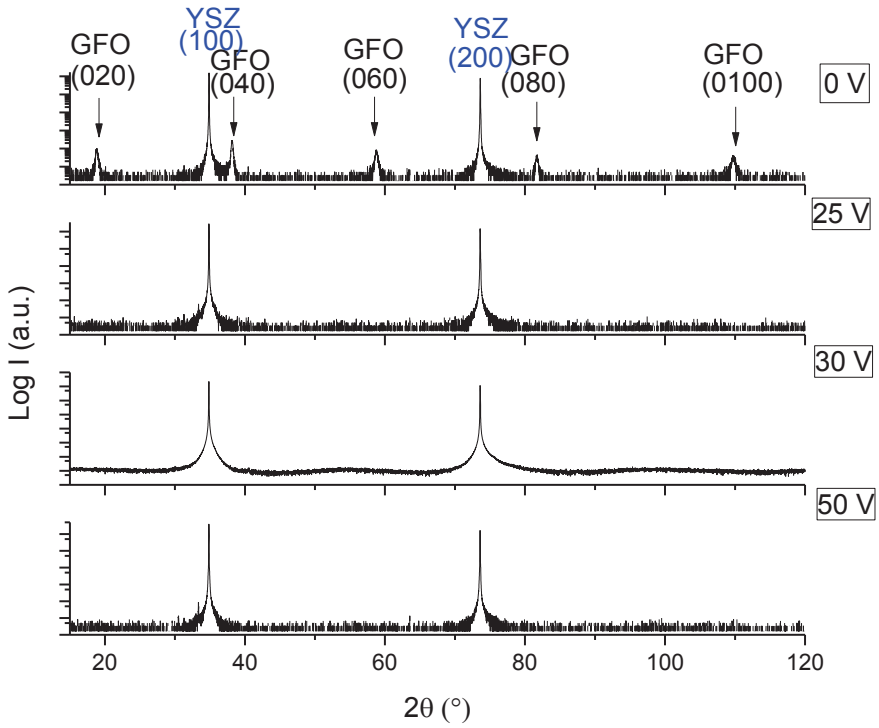

Figure 5-21. XRD of GFO thin films deposited on YSZ(100) with different substrate biases.

Films deposited without any substrate bias exhibit a texture with crystallites orientated along the (0*k*0) direction. The application of a bias higher than +25 V prevents the GFO structure from being crystallized. The ion bombardment induced by the bias voltage can also result in a significant modification of the film morphology[9; 10]. As a result particles continue the movement on the substrate bringing disorientation. Bias voltage of +25 V had little influence on the film morphology, but higher ones led to a decrease of the crystalline quality as well as of the surface topology (Figure 5-22).

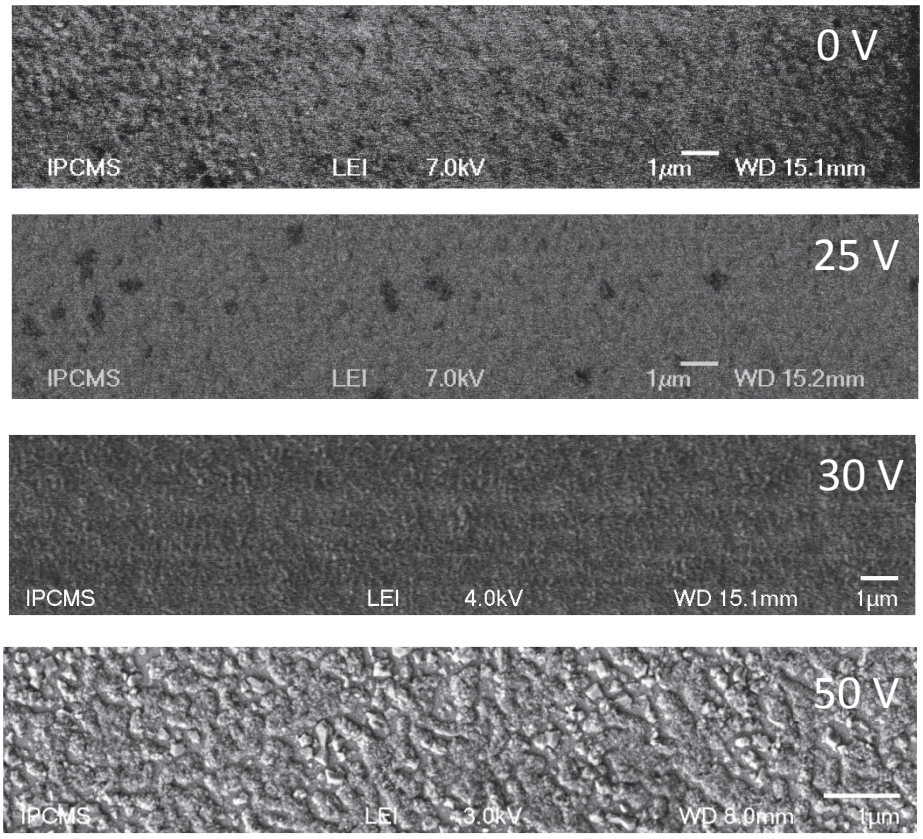

Figure 5-22. SEM observations of GFO thin films deposited on YSZ(100) with different substrate biases.

Figure 5-23 shows a comparison of the roughness measured for films deposited with different substrate biases.

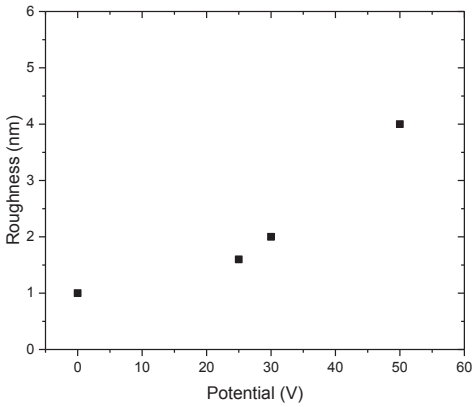

Figure 5-23. Influence of the applied bias on the films roughness.

Results of Figure 5-23 are in agreement with the SEM images (Figure 5-22) showing that with the increase of the voltage the surface quality decreases.

The observed variations in the Ga/Fe ratios as a function of the substrate bias voltage are shown on a Figure 5-24.

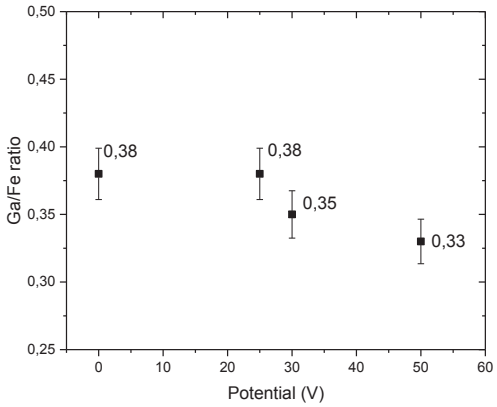

Figure 5-24. Influence of the substrate bias on the composition of the sputtered GFO thin films (Ga/Fe ratio).

For biases lower than +25V, the Ga/Fe ratio remains constant at the value close to the expected one of 0.42. For higher biases, changes and the Ga amount in the thin film decreases. The Ga adatoms would be more easily re-sputtered by incident high-energy ions in the growth process of the films when a bias is applied, which leads to the decrease in Ga content and the increase in Fe content.

In the case of depositions on YSZ(100) substrate, the application of a substrate bias higher than 25 V during the GFO deposition significantly decreases the film crystallization and roughness.

4.2 Deposition on STO:Nb(111)

A study of bias application (V_p=0-20V) was also done on STO:Nb(111) substrates. The X-Ray diffractograms of the sputtered layers are shown in Figure 5-25.

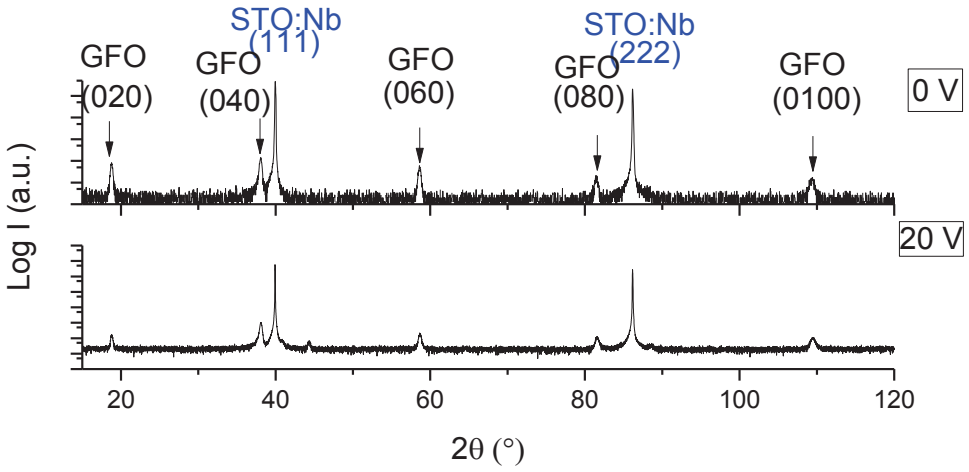

Figure5-25. X-ray diffractograms of GFO thin films deposited on STO:Nb(111) with and without substrate bias

Well crystallized GFO thin films could be obtained under the application of +20 V substrate bias. The films are oriented in (0*k*0) direction but show less intense and wider diffraction peaks than for the layer deposited without any bias. No parasitic phase was observed and the quality of the layer gave the possibility to get reciprocal space maps maps

and calculate the cell parameters in order to compare them with those obtained without bias (Figure 5-26).

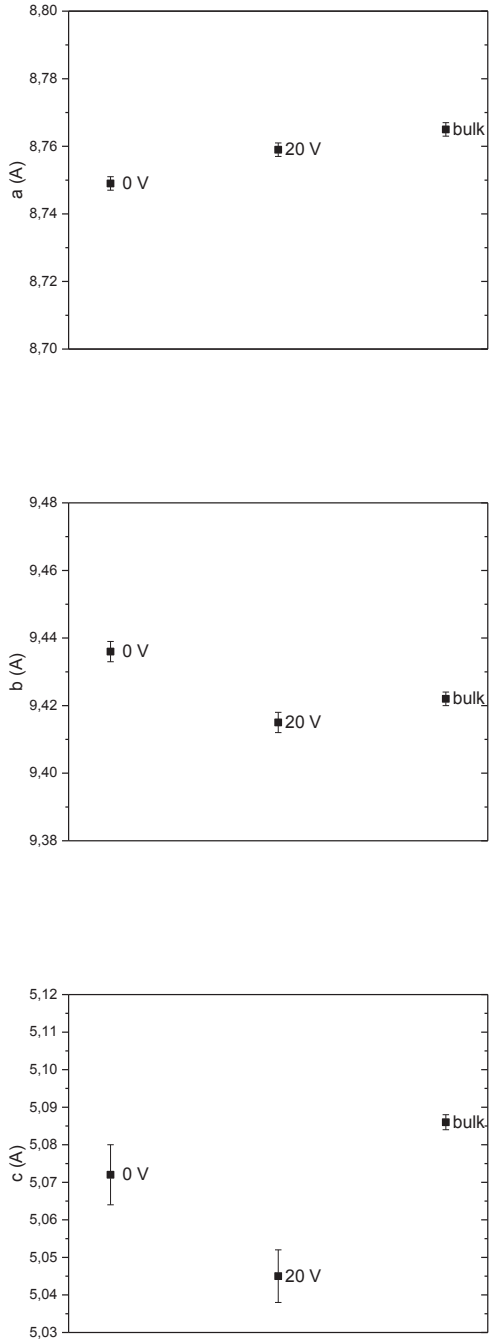

Figure 5-26. Cell parameters of thin films deposited with and without bias on STO:Nb(111), together with the bulk values.

While the in plane parameters are still lower than the bulk values, the out of plane one is also lower, differently to what has been observed until now. This could be due to the constant ion bombardment applied to the layer during its deposition.

The average roughness of a 35 nm thick film deposited on STO:Nb (111) with bias was measured to be less than around 1 nm, that is as low as that of a layer deposited with no bias for a similar thickness. The results are correlating with the SEM observations shown on a Figure 5-27.

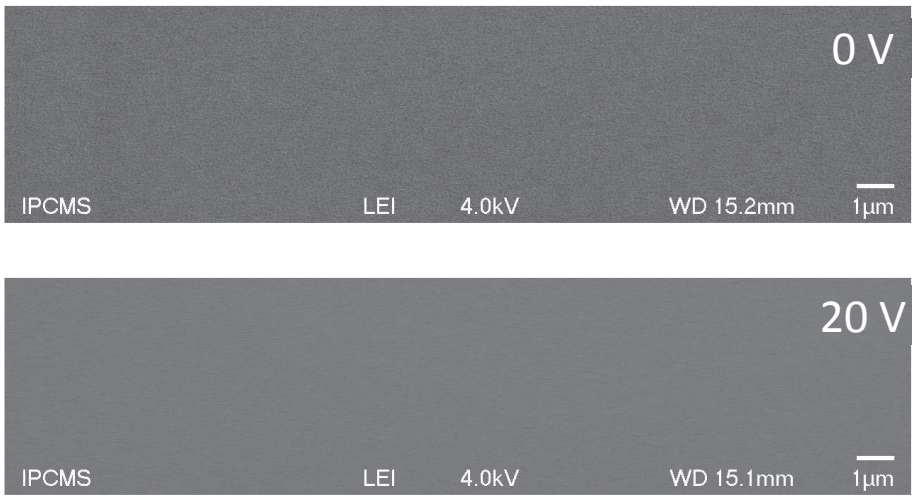

Figure 5-27. SEM images of layers deposited on STO:Nb(111) with and without bias.

The surface investigations of the samples deposited on STO:Nb(111) substrates didn't show any defects like holes or particles.
Figure 5-28 (a,b) shows the hysteresis loops of the layers measured at 5 and 300 K for films deposited with and without application of substrate bias.

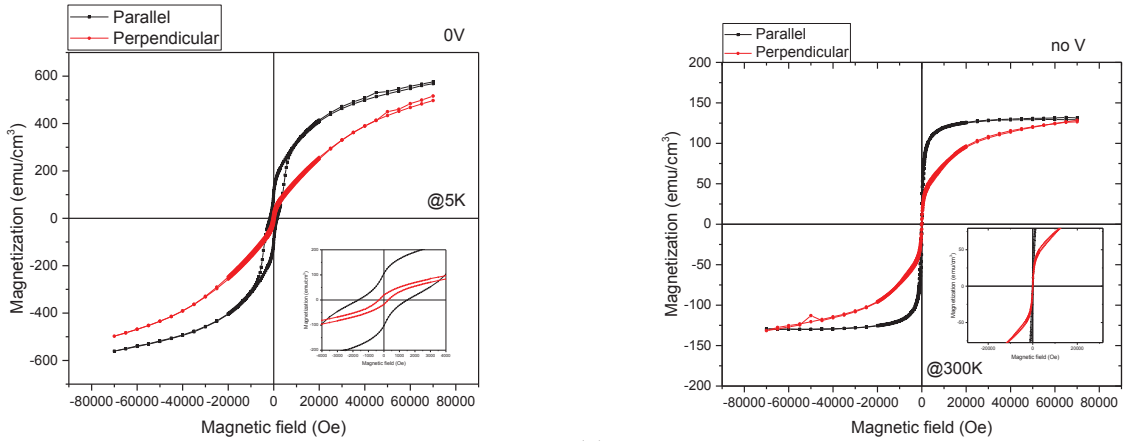

(a)

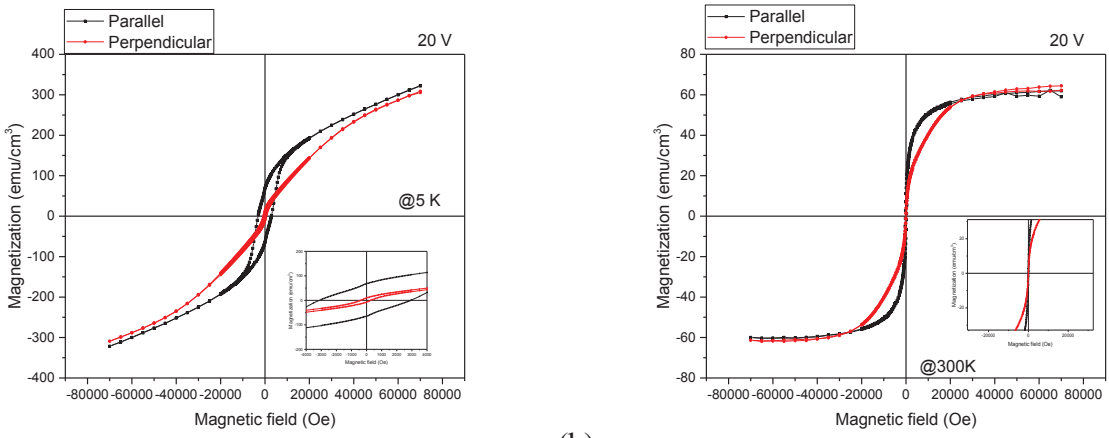

(b)

Figure 5-28. Hysteresis loops measured at 5 and 300 K for GFO films deposited on STO:Nb(111): a) without b) with a +20 V substrate bias.

The +20 V substrate bias has decreased magnetization by a factor of 2. This is possibly due to the fact that the bias has brought the grain boundary phase in different orientations than (0*k*0) not visible with X-ray diffraction. The perturbed growth may lead to distorted zones which are not magnetically ordered.

5. Conclusion

The GFO deposition by sputtering was successfully optimized on different substrates: YSZ(100), STO:Nb(111) and Pt buffered YSZ(111). The best atmosphere conditions were 4 sccm O_2 and 20 sccm Ar. The cell parameters were in good agreement with those obtained for thin films deposited by PLD. The TEM analysis of the sample showed a dependence on the preparation method of the sample for microscopy. In case of ion milling the transformation from *P*c2_1n to *F*d-3m was observed. Magnetic properties of the thin films showed the same behavior as in the case of thin films done by PLD. The estimated Neel temperature is of 345 K.

Investigations of the bias influence on the properties of the thin film demonstrate that when the ion bombardment energy is excessive, the impact of high-energy ions on the substrate surface causes damage and disturbs the crystal growth. During deposition, an ion bombardment energy suppresses the growth of an ordered crystalline film. It was possible to obtain well crystallized GFO films under the application of a bias up to 20V. It leads to a modification of the cell parameters and magnetic properties of the films.

Bibliography

[1] Soylu, M., Cavas, M., Al-Ghamdi, A. A., Gafer, Z., El-Tantawy, F. and Yakuphanoglu, F., Solar Energy Materials and Solar Cells 124 (2014) 180.

[2] Trassin, M., Viart, N., Versini, G., Barre, S., Pourroy, G., Lee, J., Jo, W., Dumesnil, K., Dufour, C. and Robert, S., Journal of Materials Chemistry 19 (2009) 8876.

[3] Sreedhar, A., Hari Prasad Reddy, M., Uthanna, S. and Pierson, J. F., ISRN Condensed Matter Physics 2013 (2013) 9.

[4] Iftimie, S., Mallet, R., Merigeon, J., IONb, L., Girtan, M. and Antohe, S., DIGEST JOURNAL OF NANOMATERIALS AND BIOSTRUCTURES 10 (2015) 221.

[5] Richardt, A. and Durand, A.-M. (1997). Les Interaction Ion Énergétiques-Solides, fine.

[6] Krylov P., Zakirova R., Fedotova I. and Gilmutdinov F., Physics and Techniques of semiconductors 47 (2013) 870.

[7] Lefevre, C., Roulland, F., Thomasson, A., Meny, C., Porcher, F., Andre, G. and Viart, N., Journal of Physical Chemistry C 117 (2013) 14832.

[8] Trassin, M., Viart, N., Ulhaq-Bouillet, C., Versini, G., Barre, S., Leuvrey, C. and Pourroy, G., Journal of Applied Physics 105 (2009) 6101.

[9] Kelly, P. and Arnell, R., Vacuum 56 (2000) 159.

[10] Kovac, J., Stock, H.-R. and Zoch, H.-W., Journal of Surface Engineered Materials and Advanced Technology 2 (2012) 115.

General conclusion

The work presented in this manuscript addresses challenges concerning the electric behavior of $Ga_{2-x}Fe_xO_3$ (GFO) thin films. The deposition of GFO thin films had been optimized by pulsed laser deposition in previous works done in our research team. The control of their leakage currents and enhancement of their polarization however still needed optimization. It had been shown that the introduction of a bivalent cation such as Mg^{2+} could reduce the leakage currents of the films but it was accompanied with a reduction of the magnetic properties of the films and the conduction phenomena were not fully understood.

The objectives of the work presented in this manuscript were two-fold: understand and fully control the electric conduction phenomena which take place in GFO thin films, on the one hand, and find pathways towards the optimization of the polarization of these films, on the other hand.

The first fold of the work was carried out studying the effect of the insertion of Ni cations into GFO films. Ni cations were selected because they are bivalent cations, as Mg^{2+}, but also present a magnetic moment. We have observed the evolution of structural, electric and magnetic properties of thin films of $Ga_{0.6}Fe_{1.4}O_3$, upon Ni^{2+} doping up to 5 %. Three different substrates were used in order to compare the properties of the thin films: the two conducting Pt(111)//YSZ(111) and STO:Nb(111), and the non-conducting YSZ(100). In case of depositions done on Pt(111)//YSZ(111) it was not possible to obtain parasitic free GFO phase. In case of STO:Nb(111) and YSZ(100) substrates, it was possible to insert up to 5% of Ni into the GFO structure. Resonant X-ray diffraction was used to assert the actual insertion of the Ni cations within the GFO cell. The insertion of 2 % Ni shifts the cell parameters of GFO thin films towards values close to those observed for bulk, while they are different for Ni contents below and above this value. Structural analysis performed by TEM evidenced a spinel-like phase within the GFO films, for depositions on both STO:Nb(111) and YSZ(100) substrates. Its growth is perfectly oriented along its [111] direction. The cell parameter of this spinel-like phase is such that most of its interplanar distances are fully compatible with those of the GFO phase. This may explain why this extra phase was never detected in θ–2θ X-ray diffraction patterns. The Néel temperature of the films reaches a maximum for the 2 % Ni content, probably because its structure is the closest to the bulk one, allowing optimized orbital overlapping and superexchange interactions. The semiconducting behaviour of the films was evidenced by Van der Pauw measurements. The resistivity showed a maximum for the 2 % Ni-doped sample. The number of carriers and their mobilities were evaluated from Hall Effect measurements. A conductivity type inversion, from *n* to *p*, is evidenced when going from low to high Ni doping contents. These observations allowed fully understanding

the conduction phenomena in the GFO films, as due to a hopping conduction mechanism between Fe^{2+} and Fe^{3+}. The possibility to tune the conduction type in a semiconducting ferrimagnetic oxide is certainly a major achievement of this thesis.

The second fold of this study was explored optimizing the deposition of GFO films with a technique which allows the application of an electric field during the deposition: sputtering. It was shown that to solve the stoichiometry transfer problem, a pre-sputtering time of 60 min needed in order to achieve equilibrium in the plasma and have a film of the composition of the target. The study of optimization of crystallinity was performed on 3 different substrates: YSZ(100), Pt(111)//YSZ(111) and STO:Nb(111). Best results in terms of crystallographic quality of the thin films were obtained for a deposition atmosphere consisting in 4 sccm O_2 and 20 sccm of Ar, at the temperature of 700 °C, and with a radiofrequency power of 40W. It was possible to optimize the depositions of GFO thin films onto both YSZ(100) and STO:Nb(111). The deposition on the conducting electrode Pt buffered YSZ(111) still requires some more studies. It was shown that the ion milling used for the TEM samples preparation had an influence on the crystallographic phase of the sputtered films. When the samples were thinned by ion milling, a phase transformation from $Pc2_1n$ to Fd-3m space groups takes place. When the samples are prepared without any ion milling, as in the case of a scratched sample, only the $Pc2_1n$ phase is observed. This possible phase transformation under ion milling indicates some instability of the crystallographic structure of the sputtered GFO films. The room temperature saturation magnetization was of about 100 emu/cm^3 for GFO 1.4 which is comparable to results obtained for GFO thin films elaborated by PLD. Finally, we studied the influence of a voltage bias applied to the substrate during deposition of the films by sputtering on their structure and properties, as a first step towards possibilities of polarization enhancement. It was shown, that high biases are disturbing the growth of the GFO thin films and prevent their crystallization. In case of the lowest applied bias of 20 V it was possible to get a crystallized GFO layer. But when comparing the magnetization of the layers that were deposited with and without bias, it appeared that the application of a bias decreased it by a factor of 2.

The main perspectives of this work still concern the electric behavior of the GFO films, both their conduction properties and polarization.

We plan to study further possibilities of reducing the leakage currents, without doping, on the one hand, *via* annealing the films in an oxidizing atmosphere, or through doping with cations whose sizes are larger than transition metal cations, such as rare-earth elements, on the

other hand. The objective of this possibility is to distort the GFO cell and induce an increased polarization.

Then, it is to be noted that despite the efforts of our collaborators, no polarization loop could be observed on the films elaborated for this work. In that respect, the issue of the electrodes, both bottom and top, is crucial and will need to be optimized. The introduction of Ni into the GFO structure allowed perfect control of the electric behavior of the films, but was not possible on the conducting Pt buffered YSZ(111). Other substrates were not conducting enough to allow perpendicular characterizations.

Finally, we also plan to continue further investigating the influence of the application of a voltage bias during the elaboration of the sputtered GFO films on their properties. The next investigations concern TEM analysis and electrical characterizations of the samples deposited with and without bias. It would also be interesting to check the influence of negative electric fields on the formation of GFO during the deposition.

.

Anna Demchenko

Exploration des possibilités offertes en termes de multiferroïcité par le ferrite de gallium en couches minces

Résumé

Les matériaux multiferroïques et/ou magnétoélectriques sont riches en promesses de nouvelles applications, comme par exemple des mémoires quatre états à densité accrue ou des mémoires magnétoélectriques à faible consommation d'énergie. Ces promesses restent cependant pour l'instant lettres mortes en raison du très faible nombre de matériaux présentant ces propriétés à température ambiante, et des forts courants de fuite qu'ils présentent en couches minces. Cette thèse porte sur un matériau prometteur en termes d'applications, car magnétoélectrique et ferrimagnétique à température ambiante, le ferrite de gallium de composition $Ga_{0.6}Fe_{1.4}O_3$ (GFO).

Nous avons démontré la possibilité de réduire les courants de fuite et moduler à volonté le type de conduction *n* ou *p* dans les couches minces de cet oxyde transparent, semi-conducteur, et magnétique, par dopage par des ions Ni^{2+}. Une optimisation de la croissance de GFO par pulvérisation cathodique a par ailleurs montré qu'il était possible de le déposer sous champ électrique, ce qui ouvre d'intéressantes perspectives pour l'optimisation de la polarisation électrique des couches minces.

Mots clés: Oxydes fonctionnels en couche mince, magnétoélectrique, multiferroïque, courants de fuite, mécanismes de conduction électrique, ablation laser, pulvérisation cathodique

Résumé en anglais

The multiferroic and/or magnetoelectric materials are full of promises in terms of new applications, such as for example higher density four state memories or lower power consuming magnetoelectric memories. These promises are however actually put off because too few materials present these properties at room temperature and because their thin films present too high leakage currents. This thesis focusses on a room temperature magnetoelectric and ferrimagnetic material promising in terms of applications, the gallium ferrite $Ga_{0.6}Fe_{1.4}O_3$ (GFO).

We have demonstrated the possibility to strongly reduce the leakage currents and perfectly tune from *n* to *p* the conduction type in transparent, semi-conducting, and magnetic thin films of GFO through Ni^{2+} doping. The optimization of the growth of GFO thin films by sputtering has moreover shown the possibility of deposition under an electric field, which opens ways to control of the electric polarization of the films.

Key words: Functional oxides thin films, magnetoelectric, multiferroic, leakage currents, pulsed laser deposition, sputtering